

Seyed Hamidreza Afzalimir

**Evaluation of CTOD resistance curves in clamped SE(T)  
specimens with weld centerline cracks**

Versão Corrigida

Tese apresentada à Escola Politécnica da  
Universidade de São Paulo para a obtenção do  
Título de Doutor em Ciência.

São Paulo 2022

Seyed Hamidreza Afzalimir

**Evaluation of CTOD resistance curves in clamped SE(T)  
specimens with weld centerline cracks**

Versão Corrigida

Tese apresentada à Escola Politécnica da  
Universidade de São Paulo para a obtenção do  
Título de Doutor em Ciência.

Área de Concentração:  
Engenharia Naval e Oceânica


Orientador:  
Professor Titular Claudio Ruggieri


São Paulo 2022

Autorizo a reprodução e divulgação total ou parcial deste trabalho, por qualquer meio convencional ou eletrônico, para fins de estudo e pesquisa, desde que citada a fonte.

Este exemplar foi revisado e corrigido em relação à versão original, sob responsabilidade única do autor e com a anuência de seu orientador.

São Paulo, 26 de Julho de 2022

Assinatura do autor: 

Assinatura do orientador: 

#### Catálogo-na-publicação

Afzalimir, Seyed Hamidreza

Avaliação de curvas de resistência CTOD em corpos de prova SE(T) fixados por garras e com trincas na linha central da solda / S. H. Afzalimir -- versão corr. -- São Paulo, 2022.

122 p.

Tese (Doutorado) - Escola Politécnica da Universidade de São Paulo. Departamento de Engenharia Naval e Oceânica.

1.Fraturas mecânicas 2.Ductilidade 3.Curvas de resistência CTOD R 4.Dutos 5.Tubulações I.Universidade de São Paulo. Escola Politécnica. Departamento de Engenharia Naval e Oceânica II.t.

## **ACKNOWLEDGEMENTS**

I would like to express my sincere gratitude to my advisor Prof. Claudio Ruggieri for the continuous support of my Ph.D. study and related research, for his patience, motivation, and immense knowledge. His guidance helped me in all the time of research and writing of this report.

## Resumo

Este trabalho aborda a caracterização do deslocamento da abertura da ponta da trinca (CTOD ou  $\delta$ ) sob regime de crescimento estável de trinca (trincas não estacionárias) em corpos de prova SE(T) carregados por garras. Essa caracterização é conduzida por meio de ensaios de tenacidade à fratura e análises numéricas de crescimento estável de trincas em geometrias de corpos de prova extraídas de juntas soldadas circunferências de dutos contendo diferentes propriedades mecânicas. O estudo abrange ensaios experimentais de curvas de resistência à fratura e análises numéricas de crescimento de trincas em condições de deformação plana e modelos 3-D em corpos de prova SE(T) fixados por garra que contêm uma trinca na linha central de solda. A descrição da evolução das forças motrizes (integral-J e do parâmetro CTOD) com o aumento do carregamento monotônico em modo I em materiais dúcteis se dá a partir da modelagem do crescimento de trincas utilizando células computacionais. Ensaios experimentais em soldas circunferenciais de diferentes materiais fornecem as curvas de resistência ao crescimento de trincas, a partir das quais os principais parâmetros microestruturais utilizados na análise de crescimento são calibrados. A presente investigação mostra que as curvas de resistência CTOD baseadas no uso do procedimento de duplo clip-gage (DCG) são consistentemente mais altas do que os correspondentes dados de resistência à fratura baseados nas relações J-CTOD, potencialmente produzindo estimativas não conservadoras de tenacidade à fratura. Para obter uma compreensão mais profunda da correlação das curvas R medidas em corpos de prova SE(T) com o comportamento em dutos reais contendo trincas circunferenciais, curvas R baseadas em DCG também são derivadas a partir da modelagem de dutos. O uso do procedimento de homogeneização, para considerar com precisão o efeito da solda circunferencial com chanfro em V e do revestimento cladeado do duto, confirmou as evidências iniciais sobre a avaliação não conservadora da técnica de DCG. Ao contrário do DCG que requer a medição do CMOD em dois pontos distintos, nas etapas seguintes foram realizadas medições do CTOD usando apenas um valor de CMOD para superar a dificuldade da configuração do DCG (devido ao processo relativamente mais complicado em montar dois extensômetros do tipo clip-gage no corpo de prova). Para isso, é conduzida uma investigação do fator rotacional plástico ( $r_p$ ) para verificar a sua precisão na medição do CTOD. Os resultados mostram que ele fornece curvas R mais conservadoras do que as curvas provenientes dos valores de CTOD baseados na correlação com J, e menos conservadoras em relação às curvas oriundas do método DCG.

**Palavras-chave:** CTOD, J-Integral, Fratura dúctil, Crescimento de trincas, Curvas de resistência CTOD-R, Corpos de prova SE(T), Defeitos circunferenciais, Dutos e tubulações

## Abstract

This work addresses the characterization of the crack tip opening displacement (CTOD or  $\delta$ ) for extending cracks in clamped single edge notched tension, SE(T), fracture specimens based upon fracture toughness tests and numerical analyses of stable crack growth conducted on specimen geometries extracted from pipe girth welds with different material properties. The study covers fracture resistance tests and crack growth analysis of plane strain and 3-D models for clamped SE(T) specimens with a weld centerline crack, in which a computational cell methodology to model Mode I crack extension in ductile materials is utilized to describe the evolution of J and CTOD with increased loading for the extending crack. Laboratory testing of girth welds made of different materials provides the measured crack growth resistance curves from which the key microstructural parameters utilized in the growth analysis are calibrated. The present investigation shows that CTOD resistance curves based on the double clip-gage (DCG) procedure are consistently higher than the corresponding fracture resistance data based on J-CTOD relationships, thereby potentially yielding nonconservative fracture toughness estimates. To gain a deeper insight in correlation of SE(T) fracture specimen R-curves with actual circumferentially cracked pipe, DCG based R-curves are also derived in actual pipe. Using homogenization procedure to accurately consider the effect of V-groove girth weld and clad layer confirmed our initial conclusion regarding DCG nonconservative assessment. Next step, we tried to measure the CTOD using only one CMOD values, unlike DCG that requires CMOD at two point, to overcome the DCG setup difficulty (it is a little bit cumbersome process to mount two clip gauge on one fracture specimen). Plastic rotational factor ( $r_p$ ) is investigated to see if it can measure CTOD precisely or not. The results show that it provides R-curves more conservative than J based CTOD values and less conservative than that of DCG method.

**Keywords:** CTOD, J-Integral, Ductile fracture, Crack growth, CTOD-R resistance curves, SE(T) specimens, Circumferential defects, Pipes

# Contents

Resumo .....	I
Abstract .....	III
Contents.....	IV
List of Figures.....	VI
List of Tables .....	X
List of ABBREVIATIONS.....	XI
List of Symbols.....	XII
1 INTRODUCTION .....	1
1-1 Introduction .....	2
1-2 Study Objectives.....	5
1-3 Thesis structure.....	5
2 LITERATURE REVIEW.....	6
2-1 Introduction .....	7
2-2 The Global Approach to Fracture .....	7
2-2-1 Linear Elastic Fracture Mechanics (LEFM) .....	7
2-2-2 Elastic-Plastic Fracture Mechanics (EPFM).....	11
2-2-3 Failure Assessment Diagram (FAD) .....	22
2-3 The Local Approach to Fracture.....	24
2-3-1 Gurson-Tvergaard-Needleman model for dilatant plasticity .....	25
2-3-2 Assessment of Cracked Components Using Gurson and Rousselier Models. .....	32
2-3-3 Computational cell methodology .....	33
3 EXPERIMENTAL STUDIES .....	38
3-1 Introduction .....	39
3-2 X80 Pipe Girth Weld .....	39
3-3 Dissimilar Nickel-Chromium Girth Weld.....	43
3-4 A106 Pipe Girth Weld .....	44



4	FINITE ELEMENT ANALYSIS .....	48
4-1	Introduction .....	49
4-2	Stationary Crack Analysis .....	49
4-2-1	Plane-Strain Finite Element Models.....	49
4-2-2	3-D Finite Element Models.....	50
4-3	Growing Crack Analysis .....	51
4-3-1	Plane-Strain Finite Element Models.....	51
4-3-2	3-D Finite Element Models.....	52
4-4	Material Models.....	57
4-5	Software .....	57
5	RESULTS.....	58
5-1	Introduction .....	59
5-2	$\eta$ -factors and J-CTOD relationships for stationary crack analysis of V-groove welds .....	59
5-3	CTOD resistance data for extending cracks.....	62
5-3-1	Numerical simulation of crack growth.....	62
5-3-2	CTOD-R curves based on plane-strain analyses.....	63
5-3-3	CTOD-R Curves of the Dissimilar Ni-Cr Girth Weld Based on 3-D Analyses .....	70
5-4	Comparison of R-curve in SE(T) specimen and actual pipe.....	75
5-4-1	X80 pipeline steel.....	75
5-4-2	Dissimilar Ni-Cr Girth Weld .....	77
5-5	R-curves using plastic rotational factor .....	84
5-5-1	A285 steel R-curve using rp method.....	87
6	SUMMARY AND CONCLUSION .....	92
6-1	Summary and Conclusion .....	93
6-2	Future works.....	95
7	REFERENCES .....	96

## List of Figures

Figure2.1 : Stress tensor close to the crack tip.....	8
Figure2.2 : Three modes of crack loading .....	9
Figure2.3 : Effect of specimen thickness on fracture toughness value [45].....	10
Figure2.4 Counterclockwise path around the crack tip for calculating J integral.....	12
Figure2.5 : Two definition for CTOD: a) the displacement at the original crack tip, b) the intersection of a 90° vertex with crack flanks .....	13
Figure2.6 : Higher resistance to crack growth with crack advance .....	15
Figure2.7 : The effect of constraint on R-curve.....	15
Figure2.8 : Partial unloading during the evolution of load with displacement.....	17
Figure2.9 : Numerical scheme based on a standard linear regression performed over discrete points in the load step range defined between $j_0$ and $k$ to determine the $\eta$ -factor. ....	18
Figure2.10 : J integral contour around the crack tip .....	19
Figure2.11 : Double clip-gage method to estimate the CTOD using measurements of crack opening displacements (COD) at two different points.....	21
Figure2.12 : Failure Assessment Diagram (FAD) .....	23
Figure2.13 : Yield surface dependence on the hydrostatic tension and porosity .....	27
Figure2.14 : (a) Evolution of void volume versus crack mouth opening displacement (b) relation between $f$ and $f^*$ .....	30
Figure2.15 : Traction-separation scheme for release of nodal forces for newly deleted elements .....	32
Figure2.16 : The process of using Gurson or Rousselier model to assess cracked components .....	33
Figure2.17 : Modeling of ductile crack growth using computational cells.....	34
Figure 2.18: (a) Typical configuration for a dissimilar weld joint incorporating a layer of clad material. (b) Equivalent weld joint having a square groove geometry derived from the ho- mogenization approach, in which $h_e = h_w + h_c$ .....	37

Figure 31.: (a) Geometry of tested clamped SE(T) specimens for the API X80 pipeline girth weld with weld centerline notch having $a/W=0.4$ , $H/W=10$ and B×B configuration. (b) Single bevel configuration used in the preparation of the test girth weld. ....	41
Figure 32.: Engineering stress–strain data for the tested girth welds at room temperature: (a) API X80. (b) UNS N06625 alloy. (c) ASTM A106 Gr C. ....	41
Figure 33.: $J$ -resistance curves including crack growth correction for the clamped SE(T) specimens extracted from the tested girth welds: (a) API X80. (b) UNS N06625 alloy. (c) ASTM A106 Gr C girth weld. (d) ASTM A106 Gr C baseplate. ....	43
Figure 34.: (a) Geometry of weld centerline notched SE(T) specimens for the dissimilar nickel chromium girth made of UNS U06625 Alloy having $a/W=0.3$ , $H/W=10$ and B×B configuration. (b) Single bevel configuration used in the preparation of the dissimilar test girth weld. ....	45
Figure 35.: Measured load-CMOD curve for the A106 girth weld using clamped SE(T) specimens with $a/W=0.4$ : (a) Pipe material. (b) Girth weld with 35% weld strength overmatch. ....	47
Figure 4:1. Typical finite element models for stationary crack analysis of the clamped SE(T) specimen incorporating the V-groove weld configuration: (a) Plane-strain model for the X80 girth weld test geometry with $a/W=0.4$ . (b) 3-D numerical model for the UNS N06625 girth weld test geometry with $a/W=0.3$ . ....	50
Figure 4:2. Finite element models for the clamped SE(T) specimens with $a/W=0.3$ employed in the fracture testing of the UNS N06625 girth weld: (a) Half-symmetric plane-strain model. (b) Quarter-symmetric 3-D numerical model. ....	53
Figure 4.3: (a) Circumferentially cracked pipe configuration having a dissimilar Ni-Cr weld and an internal CRA clad layer under bending. (b) Narrow groove weld geometry adopted in the numerical analyses. ....	55
Figure 44.: 3D quarter-symmetric finite element model for the circumferentially cracked pipe with $a/t = 0.3$ and having a V-groove weld geometry incorporating the GT cells to describe ductile crack extension .....	56

- Figure 51.: Dependence of  $\eta$ -factors on  $a/W$ -ratio derived from plane-strain analysis incorporating the weld groove configuration and material properties for the tested girth welds: (a) Factors  $\eta$  based on CMOD. (b) Factors  $\eta$  based on LLD..... 61
- Figure 52.: Dependence of J-CTOD relationships, as characterized by parameter  $m$ , on  $a/W$ -ratio derived from plane-strain analysis incorporating the weld groove configuration and material properties for the tested girth welds..... 62
- Figure 53.: Predicted J- $\Delta a$  curves for the tested girth welds and the baseplate material using the cell size  $D/2=100\mu\text{m}$ ,  $f_N=0.5$  and  $s_N=0.05$  in all computations: (a) API X80. (b) UNS N06625 alloy. (c) ASTM A106 Gr C girth weld. (d) ASTM A106 Gr C baseplate steel. 65
- Figure 54.: CTOD-resistance curves derived from plane-strain analysis using several procedures: (a) API X80. (b) UNS N06625 alloy. (c) ASTM A106 Gr C girth weld. (d) ASTM A106 Gr C baseplate..... 66
- Figure 55.: Deformed profiles for the X80 girth weld test specimen at two different amounts of ductile tearing: (a)  $\Delta a=2\text{mm}$ . (b)  $\Delta a=4\text{mm}$ . ..... 68
- Figure 56.: (a) Distribution of  $J$  over the crack front, denoted  $J_{\text{local}}$ , with increased levels of loading for the 3-D V-groove weld model with  $a/W=0.3$  and  $0.5$ . (b) Distribution of CTOD, as defined by the  $90^\circ$  intercept procedure, over the crack front, denoted  $\delta_{\text{local}}$ , with increased levels of loading for the 3-D V-groove weld model with  $a/W=0.3$  and  $0.5$ . .... 72
- Figure 57.: (a)  $J$ -resistance curves for the UNS N06625 girth weld with new  $\eta$ -factors derived from the 3-D analysis of the V-groove weld model. (b) Predicted J- $\Delta a$  curve for the uncorrected data (without crack growth correction) using  $\epsilon_N=1.5$  and  $f_0=0.01$ . ..... 74
- Figure 58.: Comparison of CTOD resistance curves derived from the double clip gage method and J-CTOD relationship for the 3-D V-groove weld model of the UNS N06625 girth weld. .... 75
- Figure 59.: Predicted J- $\Delta a$  curves for the X80 pipeline steel tested by Bayley [138] obtained by crack growth analyses performed on the clamped SE(T) specimen using the cell size  $D/2 = 100\mu\text{m}$ ,  $f_N = 0.5$  and  $s_N = 0.05$  with  $\epsilon_N = 2.0$ ..... 76

- Figure 510.: Predicted  $J-\Delta a$  curves for the N06625 girth weld tested by Sarzosa et al. [132] obtained by crack growth analyses performed on weld centerline notched SE(T) specimens having a V-groove model and a square groove model with the cell size  $D/2 = 100\mu\text{m}$ ,  $f_N = 0.5$  and  $s_N = 0.05$  with  $\varepsilon_N = 1.5$ . ..... 77
- Figure 511.: *CTOD* resistance curves for the X80 pipeline steel derived from 3D analyses of crack extension for the clamped SE(T) specimen with  $a/W = 0.35$  and a circumferentially cracked pipe with  $a/t = 0.35$ : (a) *CTOD* determined by the extending crack tip procedure. (b) *CTOD* evaluated by the double clip-gage (DCG) method ..... 79
- Figure 512.: *CTOD* resistance curves for the UNS N06625 girth derived from 3D analyses of crack extension incorporating the V-groove model for the clamped SE(T) specimen with  $a/W = 0.3$  and a circumferentially cracked pipe with  $a/t = 0.3$ : (a) *CTOD* determined by the extending crack tip procedure. (b) *CTOD* evaluated by the double clip-gage (DCG) method. .... 80
- Figure 513.: *CTOD* resistance curves for the UNS N06625 girth derived from 3D analyses of crack extension incorporating the square groove model for the clamped SE(T) specimen with  $a/W = 0.3$  and a circumferentially cracked pipe with  $a/t = 0.3$ : (a) *CTOD* determined by the extending crack tip procedure. (b) *CTOD* evaluated by the double clip-gage (DCG) method..... 81
- Figure 514.: *CTOD* resistance curves based on the double clip-gage (DCG) method for the UNS N06625 girth derived from 3D analyses of crack extension for the circumferentially cracked pipes with  $a/t = 0.1, 0.2$  and  $0.3$ : (a) V-groove model. (b) Square groove model..... 84
- Figure 515.:  $r_P$  as a function of  $a/W$  ratios, Plastic CMOD, and material hardening levels (a) high hardening ( $n = 5$ ) (b) moderate hardening ( $n = 10$ ) (c) low hardening ( $n = 20$ ) ... 85
- Figure 516.: Predicted  $J-\Delta a$  curves for the A285 steel ..... 88
- Figure 517.:  $r_P$  variation for A285 steel ..... 89
- Figure 518.: *CTOD* based R-curves for A285 steel (a) plane strain and (b) 3D model..... 90

## List of Tables

Table 3-1: Tensile properties for the tested girth welds, including the baseplate material, in which $\sigma_{ys}$ is the yield stress (0.2% offset method), $\sigma_{uts}$ is the tensile strength and $n$ is the strain hardening exponent derived from API 579 .....	42
Table 5-1: Coefficients for the polynomial fitting of $\eta J - CMOD$ -values defined by equation 5.1 .....	64
Table 5-2: Coefficients for the polynomial fitting of $\eta J - LLD$ -values defined by equation 5.2 .....	64
Table 5-3: Coefficients for the polynomial fitting of $m$ -values defined by equation 5.3.....	66
Table 5-4: Calibrated GTN parameters and factors $q1$ , $q2$ derived from the work of Faleskog et al. [78] for all tested materials.....	67

# CHAPTER 1

## INTRODUCTION

## 1-1 Introduction

In the last decades, there has been a significant increase in oil and gas consumption. As the more easily accessible oil and gas resources are becoming depleted and, at the same time, the technology has significantly improved, the oil and gas industry is expanding its exploration and production activities into more hostile environments, including very deep water offshore hydrocarbon reservoirs. To comply with the current stringent environment-based regulations, economic development of such resources has emphasized the need of fail-safe infrastructure for reliable production and transportation of oil and natural gas. In particular, the assurance of the structural integrity of subsea pipelines and flow lines conducting larger volumes of corrosive fluids containing carbon dioxide (CO<sub>2</sub>) and hydrogen sulphide (H<sub>2</sub>S) is essential in fail-safe operations of subsea pipelines. A key approach to address this issue is by the use of API grade steel pipes either clad or mechanically lined with corrosion resistant alloy (CRA) materials, such as Ni-based alloys [1, 2], for the transport of oil and gas containing corrosive environment.

In this regard, it is crucial to ensure safe operation of pipelines which transport hydrocarbon. Defects, such as cracks, can endanger the pipeline integrity. Therefore, fitness-for-service (FFS) of pipelines were developed based on fracture mechanic to evaluate integrity of those cracked pipelines. Integrity assessment is not limited to operation time and it can cover fabrication and installation procedures.

In view of the technological importance of subsea piping systems, there has recently been a surge of interest in installing deep water steel catenary risers (SCRs) by the pipe reeling process. Here, the pipeline is first assembled at an onshore spool-base facility and then spooled onto a reel mounted on a pipe lay vessel for later deployment to the sea floor [3-6]. While faster and more effective, the reel pipe lay method subjects the pipe to large bending load and high plastic straining, well beyond its elastic limit, with a strong impact on stable crack propagation of undetected flaws at girth welds thereby potentially leading to premature pipe failure during in-service conditions.

Substantial progress has been made in recent years in developing and testing non-standard specimen geometries to measure fracture toughness data, including tearing resistance properties, more applicable to defect assessments and FFS analyses of structural components with crack-like flaws under low constraint conditions. A primary motivation



to these activities emerged from the understanding of the potential strong dependency of fracture toughness on crack geometry, loading type and material strain hardening behavior. Crack-like defects in engineering components are very often surface cracks, predominantly loaded in tension, that form during fabrication (such as weld cracks and lack of fusion) or during in-service operation (commonly in the form of fatigue cracks at weld seams or environmental cracks). These cracked components develop low levels of crack tip constraint and stress triaxiality which are not well characterized by fracture testing of standard, deep notch specimens under high constraint conditions and loaded predominantly in bending. Indeed, the rather strong differences in constraint conditions between common structural defects and standard fracture specimens, including specifically the compact tension geometry, C(T), and the single-edge notch specimen under three-point (3P) bending, SE(B), having deep cracks ( $a/W \geq 0.45 - 0.5$ ), provide a main obstacle in extending correlative fracture mechanics as a more effective engineering tool for defect assessment procedures.

A case of considerable relevance in connection with the previous arguments lies in the incorporation of the effects of ductile tearing in flaw acceptance criteria based on Engineering Critical Assessment (ECA) methodologies as structural steels commonly exhibit large increases in fracture toughness, as characterized by the J-integral [7, 8], with stable crack extension of a crack-like flaw. Experimental studies to address constraint effects on the upper-shelf fracture toughness of ferritic steels (see illustrative examples in [9, 10]) reveal a marked influence of specimen geometry, relative crack size, as characterized by the  $a/W$ -ratio, and loading mode (bending vs. tension) on crack growth resistance ( $J - \Delta a$  or, equivalently,  $CTOD - \Delta a$ ) curves (also termed R-curves). Here, the J-integral and the crack tip opening displacement ( $CTOD$  or  $\delta$ ) describe the intensity of near-tip deformation [8, 11] and  $\Delta a$  is the amount of crack growth. For the same material, deeply-cracked C(T) and 3P SE(B) specimens provide lower R-curves while shallow-notch SE(B) geometries and single-edge notch tension, SE(T), specimens yield larger toughness values at similar amounts of ductile tearing,  $\Delta a$ .

Limiting specific attention to laboratory testing of fracture specimens to characterize ductile fracture behavior under low constraint conditions, much current research now focuses on standardization efforts for fracture testing of single edge notched tension, SE(T), specimens (also often termed SENT configurations) under clamped end conditions [12, 13] to measure the crack growth resistance properties in terms of  $J - \Delta a$  or, equivalently,

$CTOD-\Delta a$  curves, for the girth weld material [11, 14]. here, the  $J$ -integral or the crack-tip opening displacement ( $CTOD$  or  $\delta$ ) describe the intensity of near-tip deformation [11, 14] and  $\Delta a$  is the amount of stable crack growth. The introduction of a low constraint geometry, as represented by the clamped SE(T) configuration, to describe the fracture resistance properties of the pipe girth weld reduces the overconservatism of FFS procedures generally based on high constraint specimen geometries (such as deeply-cracked bend, SE(B), specimens) [15-18] thereby providing a more adequate and cost-effective basis to determine the relationship between a critical flaw size and the imposed level of (remote) longitudinal strain for a given set of material properties and geometrical parameters, including the ratio of pipe diameter to wall thickness and flaw size.

Early work to develop a testing protocol for this specimen configuration centered on the evaluation of crack growth resistance curves in terms of  $J-\Delta a$  data [9,15,19] based on the unloading compliance (UC) method [20, 21]. These studies were followed by more recent efforts addressing improved procedures to evaluate  $J$  and  $\Delta a$  based on extensive finite element analyses of SE(T) specimens with varying geometries and material properties, including different mismatch conditions for weld centerline notched specimens [10,22,23-26]. However, because of the widespread use of the  $CTOD$  parameter since its introduction in the 70s, when early development conducted at the Welding Institute introduced the concept of a  $CTOD$  design curve [27, 28], current defect assessment procedures adopted by the oil and gas industry favor the utilization of  $CTOD-R$  curves rather than  $J$ -resistance measurements. Here, existing testing methodologies under development to measure crack growth resistance properties for pipeline steels often adopt a double clip gage (DCG) procedure to estimate the crack tip opening displacement ( $CTOD$ ) from experimental measurements of crack opening displacements (COD) at two different points in SE(T) specimens [29-32]. While used effectively in conventional fracture testing programs, the DCG procedure does not address explicitly the effects of stable crack growth on the relationship between remotely applied loading and crack-tip driving forces, here characterized in terms of the  $CTOD$ . Moreover, the  $CTOD$  derived from the DCG procedure is defined as the crack opening at the position of the original crack tip such that, with crack tip blunting and subsequent crack extension with increased remote loading, the position of the original crack tip falls behind the current crack tip. This features questions the proper measurement of the actual  $CTOD$  for a growing crack as well as the definition of meaningful  $CTOD$  values for use in defect assessment procedures.

## 1-2 Study Objectives

The main object of this study is to address the characterization of the *CTOD* for extending cracks in clamped SE(T) fracture specimens based upon fracture toughness tests and numerical analyses of stable crack growth (quasi static crack growth) conducted on specimen geometries extracted from pipe girth welds with different material properties. The study covers fracture resistance tests and crack growth analysis of plane strain and 3-D models for clamped SE(T) specimens with a weld centerline crack, in which a computational cell methodology to model Mode I crack extension in ductile materials is utilized to describe the evolution of  $J$  and *CTOD* with increased loading for the extending crack. Laboratory testing of girth welds made of different materials provides the measured crack growth resistance curves from which the key microstructural parameters utilized in the growth analysis are calibrated: (1) API 5L X80 pipeline steel; (2) ASTM A106 Gr C steel and (3) a typical C-Mn pipe internally clad with a nickel-chromium corrosion resistant alloy (ASTM UNS N06625 Alloy 625). Finite element analyses of a 3-D V-groove weld model for the UNS N06625 girth weld are also performed to assess 3-D effects on *CTOD* resistance curves derived from the DCG method and  $J - CTOD$  relationships. The numerical computations show relatively strong similarities between the  $J - CTOD$  relationships for stationary and growth analysis with important implications for experimental measurements of *CTOD*-resistance curves. Moreover, the present investigation shows that *CTOD* resistance curves based on the *DCG* procedure are consistently higher than the corresponding fracture resistance data based on  $J - CTOD$  relationships, thereby may potentially yield nonconservative fracture toughness estimates. The study provides a body of results which enables establishing more meaningful values of *CTOD* for use in ECA procedures incorporating SE(T) testing protocols for fracture toughness measurements. The results of this study gain sight into the functionality of R-curves derived from SE(T) specimen for actual circumferentially pipes.

## 1-3 Thesis structure

This is Chapter one, which is introduction. Then we have Chapter two which is all about literature review. Chapter three provides information about experimental studies, which is followed by chapter four regarding finite element analyses. The results of this study are presented in Chapter five and then finally, Chapter six provides a summary and conclusion.

CHAPTER 2

LITERATURE REVIEW

## 2-1 Introduction

This chapter provides a review of fundamentals of fracture mechanics and micro-mechanical model employed in integrity assessment of engineering structures. This chapter initially talks about global fracture mechanics and then local fracture mechanics. Since this study employs local fracture mechanics for ductile fracture, more details are provided in this regard.

Methods for ductile fracture are classified as non-fracture mechanics methods, classical fracture mechanics methods and modern fracture mechanics methods. The non-fracture mechanics methods are mainly developed for the assessment of ultimate capacity problems. The methods addressed in classical methods are the two popular approaches, the *R6* and *J*-integral approaches. In modern fracture mechanics methods, which are the main concern of this study, continuum damage mechanics and micromechanical model-based approaches are discussed and compared.

## 2-2 The Global Approach to Fracture

Investigating the defects' behavior based on fracture mechanics in engineering components strongly depends on the behavior of material near the crack tip. In this regard, three different approaches can be introduced. First, Linear Elastic Fracture Mechanics (LEFM) which is based on theory of elasticity and suitable for materials with very small plastic deformation near the crack tip, such as brittle materials including glass and high strength steels. Second, Elastic-Plastic Fracture mechanics (EPFM) which assumes the behavior of material (stress-strain curves) is non-linear, and there is considerable plastic deformation near the crack tip, such as low strength steels. Third, Time-Dependent fracture mechanics (TDFM) which assumes that fracture and material deformation is time dependent, such as in creep.

### 2-2-1 Linear Elastic Fracture Mechanics (LEFM)

Based on isotropic linear elasticity theories, the stress field in vicinity of the crack tip can be defined using the following infinite power series [33-35]:

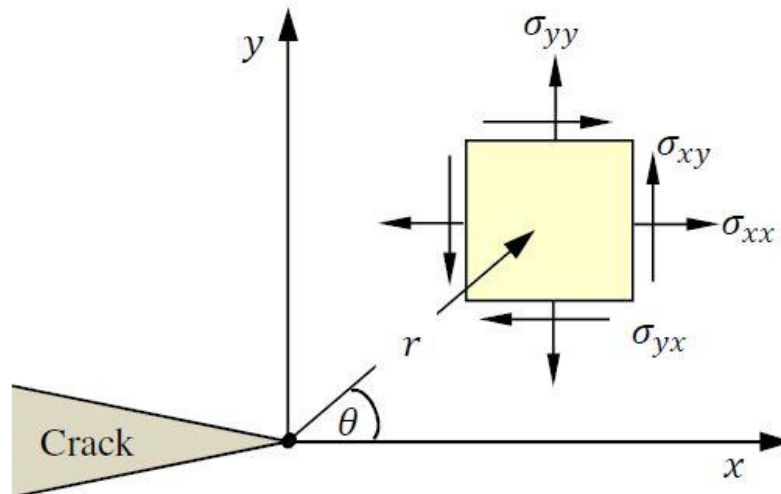
$$\sigma_{ij}(r, \theta) = \frac{k}{\sqrt{f}} f_{ij}(\theta) + A_0 g_{ij}^0(\theta) + \sum_{m=1}^{\infty} A_m r^{\frac{m}{2}} g_{ij}^m(\theta) \quad (2.1)$$

Where  $\sigma_{ij}$  is the stress tensor,  $r$  is the distance from the crack tip,  $k$  and  $A$  are constants which are proportional to the remotely applied load, and the functions  $f_{ij}$  and  $g_{ij}$  are dimensionless functions of  $\theta$  at a point defined with respect to a polar axes set located at crack tip (see figure 2.1). The second term on the right hand of equation 2.1 is known as T-stress which is a constant tensile or compressive stress acting parallel to the crack plane. The value of the T-stress depends on crack size, geometry, and the traction parallel to the crack plane; also, it has an effect on plastic zone size and crack tip opening displacement [36]. Further studies showed that compressive T-stress can reduce the crack tip constraint which is followed by an increase in fracture toughness [37-39]. Very close to the crack tip ( $r \rightarrow 0$ ), the first term on the right hand of equation 2.1 exhibits a singularity and the equation's value tends to infinity, which means the rest of the terms can be ignored and simplify the equation 2.1 as:

$$\sigma_{ij}(r, \theta) = \frac{k}{\sqrt{r}} f_{ij}(\theta) \quad (2.2)$$

Singularity-dominated zone is the region near to the crack tip where the difference between equation 2.1 and 2.2 is less than 10% [40].

Figure 2.1 : Stress tensor close to the crack tip



The  $k$  parameter (stress intensity factor) indicates the amplitude of crack tip singularity and also the mode of the loading. Generally, there are three possible modes of loading that can be applied to a crack (see figure 2.2). Any cracked body can be subjected to each of these three modes or a mixture of them where the stress field would be sum of the contributed modes (equation 2.3). Also, the stress intensity factors due to various loadings are additive as long as the mode of the loads are consistent (equation 2.4 and 2.5).

$$\sigma_{ij}^{total} = \sigma_{ij}^I + \sigma_{ij}^{II} + \sigma_{ij}^{III} \quad (2.3)$$

$$k_I^{total} = k_I^A + k_I^B + k_I^C \quad (2.4)$$

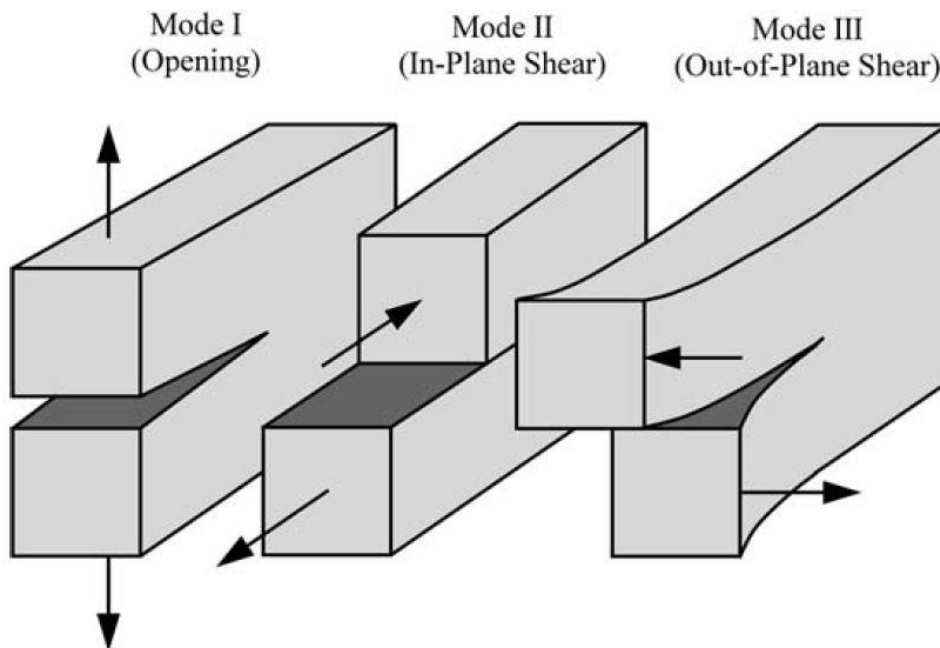
$$k_I^{total} \neq k_I + k_{II} + k_{III} \quad (2.5)$$

In many practical cases, the crack tends to grow perpendicular to the maximum opening load, which means mode I is the predominant mode. In this regard, the solution for mode I stress intensity factor,  $K_I$ , for a crack in an infinite body is as following form:

$$K_I = Y\sigma\sqrt{\pi a} \quad (2.6)$$

Where  $Y$  is a dimensionless parameter depending on the geometry and the crack,  $\sigma$  is the remotely applied stress, and  $a$  is the crack length. The values of  $K_I$  for common geometries and specimens are available in handbooks [41-43]. It should be mentioned that this solution is only valid for a crack in an infinite body, which means the crack is so small that it is not affected by external boundaries. Therefore, for small specimens, where the crack tip is affected by external boundaries, it is impossible to find a close-form solution for stress intensity factor.

Figure2.2 : Three modes of crack loading

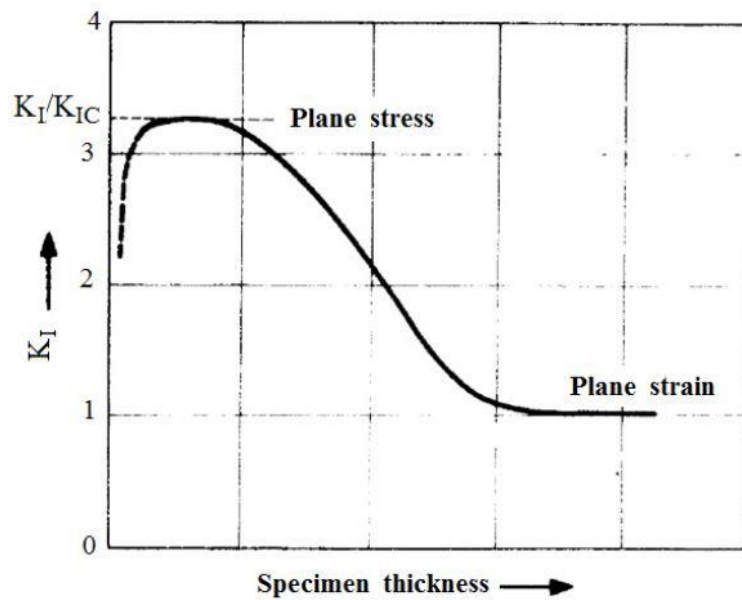


### 2-2-1-1 Crack Growth

In elastic cracked bodies, crack tends to grow when stress intensity factor holds a value larger than a critical value known as fracture toughness,  $K \geq K_c$ . Fracture toughness ( $K_c$ ) can

be identified for a material using experimental tests by applying load to a known dimension of a specimen (including the crack length) until fast fracture occurrence [44]. Fracture toughness is a material property; however, it strongly depends on specimen dimension. For instance, for mode I loading at a constant temperature, increasing the specimen thickness can reduce the fracture toughness value up to a lowest limit, known as plane strain fracture toughness ( $K_{IC}$ ). In other words, specimen is predominantly in plane strain condition. Figure 2.3 [45] shows the effect of specimen thickness on fracture toughness value.

Figure 2.3 : Effect of specimen thickness on fracture toughness value [45]



Andrianopoilos et al. (1994)

### 2-2-1-2 Crack Tip Plasticity

Linear elastic stress analysis of sharp cracks predicts singularity (infinite stresses) at the crack tip . In real materials, however, stresses at the crack tip are finite because the crack-tip radius must be finite. Inelastic material deformation, such as plasticity in metals and crazing in polymers, leads to further relaxation of crack-tip stresses. The elastic stress analysis becomes increasingly inaccurate as the inelastic region at the crack tip grows. Simple corrections to linear elastic fracture mechanics (LEFM) are available when moderate crack-tip yielding occurs. For more extensive yielding, one must apply alternative cracktip parameters that take nonlinear material behavior into account (such as  $J - Q$ ). The size of the crack-tip-yielding zone can be estimated by two methods: the Irwin approach, where the elastic stress analysis is used to estimate the elastic-plastic boundary, and the strip-yield model. Both approaches lead to simple corrections for crack-tip yielding [11].



## 2-2-2 Elastic-Plastic Fracture Mechanics (EPFM)

LEFM is valid only in cases with small nonlinear deformation surrounding the crack tip. However, in many cases where considerable nonlinear deformation exists, it is essential to employ other fracture mechanics model which is able to take in to account the effect of nonlinear deformation. J integral and Crack Tip Opening Displacement (CTOD) are two important elastic-plastic fracture parameter, each of which can describe crack tip condition in both elastic and elastic-plastic materials. It should be mentioned that J integral and CTOD [46] has their own limitation. However, their limitation is much less restrictive than LEFM limitation.

### 2-2-2-1 The J Integral

J integral was developed based on deformation theory of plasticity (nonlinear elasticity) as a fracture characterizing parameter. Rice [7] defined the J integral as a path independent line integral that its value is equal to energy release rate in nonlinear elastic cracked body. According to figure 2.4 consider an arbitrary counterclockwise path around the crack tip. The J integral is given by:

$$J = \int_{\Gamma} \left( w dy - T_i \frac{\partial u_i}{\partial x} ds \right) \quad (2.7)$$

Where  $w$  is strain energy density which is equal to  $\int_0^{\varepsilon_{ij}} \sigma_{ij} d\varepsilon_{ij}$ ,  $T_i$  are components of the traction vector,  $u_i$  displacement vector components,  $ds$  length increment along the contour  $\Gamma$ ,  $\sigma_{ij}$  and  $\varepsilon_{ij}$  are the stress and strain tensors, respectively. For linear elastic cases, J is related to K as following:

$$J = \frac{K^2}{\dot{E}} \quad (2.8)$$

Where  $\dot{E} = E$  for plane stress, and  $\dot{E} = E/(1 - \nu^2)$  for plane strain stress state.  $E$  and  $\nu$  are Young's modulus and Poisson's ratio respectively.

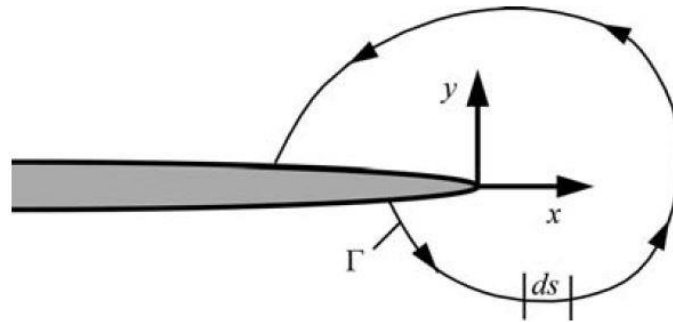
Hutchinson [47], Rice and Rosengren [48] showed that the magnitude of stress and strain near the crack tip in terms of the J integral is as equation 2.9. This solution is known as HRR singularity. They assumed that material deforms according to Ramberg-Osgood equation.

$$\sigma_{ij} = \sigma_0 \left( \frac{EJ}{\alpha \sigma_0^2 I_n r} \right)^{\frac{n}{1+n}} \tilde{\sigma}_{ij}(n, \theta) \quad (2.9a)$$

$$\varepsilon_{ij} = \frac{\alpha \sigma_0}{E} \left( \frac{EJ}{\alpha \sigma_0^2 I_n r} \right)^{\frac{n}{1+n}} \tilde{\varepsilon}_{ij}(n, \theta) \quad (2.9b)$$

Where  $\sigma_0$  is a reference stress value which usually equals to yield stress,  $\alpha$  is dimensionless constant,  $n$  is strain hardening,  $I_n$  is an integration constant which depends on  $n$ .  $\tilde{\sigma}_{ij}$  and  $\tilde{\varepsilon}_{ij}$  are dimensionless function of  $n$  and  $\theta$ . According to equation 2.9, HRR can completely characterize the crack tip stress and strain fields only by  $J$ . This means that different components (with different geometries) can have the same stress and strain field if the  $J$  values are the same. This strengthens the fact that  $J$  is a fracture parameter. As mentioned earlier, HRR is valid for both elastic and elastic plastic materials. In elastic materials, where  $n = 1$ , HRR shows a  $1/\sqrt{r}$  singularity which is consistent with LEFM. Also, for perfectly plastic materials, where  $n = \infty$ , HRR solution is equal to Prandtl slip-line solution [49].

Figure 2.4 Counterclockwise path around the crack tip for calculating  $J$  integral



### 2-2-2-1-1 Crack Growth

In EPFM, crack growth criterion is similar to LEFM. Indeed, when  $J$  value reaches a critical value, the crack starts to advance. Also,  $J_{Ic}$ , critical value of  $J$  in mode I loading for plane strain condition, is a material property since it is not related to the size of plastically deformed area [50]. In elastic condition, it is easy to calculate  $K_{Ic}$  based on  $J_{Ic}$  using equation 2.8. There are two common methods for estimating  $J_{Ic}$  using experimental tests. One of them needs multiple specimens while the other one requires only one specimen. Further details of two methods are available in ASTM standard for fracture toughness measurement [51].

### 2-2-2-2 Crack Tip Opening Displacement (CTOD)

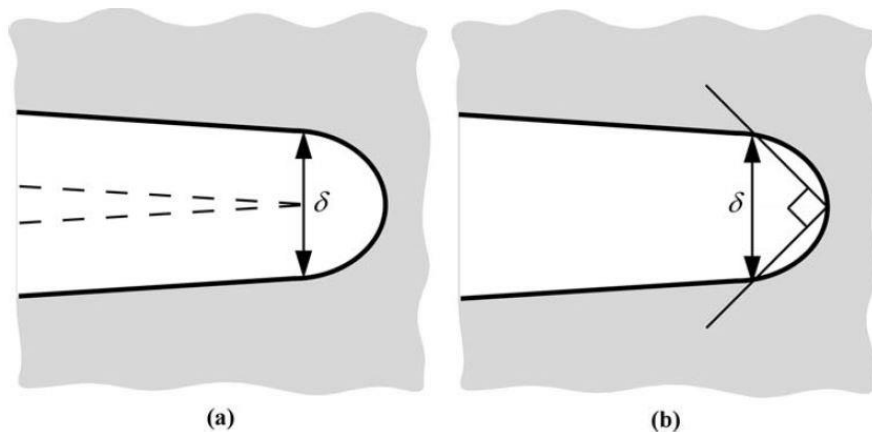
Initially Wells [46] attempted to measure the  $K_{Ic}$  for some structural steels. He found that LEFM was not the suitable method for those steels since they were so tough that crack faces moved apart prior to fracture. Therefore, he concluded that CTOD can be used to measure the

fracture toughness when LEFM is no longer valid. Shih [52] confirmed this by providing a relationship between J and CTOD as following:

$$\delta = \frac{J}{m\sigma_f} \quad (2.10)$$

Where  $\delta$  is CTOD,  $m$  is a proportionality coefficient that strongly depends on the material strain hardening ( $n$ ), but weakly sensitive to crack size, and  $\sigma_f$  represents the flow stress defined by  $\sigma_f = (\sigma_{ys} + \sigma_{uts})/2$  in which  $\sigma_{ys}$  and  $\sigma_{uts}$  denote the yield stress and the tensile strength. There are two common definitions for CTOD which are the displacement at the original crack tip and the intersection of a  $90^\circ$  vertex with crack flanks, as shown in figure 2.5. Rice [7] suggested the later definition which is proper method to calculate CTOD in finite element analysis.

Figure 2.5 : Two definition for CTOD: a) the displacement at the original crack tip, b) the intersection of a  $90^\circ$  vertex with crack flanks



### 2-2-2-3 The Material Resistance Curve (R-Curve)

Many tough materials not only do not fail catastrophically at a particular J or CTOD value, but also show higher resistance to crack growth with crack advance (see figure 2.6). This is why crack growth resistance curves (R-curve) were developed to assess the crack growth in cracked components with high toughness. The R-curve represent the relation between crack driving force (J or CTOD) and crack extension, the so called J-R or CTOD-R curve. As mentioned earlier, fracture toughness may vary due to different specimen size (different level of constraint [53,54]) as R-curves do (see figure 2.7). In other words, after crack growth initiation, the slope of R-curves tend to decrease due to increase in crack tip constraint [55]. Therefore, due to the fact that most of R-curves are obtained from standard specimens in laboratory, the effect of constraint due to geometry must be considered so that the R-curves

can be applicable for real components. In this regard, two parameter fracture mechanics, such as  $J - T$  approach [56],  $J - Q$  theory [57,58], and  $J - A_2$  method [59] were developed.  $J - Q$  theory and  $J - A_2$  method have been used widely for characterizing constraint effect under large scale yielding condition [60]; however,  $J - T$  approach has a limited application in elastic-plastic fracture mechanics since it is based on theory of elasticity. It should be mentioned that in small scale yielding condition, the J-R curve is a material property since the J value depends only on crack extension [11].

Figure 2.6 : Higher resistance to crack growth with crack advance

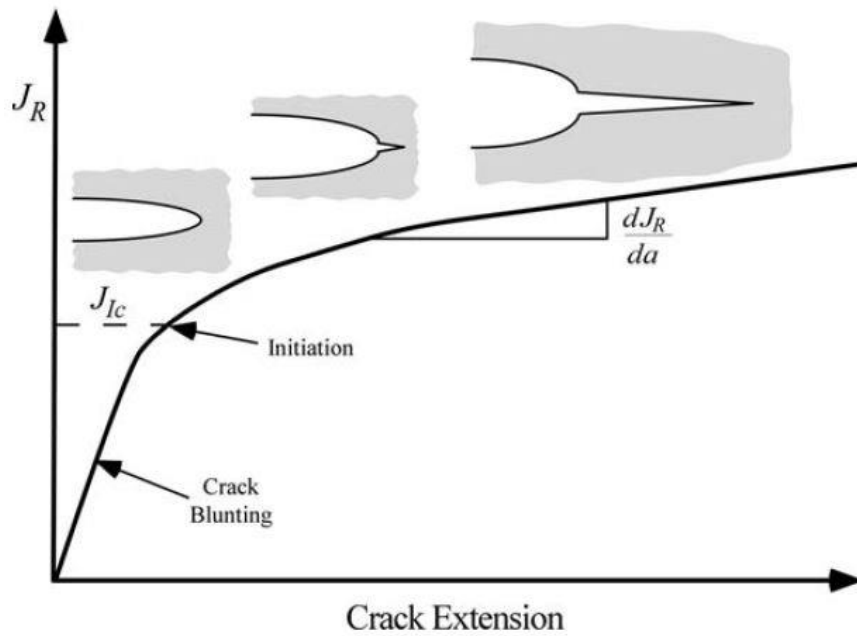
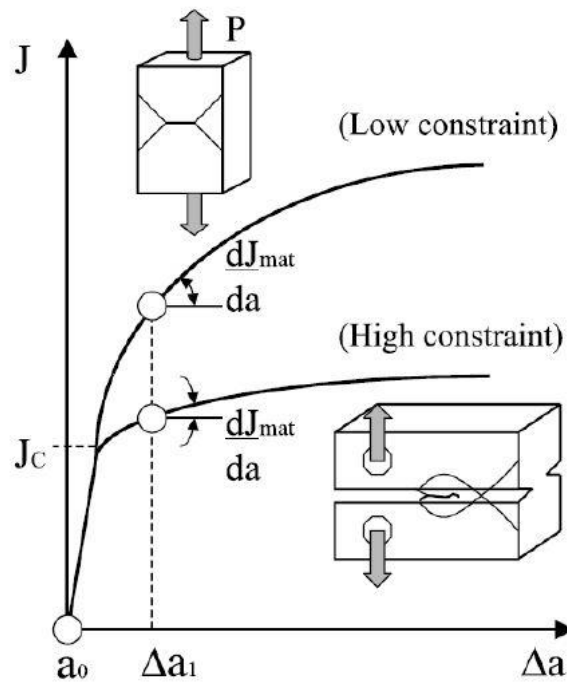


Figure 2.7 : The effect of constraint on R-curve



### 2-2-2-3-1 Evaluation procedure of R-Curves

This section describes the procedure of determining resistance curves for common fracture specimens, including SE(T) and SE(B), using experimental tests and analytical framework. The methodology is based on the unloading compliance (UC) technique using a single

specimen test to determine the instantaneous value of the specimen compliance at partial unloading during the measurement of the load vs. displacement curve. This technique enables accurate estimations of  $J$  (or  $\delta$ ) and  $\Delta a$  at several locations on the load-displacement records from which the  $J$ -R and  $\delta$ -R curves can be developed.

- **Evaluation procedure of  $J$  using  $\eta$ -factor**

In order to estimate crack driving force,  $J$  integral, with stable crack growth, it is wise to take advantage of an incremental procedure which updates the  $J$  in terms of its elastic,  $J_e$ , and plastic,  $J_p$ , parts at each partial unloading point, denoted by  $k$  (see equation 2.11), during the measurement of load vs. displacement curve as shown in figure 2.8. Equation 2.12 calculates the elastic part of  $J$ .

$$J^k = J_e^k + J_p^k \quad (2.11)$$

$$J_e^k = \left( \frac{K_I^2}{\dot{E}} \right)_k \quad (2.12)$$

Where  $K_I$  is the elastic stress intensity factor for the cracked body at the  $k$ -th unloading point,  $\dot{E} = E/(1 - \nu^2)$ , where  $E$  and  $\nu$  are (longitudinal) elastic modulus and Poisson's ratio, respectively. There are studies [19, 42] that provide solutions for  $K_I$  for SE(T) and SE(B) specimens.

The procedure to estimate the plastic term,  $J_p$ , adopted an incremental equation. This equation is based on Load-Load line Displacement (LLD) records which derives from Ernst et al. [61] study. Also, it is possible to estimate the  $J_p$  using Load-Crack Mouth opening Displacement (CMOD) records. In this regard, Cravero and Ruggieri [62] and Zhu et al. [63] introduced an incremental procedure as following:

$$J_p^k = \left[ J_p^{k-1} + \frac{\eta_{J-CMOD}^{k-1}}{b_{k-1}^{BN}} (A_p^k - A_p^{k-1}) \right] \cdot \Gamma_k \quad (2.13)$$

With  $\Gamma_k$  defined by

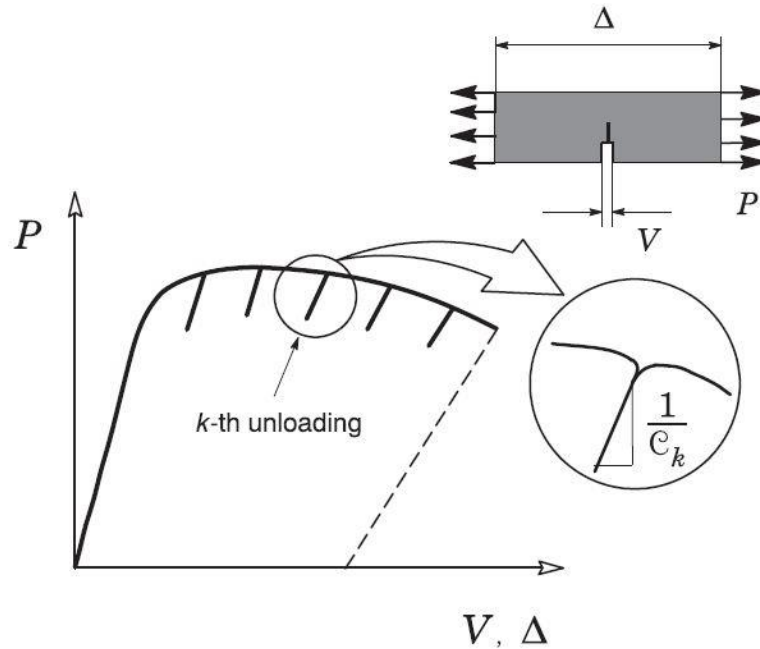
$$\Gamma_k = \left[ 1 - \frac{\gamma_{LLD}^{k-1}}{b_{k-1}} (a_k - a_{k-1}) \right] \quad (2.14)$$

With  $\gamma_{LLD}$  defined by

$$\gamma_{LLD} = \left[ -1 + \eta_{J-LLD}^{k-1} - \left( \frac{b_{k-1}}{W\eta_{J-LLD}^{k-1}} \frac{d\eta_{J-LLD}^{k-1}}{d(a/w)} \right) \right] \quad (2.15)$$

Where  $A_p$  represents the plastic area under the load-displacement curve,  $B_N$  is the net specimen thickness at the side groove roots ( $B_N = B$  if the specimen has no side grooves where  $B$  is the specimen gross thickness),  $a$  is the crack length,  $b$  denotes the uncracked ligament ( $b = W - a$  where  $W$  is the width of the cracked configuration and  $a$  is the crack length). Factor  $\eta$  represents a nondimensional parameter which relates the plastic contribution to the strain energy for the cracked body with  $J$ . It is also noted that  $A_p$  (and consequently,  $\eta_J$ ) can be defined in terms of load-load line displacement (LLD or  $\Delta$ ) data or load-crack mouth opening displacement (CMOD or  $V$ ) data and, thus, the corresponding quantities are referred to as  $\eta_{J-LLD}$  and  $\eta_{J-CMOD}$  in the present study. The term  $\Gamma_k$  in equation 2.13 corrects the measured load-displacement records for crack extension [11, 61, 64].

Figure 2.8 : Partial unloading during the evolution of load with displacement



- **$\eta$ -Factor**

According to equations 2.13 and 2.15, it is essential to estimate plastic  $\eta$ -factor in order to calculate the  $J$  value. Finite element analysis of selected fracture specimens is widely used in literature [65-67] to calculate plastic  $\eta$  factor. Most of them are applicable for materials obeying

power hardening model in which the relation between logarithmic strain ( $\bar{\epsilon}$ ) and uniaxial true stress ( $\bar{\sigma}$ ) is as equation 2.16.

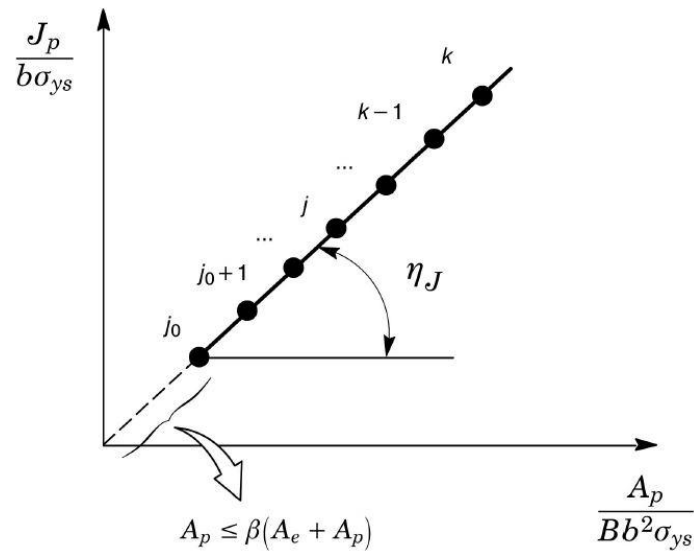
$$\frac{\bar{\epsilon}}{\epsilon_{ys}} \propto \left( \frac{\bar{\sigma}}{\sigma_{ys}} \right)^n \quad (2.16)$$

where  $\epsilon_{ys}$  and  $\sigma_{ys}$  are yield strain and yield stress respectively, and  $n$  is the Ramberg-Osgood strain hardening exponent.

FRACTUS2D [56] is employed to calculate  $\eta$ -factor, which employs a standard linear regression over discrete points in the load steps (see figure 2.9). Note that according to the numerical scheme, the initial load step,  $j_0$ , is defined as the one at which  $A_p = \beta(A_e + A_p) = \beta A_t$  where  $\beta = 0.1$  is adopted. The solution that is adopted by FRACTUS2D [56] is based on following equation which is derived from equations 2.10 and 2.13.

$$\frac{J_p}{b\sigma_{ys}} = \frac{\eta J A_p}{B b^2 \sigma_{ys}} \quad (2.17)$$

Figure 2.9 : Numerical scheme based on a standard linear regression performed over discrete points in the load step range defined between  $j_0$  and  $k$  to determine the  $\eta$ -factor.



- **Evaluation of J using finite element analyses**

A method for calculating J using finite element framework was provided by Shih et al. [69]. According to this method, the domain integral expression of equation 2.7 is obtained by introducing a smooth function,  $q$ , which take the value of unity at the crack tip nodes and zero on the contour  $\Gamma$  and then applying the divergence theorem to give:



$$J = \int_{A^*} \left\{ \left( \sigma_{ij} \frac{\partial u_j}{\partial x_1} - w \delta_{1i} \right) \frac{\partial q}{\partial x_i} \right\} dA \quad (2.18)$$

Where  $A^*$  is the enclosed area by  $\Gamma^* = \Gamma_1 + \Gamma_+ + \Gamma_- - \Gamma_0$  in a 2D problem as shown in figure 2.10. The  $q$  function, which is as following equation, must be specified at all nodes inside the integration area.

$$q = \sum_{I=1}^n N_I Q_I \quad (2.19)$$

Where  $n$  is the number of nodes per element,  $N_I$  is the shape function, and  $Q_I$  are the nodal values for the  $I^{th}$  node. The special derivative of  $q$  in equation 2.18 is as following:

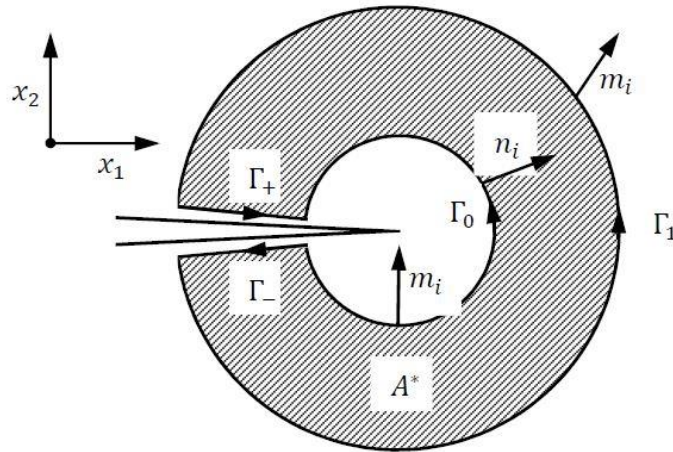
$$\frac{\partial q}{\partial x_i} = \sum_{I=1}^n \sum_{k=1}^2 \frac{\partial N_I}{\partial \xi_k} \frac{\partial \xi_k}{\partial x_j} Q_I \quad (2.20)$$

where  $\xi_k$  represents the local coordinates ( $\xi_1, \xi_2$ ) and  $\frac{\partial \xi_k}{\partial x_j}$  is the inverse Jacobian matrix of the transformation. With  $2 \times 2$  Gaussian integration, the domain integral expression of  $J$ -integral in equation 1 for the plane problem is as following:

$$J = \sum_{All \ elements \ in \ A^*} \sum_{p=1}^m \left\{ \left[ \left( \sigma_{ij} \frac{\partial u_j}{\partial x_1} - w \delta_{1i} \right) \frac{\partial q}{\partial x_i} \right] \det \left( \frac{\partial x_j}{\partial \xi_k} \right) \right\}_p w_p \quad (2.21)$$

Where  $m$  is the number of gauss points per element, and  $w_p$  is weighting factors. All quantities inside the  $\{ \}_p$  must be calculated at all gauss points in an element. It should be mentioned that integration over the crack faces is necessary only when there are non-zero tractions.

Figure 2.10 : J integral contour around the crack tip



- Evaluation procedure of CTOD

To the extent that  $J$  describes the crack tip condition,  $J - R$  and  $CTOD - R$  both can characterize the crack growth resistance curve well, since there is a unique relationship between  $J$  and  $CTOD$  (see equation 2.10). According to equation 2.10 which relates the  $J$  to the total value of  $CTOD$ , the  $CTOD$  can be advantageously determined by calculating  $J$  using load vs. CMOD curve. This equation simplifies the evaluation of  $CTOD$  values, however, relying on a rigorous energy release rate definition of  $J$  for a cracked body. ASTM 1820 [70] is the most widely used  $CTOD$  evaluation procedure.

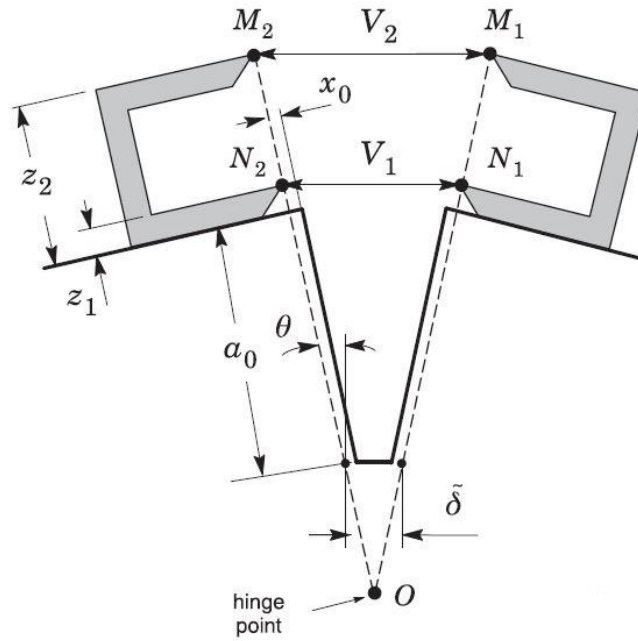
Although it is proved that equation 2.10 is an effective procedure to estimate  $CTOD$ , its accuracy strongly depends on accurate evaluation of  $J$ , and therefore  $\eta$ -factor, and  $m$ . In this regard, a double clip gage arrangement was developed based on a plastic hinge concept to simply estimate  $CTOD$  by knowing crack opening displacement ( $COD$ ) at two different point, as shown is figure 2.11. According to figure 2.11 two knife edgea are attached to the each side of the notch, which enables the measurement of displacement at knife edge position using two clip-gages. This fixture, double clip-gage (DCG), is recommended by recent test procedures to estimate SE(T) specimen R-curves [30, 32].

As shown in figure 2.11, the  $DCG$  mounting fixture is usually installed at distance  $x_0$  from crack flange, which causes an apparent offset from crack flank since only when  $x_0 = 0$  the  $DCG$  fixture is aligned with crack flank. This offset from crack flank increases the measured  $CTOD$ , denoted by  $\delta$ . In the test procedures, it is possible to correct the measured  $CTOD - R$  curve for different values of  $x_0$ . Moreover, the  $DCG$  procedure assumes a rigid rotation of the crack flanks, from crack tip to crack mouth, around a hinge point in the crack ligament. This assumption also may lead to an apparent increase of measured  $CTOD$  values. An equation based on trigonometric relations was developed for estimating  $CTOD$  using  $DCG$  procedure as following:

$$\delta = V_1 - \frac{z_1 + a_0}{z_2 - z_1} (V_2 - V_1) \quad (2.22)$$

Where  $V_1$  and  $V_2$  are  $COD$ -values,  $z_1$  and  $z_2$  are the orthogonal distance of measuring points for  $V_1$  and  $V_2$  from crack mouth, and  $a_0$  is the initial crack length (not the current crack size). Note that equation 2.16 calculates the  $CTOD$  at the position of the original crack tip. Sarzosa et al. [71] discuss the effect of extending crack on the  $CTOD$ .

Figure 2.11 : Double clip-gage method to estimate the CTOD using measurements of crack opening displacements (COD) at two different points.



Plastic hinge models is another method to measure the CTOD which assumes a constant point at distance  $b \cdot r_p$  from crack tip at crack ligament around which the specimen rotates. This assumption is correct for deeply cracked SE(B) specimen where  $r_p=0.4$  is suggested. This method takes advantage of estimating elastic and plastic portion of CTOD as shown in following equation. This means that knowing  $r_p$  value enables us to calculate CTOD. However, in many specimens plastic rotational factor ( $r_p$ ) is not constant and changes. Sebastian Cravero, Claudio Ruggieri 2007 show that  $r_p$  varies with increasing CMOD for pin loaded SE(T) fracture specimen and it strongly depends on strain hardening for shallow cracked specimen.

$$\begin{aligned} \delta_{disp} &= \delta_{disp,el} + \delta_{disp,pl} \\ &= \frac{K_0^2(1-\nu^2)}{2R_{p0.2b}E} + \frac{r_{pl}(W-a_0)V_{pl}}{r_{pl}(W-a_0)+a_0+z} \end{aligned} \quad (2.23)$$

Where  $\delta_{disp,el}$  is the elastic part of  $\delta_{disp}$ ,  $\delta_{disp,pl}$  is the plastic part of  $\delta_{disp}$ ,  $K_0$  is the stress intensity factor,  $\nu$  is Poisson's ratio,  $E$  is Young's modulus,  $R_{p0.2b}$  is the 0.2% offset yield strength,  $r_{pl}$  is the plastic rotational factor,  $V_{pl}$  is the plastic part of CMOD,  $a_0$  is the initial crack length and  $z$  is the distance of the knife edge measurement point from the front face on specimens.

#### 2-2-2-4 The J-Q Theory

Constraint can be the main answer to explain why different fracture specimen or engineering components show different fracture toughness. Indeed, by increasing the load, the small scale yielding (SSY) fields tend to diminish and crack tip plastic zone size tend to increase leading to large scale yielding (LSY) fields. Now the stresses relax below the values determined only based on J-integral for high constraint SSY condition. In other words, there is no more unique relationship between J-integral and crack tip fields due to constraint loss. This means that the crack tip fields cannot be determined only based on J-integral.

Following what mentioned in previous paragraph, O'Dowd and Shih [57, 58] proposed a two parameter description, J integral and constraint, for crack tip fields which is applicable under LSY condition even.

#### 2-2-3 Failure Assessment Diagram (FAD)

In 1975, Dowling and Townley [72] introduced the two-criterion approach to investigate the integrity of defected components. According to this approach, the component may fail due to either brittle fracture or plastic collapse. Indeed, integrity assessment not only should assess the cracked component using fracture mechanics, but also must take into account the possibility of plastic collapse before brittle fracture. Failure Assessment Diagram (FAD) was developed to consider both types of failure in integrity assessment procedure using Failure Assessment Curve (FAC) which is established based on a relationship between fracture condition and a limit load solution describing the plastic collapse of the crack ligament [43, 73, 74]. The following equation defines the FAC:

$$K_r = f_i(L_r) \quad (2.24)$$

Where the  $K_r$  and  $L_r$  are the fracture and load ratios respectively, and their value depends on the applied load, specimen geometry (defect shape and size), and the material properties (see equation 2.19). The subscript  $i=1, 2, 3$  indicates the level of failure assessment. Higher level of assessment means more accuracy which obviously requires more data and analysis.

$$K_r = \frac{K_I(a,P)}{K_{mat}} \quad (2.25a)$$

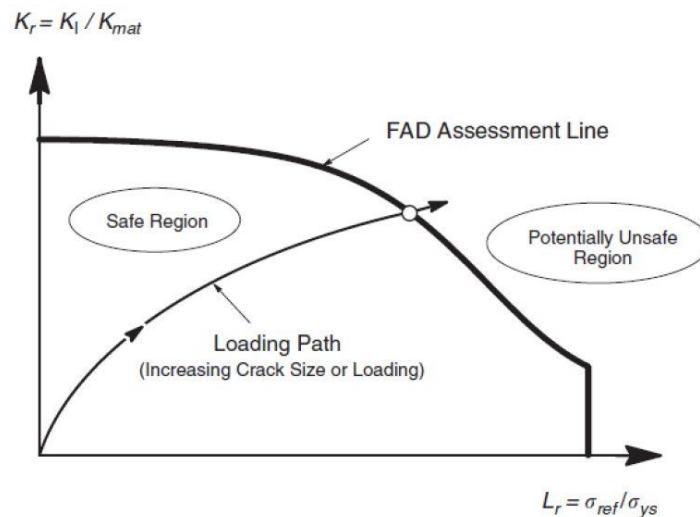
$$L_r = \frac{P}{P_L(a, \sigma_y)} \quad (2.25b)$$

Where ,  $K_I$  is the mode I stress intensity factor at load  $P$ ,  $K_{mat}$  is material's fracture toughness,  $a$  is the crack size,  $P_L$  is the value of  $P$  corresponding to plastic collapse of the cracked component and  $\sigma_y$  is the yield strength of material. The  $L_r$  can also be calculated using a reference stress ( $\sigma_{ref}$ ) defining the plastic collapse load of the crack ligament as following [75]:

$$L_r = \frac{\sigma_{ref}}{\sigma_y} \quad (2.26)$$

In order to assess the integrity of defected component it is essential to initially calculate the  $K_r$  and  $L_r$  values, and thereby assessment point  $(L_r, K_r)$ , and then see whether the component is safe or not by checking the relative position of assessment point on FAD. If the assessment point is inside the safe area of the FAD, the structure is safe, otherwise not (see figure 2.12).

Figure2.12 : Failure Assessment Diagram (FAD)



As mentioned earlier, there are three levels of assessment. The first level ( $i=1$ ), the simplest one, can be employed for general applications, and when there is only limited available information on material properties (only yield stress ( $\sigma_y$ ) and ultimate stress ( $\sigma_{uts}$ ) are required). In this case FAC function is as:

$$f_1(L_r) = (1 - 0.14L_r^2)[0.3 + 0.7\exp(0.65L_r^6)] \quad (2.27)$$

$$L_r = L_r^{max} = \frac{\sigma_y + \sigma_{uts}}{2\sigma_y} \quad (2.28)$$

Be careful that if stress-strain curve is discontinuous at yield point, either a cut-off value for  $L_r \leq 1$  or level 2 assessment should be used. Level 2 assessment requires more details of stress-strain curve, and therefore it is applicable for all types of materials. The FAC for level 2 is as following:

$$f_2(L_r) = \left( \frac{E\varepsilon_{ref}}{\sigma_{ref}} + \frac{L_r^3 \sigma_y}{2E\varepsilon_{ref}} \right)^{-1/2} \quad (2.29)$$

Where  $\varepsilon_{ref}$  is the true strain obtained from the uniaxial tensile stress-strain curve at a true stress level  $\sigma_{ref}$ .

Level 3 assessment is the most advanced assessment which is suitable for assessing ductile fracture (stable crack growth). This level of assessment takes advantage of J integral which enables elastic-plastic analysis of defected component. Indeed, this level is based on criterion  $J \leq J_{mat}$  [49]. In this level it is essential to initially find the FAC for a specific component (with a specific geometry and material). And then, assess the component using only  $J_e$ . The FAC for level 3 is as following:

$$f_3(L_r) = \sqrt{\frac{J_e}{J}} \quad (2.30)$$

Where  $J_e$  and  $J$  are J integral values obtained from elastic and elastic-plastic analyses under the same loading. The  $K_r$  for this level is as following:

$$K_r = \sqrt{\frac{J_e}{J_{mat}}} \quad (2.31)$$

Where  $J_{mat}$  is the material toughness.

- **Assessment under combined primary and secondary stress**

Some of the engineering components are under combined primary and secondary stresses. Primary stresses arise from loads which contribute to plastic collapse, such as pressure. And secondary stresses are self-equilibrating stresses originated from a range of sources, such as thermal and residual stress due to welding.

FAD calculates  $L_r$  and FAC only using primary stress, while calculates  $K_r$  using both primary and secondary stresses. In this regard, in elastic cases,  $K_r$  is equal to the sum of stress intensity due to primary stress ( $K_I^P$ ) and secondary stress ( $K_I^S$ ). However, in elastic-plastic

cases, considering plasticity, this superposition is not accurate enough since it is underestimate. To address this issue, an additive parameter  $\rho$  which its value depends on the magnitude of the both primary and secondary stresses, is applied to the  $K_r$  definition as following:

$$K_r = \frac{K^p + K^s}{K_{mat}} + \rho \quad (2.32)$$

Appendix 4 of R6 provides routes for calculating  $\rho$ .

### 2-3 The Local Approach to Fracture

The local approach is a method for investigating the failure of steel components. This method which does not use fracture mechanics parameters, is widely used in literature to assess the integrity of various geometries made by both ferritic and austenitic steels under combined primary and secondary stresses [76-81]. Also, this approach can be used both for ductile and brittle fracture.

This approach is based on micro-mechanical models of failure. Indeed, failure occurs when stress and/or strain close to crack tip reaches a critical condition. These models need to be calibrated using experimental data, quantitative metallography, and finite element analysis. When a model parameters are calibrated for a specific material, it can be applied to different components with different geometries made of the same material [74].

This study focuses on ductile fracture, in which plastic deformation is not ignorable. It is common for elastic-plastic materials to use a pressure independent plasticity model which assumes that plastic deformation does not depend on hydrostatic stress and only depends on shear stress (deviatoric stress). Although this is experimentally well verified, it is not valid for ductile fracture due to existence of micro voids in ductile materials. Studies [82, 83] have indicated that hydrostatic stress can cause softening effect due to growth of micro voids. Therefore, plasticity models can be divided into two groups which are pressure independent such as von Mises and pressure dependent models such as Gurson model [84, 85] and Rousselier model [86, 87] where stress triaxiality is incorporated.

#### 2-3-1 Gurson-Tvergaard-Needleman model for dilatant plasticity

In 1979, Gurson [73, 74] proposed the following yield function as a dilatant plasticity model for porous materials with a single spherical void, based on Rice and Tracy [72] work.

$$\varphi(\sigma_e, \sigma_m, \sigma_f, f) = \left(\frac{\sigma_e}{\sigma_f}\right)^2 + 2f \cosh\left(\frac{3\sigma_m}{2\sigma_f}\right) - 1 - f^2 = 0 \quad (2.33)$$

Where

$\sigma_e$  is effective von Mises stress

$\sigma_m$  is the mean stress, i.e., hydrostatic stress

$\sigma_f$  is flow stress of the matrix material

$f$  is the current void volume fraction which is equal to  $\frac{V_{void}}{V_{matrix}}$ . The setting of  $f=0$  recovers the classic von Mises yield function due to fully dense and incompressible material.

Later on, in 1981, Tvergaard [88] (the so-called ‘GT model’) improved the Gurson model by introducing three q-factors, to take into account the interaction effects for periodic arrays of cylindrical and spherical voids, to the model. The following equation shows the developed model by Tvergaard:

$$\varphi(\sigma_e, \sigma_m, \sigma_f, f) = \left(\frac{\sigma_e}{\sigma_f}\right)^2 + 2q_1 f \cosh\left(\frac{3q_2 \sigma_m}{2\sigma_f}\right) - 1 - q_3 f^2 = 0 \quad (2.34)$$

Where

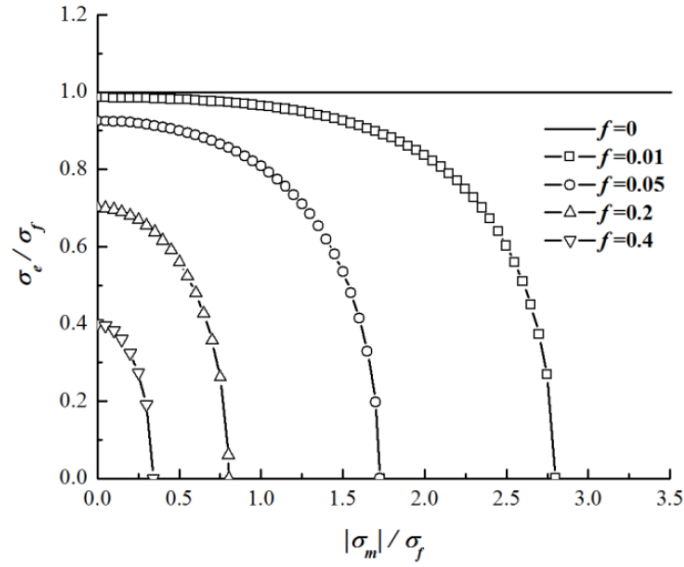
$$q_1 = 1.5, q_2 = 1.0, \text{ and } q_3 = q_1^2$$

q-factor values were calibrated by matching numerical results with experimental results in plane strain tensile fields. Note that the setting of all three q-factors equal to one, recovers the original Gurson model. In 1997, Faleskog and Shih [89, 90] improved q-values using material flow properties including strain hardening and yield stress.

Figure 2.13 shows the yield surfaces using GT model for different values of void volume fraction, where yield surface is a point if  $f$  reaches the limit  $\frac{1}{q_1}$ . However, the limit  $\frac{1}{q_1}$  is too large to be realistic in practice to simulate the final material failure [91]. This is due to the fact that, the GT model, can model the softening of the material due to void growth; however, it cannot incorporate void coalescence to capture loss of load-carrying capacity at smaller values of the  $f$  than that limit. In this regard, Tvergaard and Needleman [92] developed the GT model and proposed the ‘Gurson-Tvergaard-Needleman model’ (GTN model) by replacing  $f$  by  $f^*$ , and introducing critical void volume fraction ( $f_c$ ) at which voids coalesce. The GTN model is as follows:



Figure 2.13 : Yield surface dependence on the hydrostatic tension and porosity



$$\varphi(\sigma_e, \sigma_m, \sigma_f, f^*) = \left(\frac{\sigma_e}{\sigma_f}\right)^2 + 2q_1 f^* \cosh\left(\frac{3q_2 \sigma_m}{2\sigma_f}\right) - 1 - q_3 f^{*2} = 0 \quad (2.35a)$$

$$f^* = \begin{cases} f & (f \leq f_c) \\ f_c + \delta_a (f - f_c) & (f > f_c) \end{cases} \quad (2.35b)$$

Where

$$\delta_a = \frac{f_u^* - f_c}{f_F - f_c} \quad (2.35c)$$

$$f_u^* = \frac{1}{q_1} \quad (2.35d)$$

It should be mentioned that in order to keep numerical stability, the product of  $f_u^* q_1$  in practical applications may not be equal to one [93]. As mentioned before, macroscopic ductile fracture is due to the nucleation, growth and coalescence of micro-voids. The following sections provide more details about each stage of macroscopic ductile fracture.

### 2-3-1-1 Void growth and nucleation

The change of void volume fraction is partly due to growth of existing voids, and partly due to nucleation of new voids. Therefore, the increase of void volume fraction can be written as follows:

$$\dot{f} = \dot{f}_{growth} + \dot{f}_{nucleation} \quad (2.36)$$

Where  $\dot{f}_{growth}$  and  $\dot{f}_{nucleation}$  indicates the change of void volume fraction due to growth of existing voids and nucleation of new voids, respectively. Considering the plastic incompressibility of matrix material and the law of the mass conservation, the growth of existing voids can be expressed as:

$$\dot{f}_{growth} = (1 - f)\dot{\boldsymbol{\epsilon}}^p : \mathbf{I} \quad (2.37)$$

Where  $\dot{\boldsymbol{\epsilon}}^p$  is plastic strain increment tensor and  $\mathbf{I}$  is the second-order unit tensor.

Experimental studies have shown that the nucleation of new voids occurs mainly at second phase particles by particle fracture or decohesion of the particle-matrix interface [94]. Nucleation of new voids can be stress-controlled and/or strain-controlled. It is common to assume an initial void volume fraction ( $f_0$ ) at beginning of the analysis due to the fact that nucleation of large second phase particles usually occurs at low level of stress state, below the peak stress ahead of the crack tip [95], at the beginning of the plastic deformation [96]. Therefore, note that replacing large particles by  $f_0$  has a negligible effect on material toughness. The following equation is a nucleation model [97] which nucleates secondary small voids using increment of strain and stress [93]:

$$\dot{f}_{nucleation} = A_1 \dot{\boldsymbol{\epsilon}}_{eq}^p + A_2 (\dot{\sigma}_f + \dot{\sigma}_m) \quad (2.38)$$

Where

$A_1$  and  $A_2$  are void nucleation intensity, both of which are dependent on deformation and hydrostatic stress history [98];

$\dot{\boldsymbol{\epsilon}}_{eq}^p$  is the equivalent plastic strain increment in the matrix material;

$\dot{\sigma}_f$  is the flow stress increment;

$\dot{\sigma}_m$  is the hydrostatic stress increment.

As mentioned earlier, nucleation of new voids can be stress-controlled ( $A_1 = 0$  and  $A_2 \neq 0$ ), strain-controlled ( $A_1 \neq 0$  and  $A_2 = 0$ ), or a mixture of both ( $A_1 \neq 0$  and  $A_2 \neq 0$ ). According to stress-controlled void nucleation criterion, void nucleation only depends on the maximum stress in the matrix-particle interface. Note that the use of stress-controlled nucleation is usually accompanied by numerical difficulties. This is due to the fact that void nucleation (positive increment in porosity) may be followed by a reduction in effective stress (negative increment in stress) [99]. The stress-controlled nucleation model is as follows:

$$A_2 = \frac{f_{N2}}{S_N \sigma_{YS} \sqrt{2\pi}} \exp \left[ -\frac{1}{2} \left( \frac{\sigma_f + \sigma_m - \sigma_N}{S_N \sigma_{YS}} \right)^2 \right] \quad (2.39)$$

Where

$f_{N2}$  is the void volume fraction of nucleating particles;

$\sigma_{YS}$  is the 0.2%-offset yield strength of the material.

For strain-controlled void nucleation, two models can be found in the literature: 1- the continuous nucleation model [100, 101] where  $A_1$  is a constant, 2- normal distribution of void nucleation by Chu and Needleman [98]. The model proposed by Chu and Needleman is as follows:

$$A_1 = \frac{f_{N1}}{S_N \sqrt{2\pi}} \exp \left[ -\frac{1}{2} \left( \frac{\varepsilon_{eq}^p - \varepsilon_N}{S_N} \right)^2 \right] \quad (2.40)$$

Where

$f_{N1}$  is the void volume fraction of nucleating particles;

$\varepsilon_N$  is the mean strain for void nucleation;

$S_N$  is the corresponding standard deviation;

These three parameters depend on material properties and loading conditions (geometry and stress status). Due to difficulties in determining these parameters, many studies [102-104] used the same values for  $\varepsilon_N$  and  $S_N$  as Tvergaard and Needleman used earlier [92]. In this regard, Ruggieri et al. [95] conducted extensive analysis on unit cell model and found that  $\varepsilon_N$  has the most prominent effect. It should be mentioned that strain-controlled nucleation is widely used in the literature. Also, using strain-controlled nucleation is numerically more convenient due to the monotonically increasing of plastic strain as a function of time.

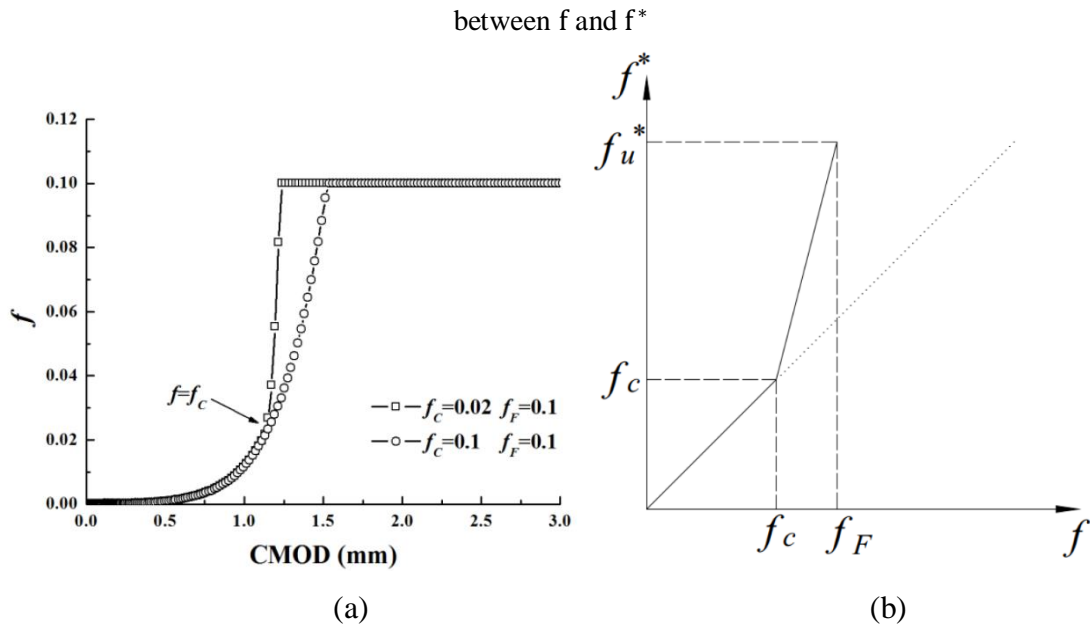
Considering a wide range of particle sizes in the material, the mixed nucleation criterion is more realistic. Generally, large particles begin to nucleate at low level of stress at the beginning of loading and nucleation (stress-controlled). However, later on, smaller particles tend to nucleate at intermediate and final stages of loading following strain-controlled nucleation criterion.

### 2-3-1-2 Void Coalescence

As voids grow and new voids nucleate, void coalescence occurs due to plastic flow localization in the material between the voids. Void coalescence is commonly accompanied by large increase in void volume fraction and reduction in stress carrying capacity. Note that void nucleation in small particles occurs at large plastic strains and therefore it does not affect the peak stress significantly. Three void coalescence criteria can be found in the literature including: 1- the critical void volume fraction [92] 2- Thomasons's plastic limit load [94] 3- traction-separation criteria [95, 102]. The following paragraphs provide details about these three coalescence criteria.

According to the critical void volume fraction model [92], void coalescence is modeled by acceleration of void volume growth when critical void volume ( $f_c$ ) reaches (see equations 4). Failure occurs when failure void volume fracture ( $f_F$ ) is reached. The evolution of void volume fraction with and without acceleration of void growth can be seen in figure 2.14 (a). Also, figure 2.14 (b) shows the relation between  $f$  and  $f^*$  which are used in equation 2.35.

Figure 2.14 : (a) Evolution of void volume versus crack mouth opening displacement (b) relation



Ruggieri et al. (1996)

According to the Thomasons's plastic limit load [94], coalescence occurs due to localized deformation and the plastic limit load (microscopic internal necking) of material between voids. By growth and nucleation of voids, and developing of necking of material between voids, finally bifurcation occurs [103]. Therefore, both localized deformation and homogenous

deformation need to be considered during coalescence process. The plastic limit load criterion is as follows:

$$\begin{cases} \frac{\sigma_1}{\sigma_f} < \left[ \alpha_{coal} \left( \frac{1}{r_{pll}} - 1 \right)^2 + \frac{\beta_{coal}}{\sqrt{r_{pll}}} \right] (1 - \pi r_{pll}^2) & \text{no coalescence} \\ \frac{\sigma_1}{\sigma_f} = \left[ \alpha_{coal} \left( \frac{1}{r_{pll}} - 1 \right)^2 + \frac{\beta_{coal}}{\sqrt{r_{pll}}} \right] (1 - \pi r_{pll}^2) & \text{coalescence} \end{cases} \quad (2.41a)$$

$$r_{pll} = \frac{2^8 \sqrt{\left(\frac{3f}{4\pi}\right) e^{\varepsilon_1 + \varepsilon_2 + \varepsilon_3}}}{\sqrt{e^{\varepsilon_2 + \varepsilon_3}}} \quad (2.41b)$$

Where

$\sigma_1$  is the maximum principle stress;

$r_{pll}$  is the void space ratio;

$\varepsilon_1$  is the maximum principle strain,  $\varepsilon_2$  and  $\varepsilon_3$  are the other two principle strains;

$\alpha_{coal} = 0.1$  and  $\alpha_{coal}(n_{R-O}) = 0.12 + 0.168n_{R-O}$  for non-hardening and hardening materials; and  $\beta_{coal} = 0.12$  for both;

$n_{R-O}$  is the hardening exponent in Ramberg-Osgood fit;

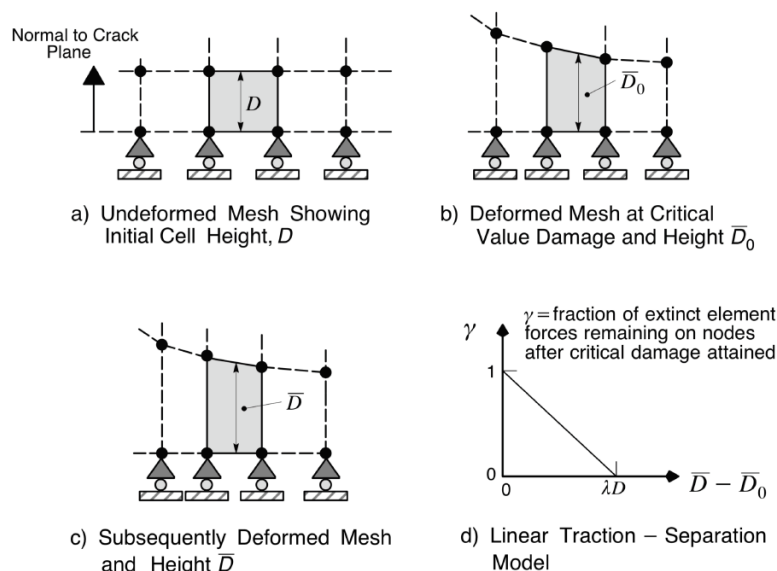
Pardoen et al. [104] improved  $\alpha_{coal}$  and  $\beta_{coal}$  where  $\alpha_{coal}(n_{R-O}) = 0.1 + 0.217n_{R-O} + 4.83n_{R-O}^2$  ( $0 \leq n_{R-O} \leq 0.3$ ) and  $\beta_{coal} = 0.124$ .

In linear traction-separation model [95, 102], when  $f$  reaches  $f_F$ , element deletion occurs by reducing the internal forces to zero in a linear fashion (see figure 2.15(d)). Note that in this model there is no critical void volume fraction ( $f_c$ ). According to figure 2.15, the element deletion process is such that the height of undeformed element is known first (which is equal to  $D$  in figure 2.15(a)). In the next step, when this element reaches void volume failure ( $f_F$ ), the average deformed height normal to the crack plane is denoted  $\bar{D}_0$ , as indicated in figure 2.15(b). During the subsequent load steps, the average deformed height of newly deleted element is equal to  $\bar{D}$  where  $\bar{D} > \bar{D}_0$ , as indicated in figure 2.15(c). At any load step after element reaching  $f_F$ , the remaining fraction ( $\gamma$ ) of internal forces applied to the element nodes tends to zero following a linear traction-separation according to following equation as shown in figure 2.15(d) [105]. This model is often used in the literature [106-109].

$$\gamma = 1 - \frac{\bar{D} - \bar{D}_0}{\lambda D} \quad (2.42)$$

Where  $\lambda$  is the release factor which is equal to 0.1~0.2

Figure 2.15 : Traction-separation scheme for release of nodal forces for newly deleted elements



Zhang et al. (1999)

The yield function of Rousselier model [86, 87], which is developed based on thermodynamical concept of generalized standard media, is as following:

$$\Phi = \frac{\sigma_{eq}}{\rho} - R(p) + B(\beta)D \exp\left(\frac{\sigma_m}{\sigma_1}\right) \quad (2.43)$$

Where  $\rho$  is relative density,  $R(p)$  is the material hardening parameter,  $\beta$  is the damage variable,  $D$  and  $\sigma_1$  are constants.  $B(\beta)$  is a function that represents material softening due to damage. According to following equation it is essential to know the initial void volume fraction and  $\beta$  to calculate  $B(\beta)$ .

$$B(\beta) = \frac{\sigma_1 f_0 \exp(\beta)}{1 - f_0 + f_0 \exp(\beta)} = \sigma_1 f \quad (2.44)$$

Where  $f_0$  and  $f$  are initial and actual void volume fraction.

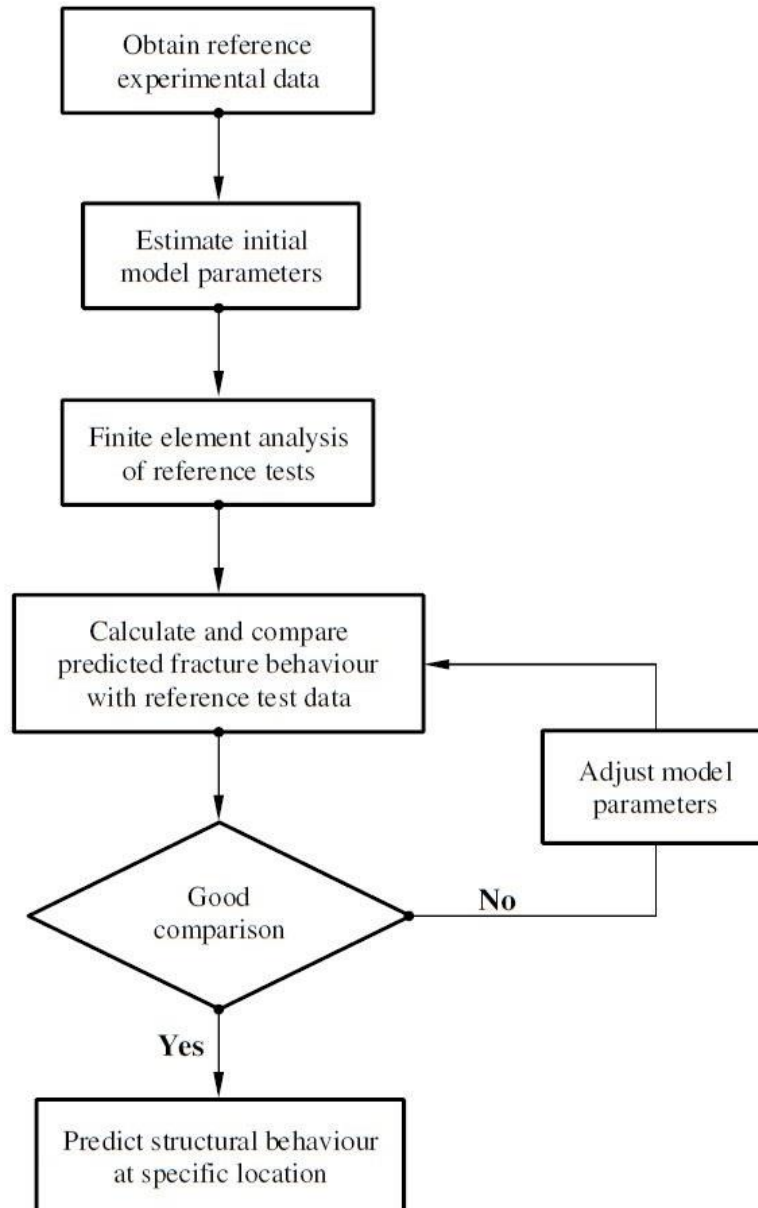
According to equation 2.37, it can be inferred that in this model, the behavior of material is based on a competition between material hardening ( $R(p)$ ) and damage ( $B(\beta)D \exp\left(\frac{\sigma_m}{\sigma_1}\right)$ ), thereby there is no need to introduce a critical damage variable. Moreover, this model has less parameters compared to Gurson's model.

### 2-3-2 Assessment of Cracked Components Using Gurson and Rousselier Models

As mentioned earlier, in order to assess the integrity of a cracked body using Gurson or Rousselier model, it is crucial to calibrate the model parameters for material of interest.

Calibration process is based on comparison of FE data and experimental data. After calibrating the model, the calibrated model can be used to investigate the main structure behavior. The whole process of using Gurson or Rousselier model is shown in the following figure.

Figure2.16 : The process of using Gurson or Rousselier model to assess cracked components



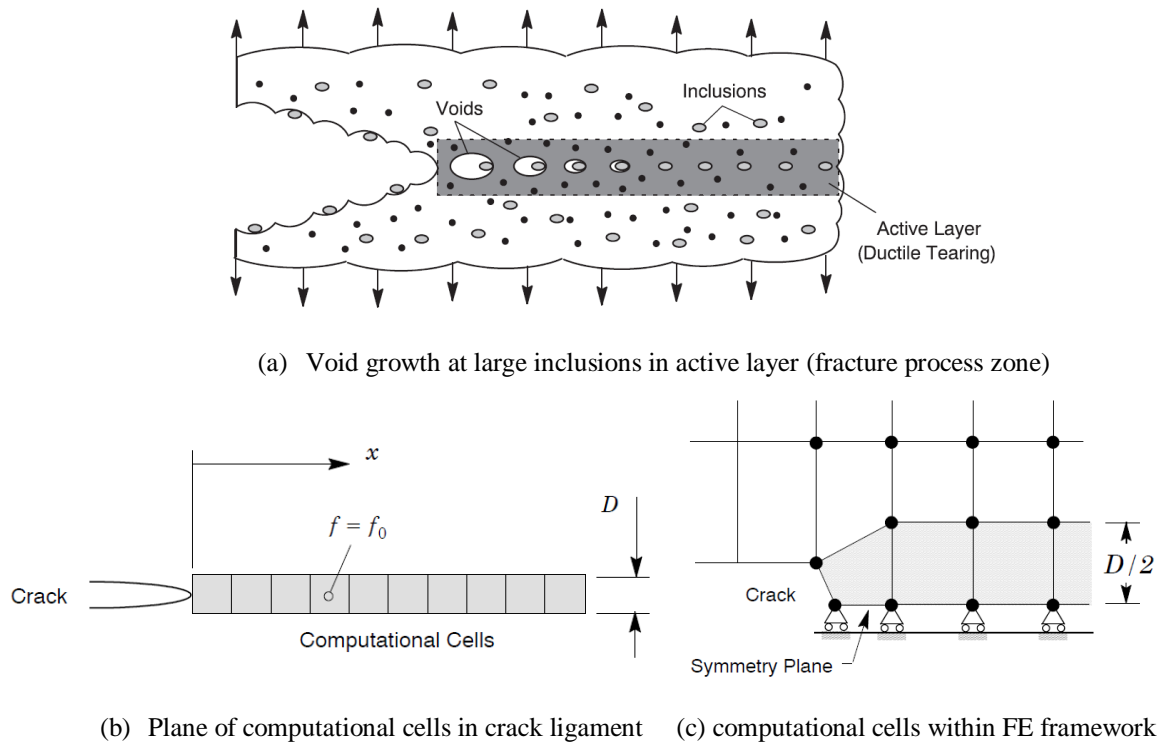
Taktak et al. (2009)

### 2-3-3 Computational cell methodology

In 1995, The computational cell methodology (CCM) was proposed by Xia and Shih [111, 112] in 2D configuration. Later on, 3D CCM was extended by Ruggieri et al. [95] and Gao et al. [90]. Using this method, a row or rows of computational cell elements are modeled at crack

ligament plane, which obey GTN plasticity model, and the rest of the specimen is modeled by conventional mises elements following  $J_2$  flow theory of plasticity (see Figure 2.17). The following figure shows modeling of ductile crack growth using CCM. The dimension of computational cells ( $D$ ) represents the mean space between large inclusions and also it is an indication of the fracture process zone area where damage occurs. The computational cells contain initial void volume fraction ( $f_0$ ) which is a metallurgical feature of the material. By applying load and growth of voids, when failure void volume fraction ( $f_F$ ) reaches, computational cell elements lost their stress-carrying capacity which is a representation of crack growth. In this regard, Ruggieri et al. [95] utilized element extinction when failure void volume fraction is reached to model crack growth. The limitation of this model is that the crack growth path cannot deviate from pre-defined crack plane (plane of computational cells). However, this methodology is widely used in the literature [106-109] which indicates the applicability of methodology in many cases.

Figure2.17 : Modeling of ductile crack growth using computational cells



## 2.4 The key points of literature

The recent developments of fracture toughness testing using SE(T) configurations [25, 26] in connection with the introduction of technical guidelines [13, 30, 59] and, more recently, specific test standards [32] provided a major impetus to conduct further research efforts aimed



at assessing the correlation of fracture conditions between this specimen geometry and cracked pipelines. Nourpanah and Taheri [113] considered 3D finite element models for circumferentially surface cracked pipes and clamped SE(T) specimens made of a homogeneous material representative of typical pipeline grade steels and having crack-like flaws with the same crack depth to show strong similarities in their fracture response, as characterized by CTOD- $\Delta a$  curves. More recently, Sarzosa and Ruggieri [114] also conducted extensive nonlinear 3D finite element analyses to investigate the effects of crack front constraint in clamped SE(T) geometries and circumferentially surface cracked pipes subjected to bending load. They showed that clamped SE(T) specimens having crack sizes in the range  $0.2 \leq a/W \leq 0.4$  provide fracture resistance curves in good agreement with the corresponding fracture behavior of circumferentially cracked pipes. Also a number of previous works [15, 16, 113, 115-119] have addressed effects of constraint on ductile crack growth in SE(T) fracture specimens and cracked pipelines to establish a more effective correlation of fracture behavior for these crack configurations. CTOD resistance curves derived from multiple methods were experimentally investigated for low and high strain hardening material to show the sensitivity of the CTOD values on the deriving method, such J-CTOD relationships and DCG [120]. In general, most of these studies have considered configurations involving only homogeneous materials in which both the fracture specimen and the cracked pipe have the same mechanical properties and, presumably, very similar levels of crack-tip constraint. While such conclusions are of obvious importance as they embody a large part of recent developments in fracture assessment methodologies for offshore pipelines incorporating *R*-curves measured from testing SE(T) fracture specimens, they may not necessarily hold when an FFS analysis is carried out to assess the severity of crack-like flaws in welded components with weld metal strength mismatch. Here, mismatch in the flow properties between the weld metal and the base plate material alters the plastic deformation pattern of crack-like flaws that often occur in the weld metal thereby affecting the coupling relationship between remote loading and crack-tip fields (as characterized by *J* or the crack tip opening displacement - CTOD). In particular, these features have important implications on structural integrity assessments of undermatched welds as, for a given remote loading, crack-tip driving forces are higher when compared with the corresponding quantities evaluated for homogeneous materials. Because of the increased use of higher strength pipeline steels, unintended undermatching between the weld metal and baseplate material may likely occur thereby adding potential difficulties in integrity assessments of field girth welds having circumferential flaws. This picture is further

complicated in the case of a clad pipe girth weld made of corrosion resistant alloys (CRAs) since the potential effects of the clad layer coupled with the rather strong dissimilar character between the weld metal and the baseplate material on the ductile tearing response may affect the fracture response correlation between the fracture specimen and the circumferentially surface cracked pipe.

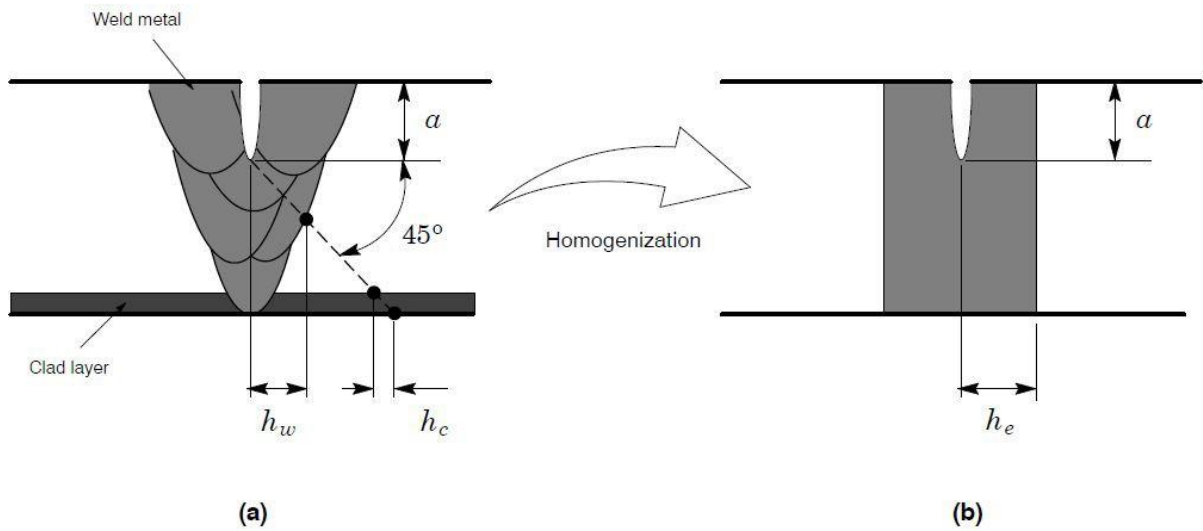
Adoption of an appropriate procedure for incorporating the combined effects of weld strength mismatch and weld groove geometry on the fracture behavior of welded structural components represents a key step in the present study. Here, we follow the homogenization approach to mismatched welds introduced by Souza et al. [121], building upon previous work by Hertelé et al. [122], to describe ductile crack extension in the tested weld centerline notched SE(T) specimen and the girth weld of a steel pipe internally clad with a nickel-based CRA alloy. The problem addressed consists of modeling a weld centerline notched joint of a clad pipe with the additional clad layer material as an equivalent square groove weld. This weld configuration is easier to treat and, further, allows the incorporation of the effect of the clad layer directly into the square groove geometry.

Figure 2.18 illustrates the essential features of the homogenization procedure to obtain an equivalent square groove weld for the girth weld of a clad pipe in which the weld metal and the clad material are made of the same CRA alloy. Following Souza et al. [121], consider an idealized 45° straight slip-line starting at the crack tip and intercepting the weld fusion line and the clad layer as depicted in Figure 2.18 (a). Because of the connection between the slip-line length and the limit load of a cracked component [123-125], the half-width of the equivalent square groove weld,  $h_e$ , shown in Figure 2.18 (b) is simply given by following equation:

$$h_e = h_w + h_c \quad (2.45)$$

where  $h_w$  and  $h_c$  define the half-width of the intercept points at the weld metal and clad layer, as indicated in Figure 2.18 (b). While valid objections might be raised to the relevance of assuming an idealized slip-line angle trajectory associated with perfect plasticity in a dissimilar weld, this simplified approach facilitates the representation of an otherwise complex configuration while, at the same time, allowing a direct comparison of the fracture behavior for girth welds with somewhat different geometries.

Figure 2.18: (a) Typical configuration for a dissimilar weld joint incorporating a layer of clad material. (b) Equivalent weld joint having a square groove geometry derived from the homogenization approach, in which  $h_e = h_w + h_c$ .



This work describes an investigation on the relationships between ductile crack extension in homogeneous and Ni-based clad pipe girth welds with circumferential surface cracks and SE(T) specimens under fixed grip conditions. A primary objective is to gain further insight and understanding of the effects of constraint on ductile tearing behavior in piping components with dissimilar girth welds and how well crack growth resistance curves measured using single edge notched tension fracture specimens correlate with ductile fracture behavior in circumferentially surface cracked pipes. The accurate prediction of ductile crack extension plays a key role in the assessment of critical flaw sizes for this class of structural component which, in turn, ensures safe operating limits on a fitness-for-service basis and provides appropriate inspection intervals and repair decisions.

## CHAPTER 3

### EXPERIMENTAL STUDIES

### 3-1 Introduction

This section describes key details of experimental fracture tests conducted on weld centerline notched SE(T) specimens extracted from girth welds made of different pipe steel grades. These tests (which are not part of this work) were conducted as part of a collaborative research program between the University of Sao Paulo (USP) and Petrobras, testing of these specimens focused on the evaluation of crack growth resistance data for pipe girth welds with different levels of weld strength mismatch, including a dissimilar welded specimen extracted from a clad line pipe. The experimental program covered: 1) an API 5L X80 [126] high strength, pipeline steel girth weld; 2) a girth weld of a typical C-Mn pipe internally clad with a nickel–chromium corrosion resistant alloy (CRA) made of ASTM UNS N06625 Alloy 625 [1, 2]; and 3) a girth weld made of a typical ASTM A106 Gr C [127] carbon steel pipe. The experimental results described here are used to develop improved  $J$ -CTOD relationships for the tested materials and, at the same time, to characterize the CTOD for extending cracks based on detailed analyses of stable crack growth for V-grooved weld models.

### 3-2 X80 Pipe Girth Weld

Mathias et al. [10] performed unloading compliance (UC) tests at room temperature of clamped SE(T) fracture specimens for a girth weld made of an API 5L X80 grade pipeline steel [107]. The tested weld joint was made from a 20-inch (508 mm) pipe with thickness,  $t = 19$  mm, using the FCAW process in the 1G (flat) position with a single V-groove configuration in which the root pass was made by GMAW welding. The weld centerline notched specimen illustrated in figure 3.1(a) has fixed overall geometry and crack length to width ratio defined by  $a/W = 0.4$  and  $H/W = 10$  with thickness  $B = 14.8$  mm and width  $W = 14.8$  mm. Here,  $a$  is the crack depth,  $W$  is the specimen width and  $H$  is the specimen length (“daylight”) between grips. Figure 3.1 (b) shows the weld groove configuration in which a single bevel design was used in the preparation of the test girth weld. Mechanical tensile tests conducted at room temperature (20°C) using subsize test specimens (6.5 mm gage diameter) provide the engineering stress–strain response for both the baseplate (BM) and weld metal (WM) displayed in figure 3.2 (a). Table 3.1 shows the average tensile properties for the tested girth weld in which the measured yield stress values reveal that the weldment overmatches the baseplate material by 18% at room temperature. The table also includes the strain hardening exponents estimated on the basis of API 579 [128] corresponding to the Ramberg–Osgood model [11, 129] to describe the stress–strain behavior for these materials.

The  $J$ -resistance evaluation procedure followed the test method for clamped SE(T) specimens developed at USP [130] and summarized in recent review article [25]. The methodology builds upon an incremental procedure to evaluate  $J$  incorporating a crack growth correction of the measured load–displacement data to obtain accurate estimates of  $J$ -values with increased crack extension (see also Cravero and Ruggieri [62]). Records of load vs. crack mouth opening displacements (CMOD) were obtained using a clip gage mounted on knife edges attached to the specimen surface. The fracture specimens were first fatigue precracked in bending and then subsequently side-grooved to a net thickness of ~85% of the overall thickness (7.5% side-groove on each side) to promote uniform crack growth. Figure 3.3 (a) displays the measured resistance curves for the tested X80 girth weld. These fracture data were obtained using specific expressions for factors  $\eta$  defined by equations 5.1 and 5.2 presented later in Section 5-2. These  $\eta$ -factors are derived from 2D plane-strain numerical analyses of V-grooved weld models for the clamped SE(T) geometry and incorporate the measured tensile properties for the weld metal and baseplate material. Here, we note that, because of the elastic character of the compliance functions to estimate the current crack length, there is no further need for developing a new set of compliance expressions for the present test weld configuration and, thus, the compliance equations provided by Souza and Ruggieri [131] are employed. Details of the numerical analyses performed to determine a specific set of  $\eta$ -factors for the tested weld centerline notched specimens are also provided in Sections 4.2.

Figure 31.: (a) Geometry of tested clamped SE(T) specimens for the API X80 pipeline girth weld with weld centerline notch having  $a/W=0.4$ ,  $H/W=10$  and  $B \times B$  configuration. (b) Single bevel configuration used in the preparation of the test girth weld.

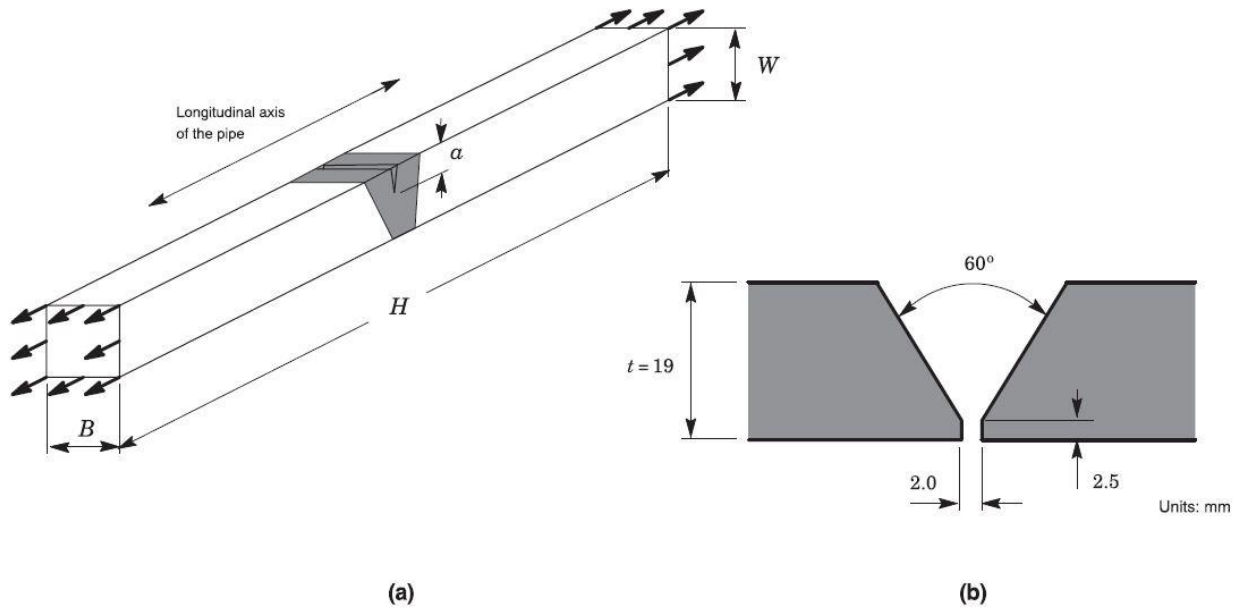
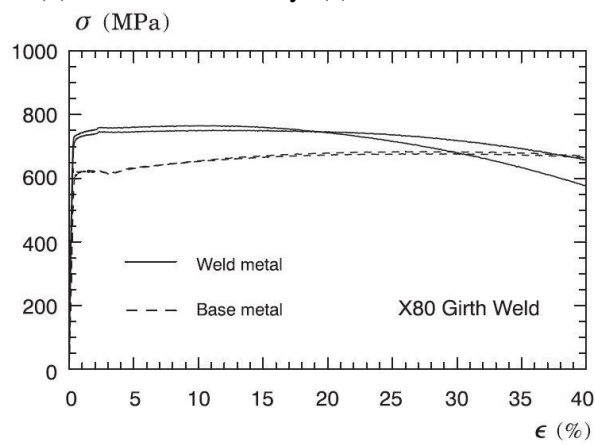
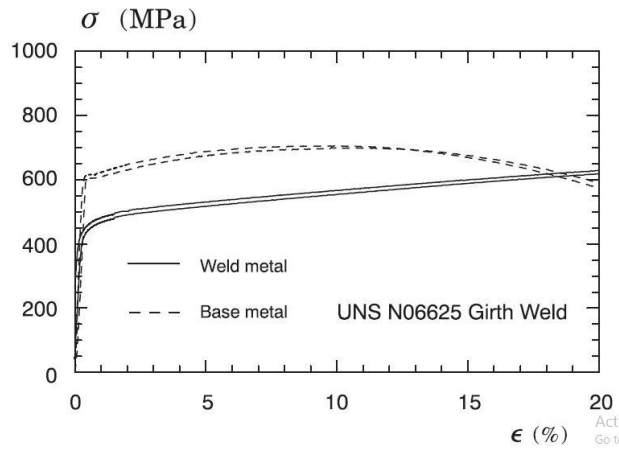


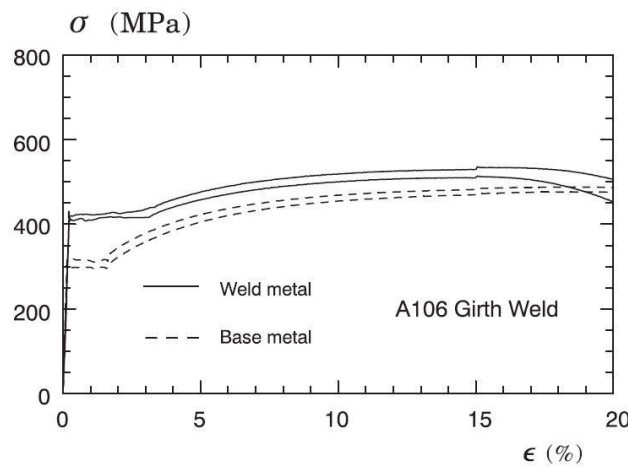
Figure 32.: Engineering stress–strain data for the tested girth welds at room temperature: (a) API X80. (b) UNS N06625 alloy. (c) ASTM A106 Gr C.



(a)



(b)



(c)

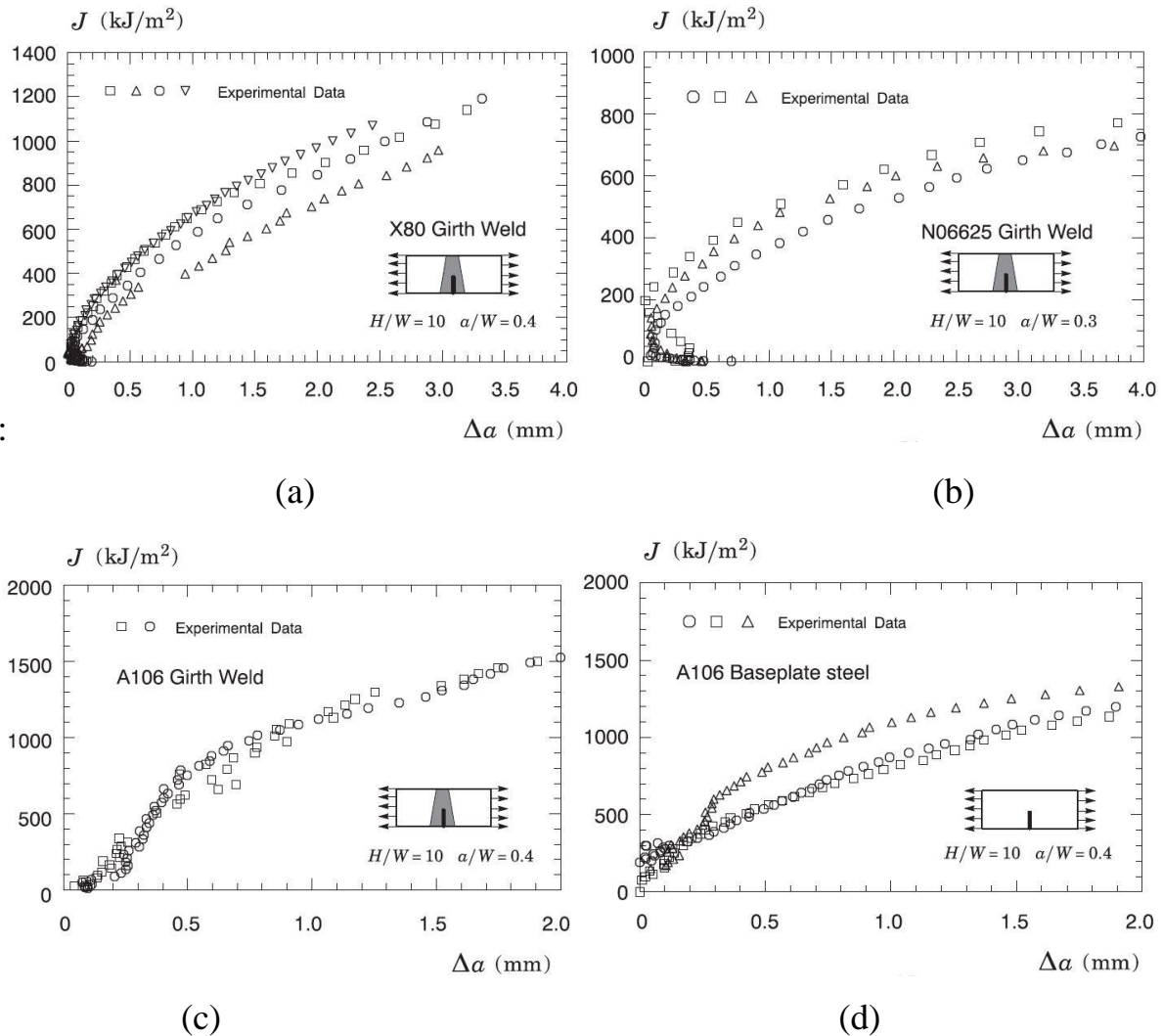
Table 3-1: Tensile properties for the tested girth welds, including the baseplate material, in which  $\sigma_{ys}$  is the yield stress (0.2% offset method),  $\sigma_{uts}$  is the tensile strength and  $n$  is the strain hardening exponent derived from API 579

	<b>Girth weld material</b>	$\sigma_{ys}$ (MPa)	$\sigma_{uts}$ (MPa)	$E$ (GPa)	$\sigma_{uts}/\sigma_{ys}$	$n$
<b>API X80</b>	BM	609	679	209	1.11	20.3
	WM	716	750	215	1.05	35.2
<b>UNS N06625</b>	BM	620	700	200	1.13	18.9
	WM	462	627	158	1.36	9.7
<b>ASTM A106</b>	BM	308	482	215	1.66	7.1
	WM	415	524	185	1.26	11.8

API RP 579 (2016)



Figure 33. :  $J$ -resistance curves including crack growth correction for the clamped SE(T) specimens extracted from the tested girth welds: (a) API X80. (b) UNS N06625 alloy. (c) ASTM A106 Gr C girth weld. (d) ASTM A106 Gr C baseplate.



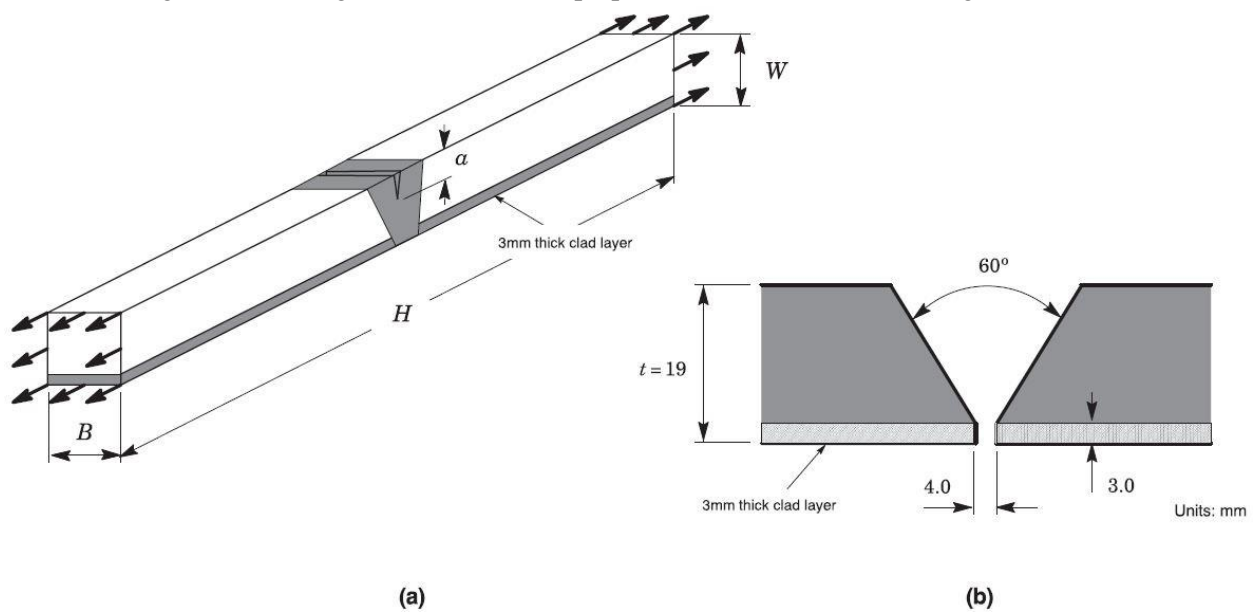
### 3-3 Dissimilar Nickel-Chromium Girth Weld

Sarzosa et al. [132] conducted fracture resistance tests based on the UC method at room temperature on weld centerline notched SE(T) specimens extracted from a girth weld of a typical API 5L X65 pipe internally clad with a nickel–chromium corrosion resistant alloy (CRA) made of UNS N06625 alloy 625 [1, 2], also commercially known as Inconel 625 alloy. The tested weld joint was made from an 8-inch pipe (203 mm outer diameter) having overall thickness,  $t = 19$  mm, which includes a clad layer thickness,  $t_c = 3$  mm. Girth welding of the pipe was performed using 100% CO<sub>2</sub> gas-shielded FCAW process in the 5G (horizontal) position with a single V-groove configuration in which the root pass was made by TIG welding

in the 2G (vertical) position. The fracture specimen shown in figure 3.4 (a) has  $a/W = 0.3$  and  $H/W = 10$  with thickness  $B = 16$  mm, width  $W = 16$  mm and  $H = 160$  mm with 7.5% side-groove on each side. Figure 3.4 (b) depicts the single bevel configuration employed in the preparation of the dissimilar girth weld. A nickel–chromium filler metal matching the UNS N06625 Alloy 625 [1, 2] was utilized to produce the girth weld and, thus, the clad internal layer and the weld metal have essentially the same mechanical properties. Figure 3.2 (b) shows the engineering stress–strain curves for both materials from which the average tensile properties for the tested girth weld are presented in Table 3.1. Here, the measured tensile properties indicate that the weld material undermatches the baseplate material by  $\approx 25\%$  at room temperature and exhibits a strong linear hardening behavior, which contrasts sharply to the hardening properties of the X65 pipe material.

Experimental evaluation of  $J - \Delta a$  data followed similar test protocol as already previously outlined for the API X80 girth weld with  $\eta$ -factors also given by equation 5.1 and 5.2 given next in Section 5-2. Further, to evaluate the CTOD using the DCG method, Sarzosa et al. [132] equipped an additional fracture specimen with a double clip-gage fixture as required for CMOD measurements at two different points illustrated in figure 3.2 (b) - presentation of the CTOD- $R$  curve obtained by Sarzosa et al. [132] is postponed until Section 5-3-3. figure 3.3 (b) displays the  $J$ -resistance curves for the tested dissimilar nickel–chromium girth weld. Apart from a “crack backup” behavior, generally associated with an increase in specimen stiffness with increased loading [9, 54, 133], in the early part of the  $J - R$  curve for all tested configurations, only relatively small scatter is observed in the fracture resistance data.

Figure 34.: (a) Geometry of weld centerline notched SE(T) specimens for the dissimilar nickel chromium girth made of UNS U06625 Alloy having  $a/W=0.3$ ,  $H/W=10$  and  $B \times B$  configuration. (b) Single bevel configuration used in the preparation of the dissimilar test girth weld.



### 3-4 A106 Pipe Girth Weld

Ferreira et al. [134] have carried out a series of fracture experiments for a girth weld made of a typical ASTM A106 Gr C [127] carbon steel pipe to measure its ductile tearing properties based on the UC method at room temperature. The tested weld joint was made from a 9-inch nominal size with 244 mm outer diameter and wall thickness,  $t = 23$  mm. Girth welding of the pipe was performed using shielded metal arc welding (SMAW) process in the 1G (flat) position with a single V-groove configuration in which the root pass was made by TIG welding in the same 1G (flat) position. The pipe was rotated continuously to maintain this position and, further, to ensure similar levels of heat input along the entire girth weld. The filling electrode with low hydrogen coating (AWS E7018) was chosen to provide a degree of weld strength overmatch higher than the usual levels of overmatch for girth welds of pipelines made of high strength steels, such as grades greater than API X70 and X80. Post weld heat treatment (PWHT) of the tested weld joint was conducted by heating it to  $620^\circ\text{C}$  for 1 h followed by cooling down to  $300^\circ\text{C}$  in a heat treat furnace and then left to cool in air to relieve the residual stresses that were potentially introduced during the girth welding.

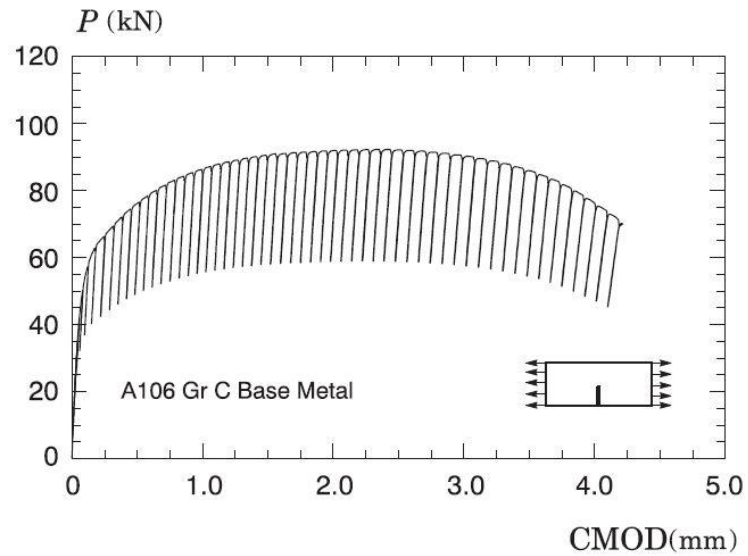
With very minor differences, the UC test procedure followed the same test methodology already outlined for testing the other girth weld materials. Here, the weld centerline notched SE(T) specimens with end-clamped conditions were extracted from the longitudinal direction

of the pipe specimen illustrated in figure 3.1 to measure tearing resistance properties in terms of  $J - \Delta a$  curves using the  $\eta$ -factors described by equations 5.1 and 5.2 provided in Section 5-2. Further, to assess the influence of weld strength mismatch on the fracture resistance properties, UC fracture tests at room temperature were also performed on clamped SE(T) specimens made of the pipe material also extracted from the longitudinal direction of the pipe specimen. The tested geometries have similar configuration to the specimen shown in figure 3.1 (a) with  $a/W = 0.4$ , thickness  $B = 20$  mm, width  $W = 20$  mm and  $H = 200$  mm ( $H/W = 10$ ). The single bevel design used in the preparation of the test girth weld is also similar to the weld groove configuration shown in figure 3.1 (b) but with slightly larger root opening of 6 mm and a smaller root face of 2 mm. Standard tensile tests conducted on conventional tensile specimens provided the mechanical properties at room temperature ( $20^{\circ}\text{C}$ ) for the tested materials. The specimens for the pipe material were extracted from the longitudinal direction of the pipe whereas the specimens for the weld metal were machined from the deposited weld metal with their longitudinal axes parallel to the welding direction. Table 3.1 provides the average tensile properties of the baseplate material and the weld metal. The measured values indicate that the weldment overmatches the baseplate material by 35% at room temperature.

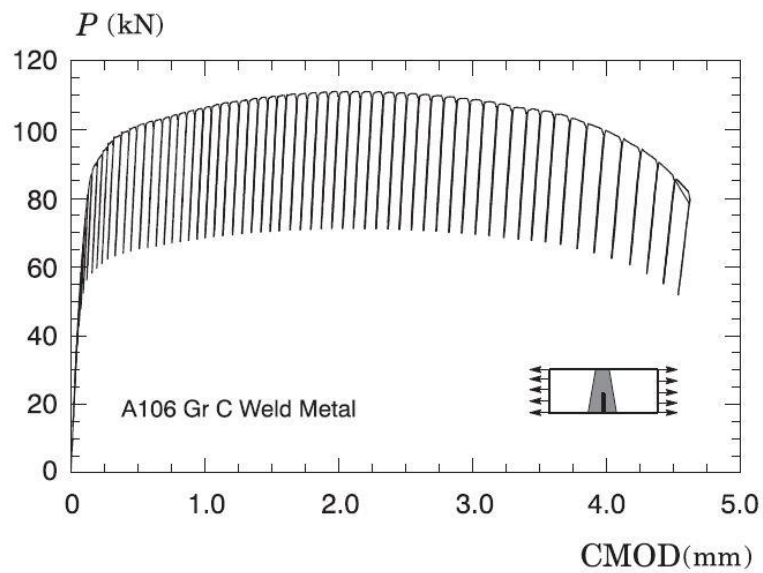
We first draw attention to the load carrying capacity for the homogeneous and weld centerline notched configurations. Figure 3.5 (a-b) shows typical measured load–displacement curves (as described by CMOD) for both material conditions. The effect of weld overmatching on the applied load is evident in this plot. At similar levels of crack mouth opening displacement, the applied load for the welded specimen increases approximately by 20% compared to the load response for the homogeneous geometry. Figure 3.3 (c-d) displays the crack growth resistance curves obtained in the experimental study and illustrate the effects of weld strength mismatch on the fracture resistance properties for the tested materials. Consider first the crack growth results for the welded specimen displayed in figure 3.3 (c), in which, despite some inherent scatter in the measured data, the resistance curves increase sharply in the early part of the resistance curve ( $\Delta a \leq 0.5$  mm) and then show some sign of a constant tearing modulus reaching large  $J$ -values with only moderate amounts of tearing thereby typifying a tough material. Consider next the fracture resistance data for the pipe material shown in figure 3.3 (d). While these curves also exhibit some inherent scatter in the measured data, these resistance curves are somewhat lower than the corresponding  $J$ - $\Delta a$  data for the girth weld material for the entire range of measured ductile tearing. For example, at the amount of crack

growth,  $\Delta a = 2$  mm, the corresponding value of the  $J$ -integral is  $\sim 1500$  kJ/m<sup>2</sup> for the pipe girth weld whereas the corresponding  $J$ -value is  $\sim 1200$  kJ/m<sup>2</sup> for the pipe material.

Figure 35. : Measured load-CMOD curve for the A106 girth weld using clamped SE(T) specimens with  $a/W=0.4$ : (a) Pipe material. (b) Girth weld with 35% weld strength overmatch.



(a)



(b)

## CHAPTER 4

# **FINITE ELEMENT ANALYSIS**

## 4-1 Introduction

This chapter provides details associated with finite element analyses. As mentioned earlier, finite element analysis is an essential step to calibrate GTN model parameters. Furthermore, development of a specific set of  $\eta$ -factors and  $J$ -CTOD relationships more applicable to the tested weld centerline crack configurations require numerically determined solutions generated from V-groove weld models. In this regard, Nonlinear finite element analyses are described for both plane-strain and 3D models of clamped SE(T) fracture specimens with fixed clamps.

## 4-2 Stationary Crack Analysis

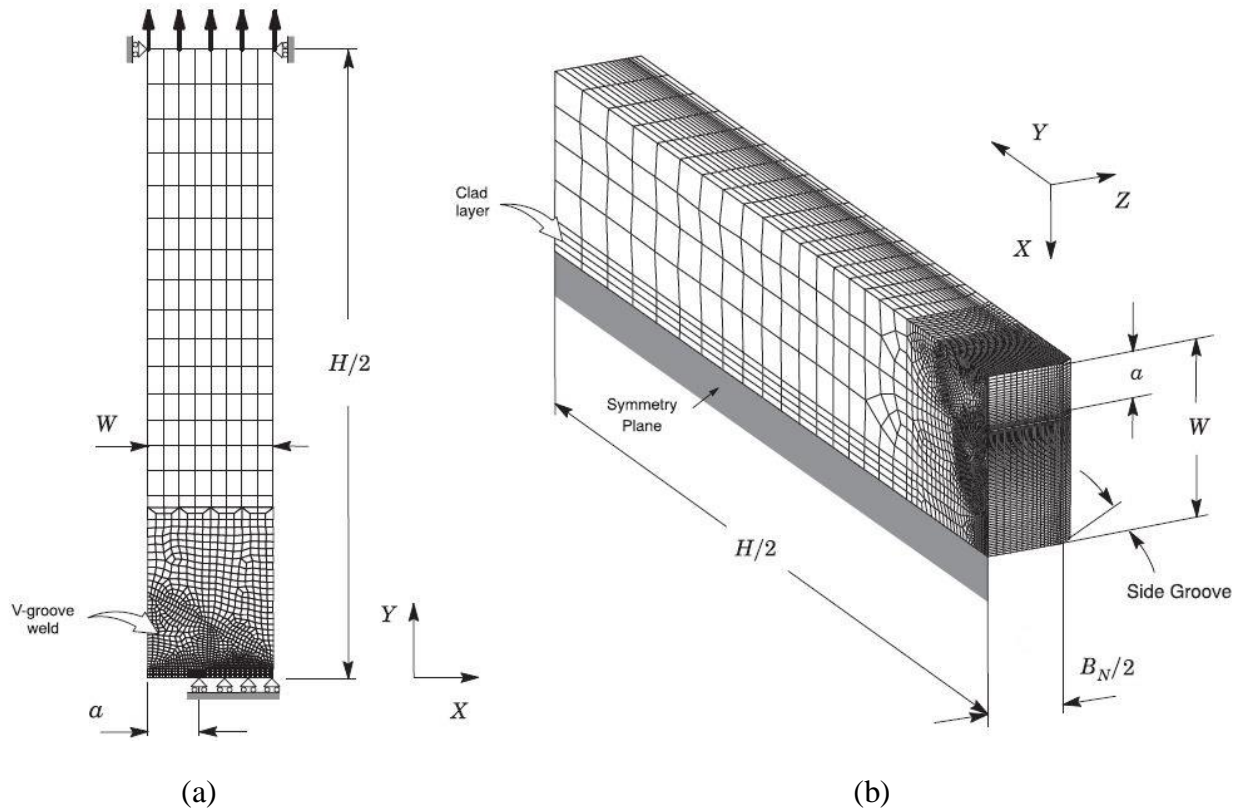
### 4-2-1 Plane-Strain Finite Element Models

Plane-strain models of clamped SE(T) fracture specimens with fixed clamp distance over specimen width ratio,  $H/W = 10$ , and varying crack sizes, as characterized by  $a/W$ -ratios in the range 0.2–0.7 with increments of 0.1 were generated. Here, the specimen width,  $W$ , is defined by each tested geometry as previously described. Moreover, these plane-strain models incorporate the geometry of the weld groove configuration used in the preparation of the test girth weld presented in Section 3. Figure 4.1 (a) shows the 2-D finite element models constructed for the plane-strain analyses of the clamped SE(T) specimen with stationary crack having  $a/W = 0.4$  for the X80 test geometry. This model incorporates the V-groove weld configuration shown in figure 4.1 (b). With minor differences, all other crack models have very similar features. Further, the plane-strain model of the fracture specimen for the UNS N06625 test geometry also includes the 3 mm clad layer as indicated in figure 4.2. A small key-hole at the crack tip having a radius,  $\rho_0$ , of 2.5  $\mu\text{m}$  is employed to enhance resolution of near-tip stresses and strains, as well as computation of  $J$ -values at low deformation levels.

#### 4-2-1-1 Boundary Conditions

Symmetry conditions permit modeling of only one-half of the specimen with appropriate constraints imposed on the symmetry as well as plane-strain constraints ( $w = 0$ ) imposed on each node, as indicated in figure 4.2 . In particular, clamped grip conditions are enforced by imposing zero lateral displacements at the end of the specimens as also indicated in figure 4.2 (a). A typical half-symmetric, 2-D model has one thickness layer of 2000–3000 elements and 4000–6000 nodes depending on the geometry, crack size and groove details. These numerical models are loaded by displacement increments imposed on the loading points to enhance numerical convergence with increased levels of deformation.

Figure 4:1. Typical finite element models for stationary crack analysis of the clamped SE(T) specimen incorporating the V-groove weld configuration: (a) Plane-strain model for the X80 girth weld test geometry with  $a/W=0.4$ . (b) 3-D numerical model for the UNS N06625 girth weld test geometry with  $a/W=0.3$ .



#### 4-2-2 3-D Finite Element Models

3-D numerical analysis of ductile crack growth for the dissimilar nickel–chromium girth weld made of UNS N06625 alloy 625 in which the experimental  $J$ - $\Delta a$  data are also determined from improved  $\eta$ -factors derived from 3-D stationary crack analysis. These 3-D finite element models have  $H/W = 10$  and varying crack sizes, as characterized by  $a/W$ -ratios in the range 0.2–0.7 with increments of 0.1. Figure 4.2 shows the quarter-symmetric, 3-D model for the clamped SE(T) specimen having  $a/W = 0.3$  in accordance with the UNS N06625 test geometry, including the 3 mm clad layer. The finite element mesh has 15 variable thickness layers defined over the half net thickness ( $B_N/2$ ) to accommodate strong  $Z$  variations in the stress distribution and at the same time to resolve the pointwise  $J$ -integral over the crack front. Here, the layer thickness defining the specimen center plane at  $Z = 0$  is  $0.055B_N$  whereas the layer defined near the side-groove ( $Z = B_N/2$ ) is  $0.015B_N$ . The additional 3 outermost layers describing the side-groove region then compose the full bulk of the specimen,  $B/2$ , as indicated in Figure 4.2



(b). The quarter-symmetric, 3-D model for this specimen also incorporates an initially blunted crack tip with radius,  $\rho_0$ , of 2.5  $\mu\text{m}$  and has  $\sim 61,800$  nodes and  $\sim 56,000$  8-node, 3-D elements.

### **4-3 Growing Crack Analysis**

#### **4-3-1 Plane-Strain Finite Element Models**

Nonlinear finite element analyses incorporating crack growth are also described for the plane-strain models of the tested specimens having the geometries described in chapter 3. figure 4.2 (a) shows the finite element model constructed for the 2-D analyses of the SE(T) geometry having  $a/W = 0.3$  employed in the fracture testing of the UNS N06625 girth weld. The numerical model also incorporates the V-groove weld configuration and the 3 mm clad layer shown in figure 4.2 . To simulate ductile crack extension using the GT model, the planar mesh (2-D) for this configuration contains a row of 112 computational cells, each cell with size  $D/2 = 100 \mu\text{m}$ , along the remaining crack ligament ( $W-a$ ) as depicted in the arrangement of figure 4.2. The choice of the cell size,  $D/2$ , follows Ruggieri et al. [95] on the basis of an approximate correlation of spacing between the large inclusions and the crack tip opening displacement (CTOD) at the onset of macroscopic crack growth in conventional fracture specimens for common pressure vessel steels.

Further, to evaluate the CTOD during crack extension based on the DCG procedure, the finite element model is equipped with a rigid, elastic element at the crack mouth as indicated in figure 4.2 (a). This arrangement thus enables the measurements of crack opening displacements (COD) at two different points as required in the DCG method. All other numerical models for growth analyses have very similar features.

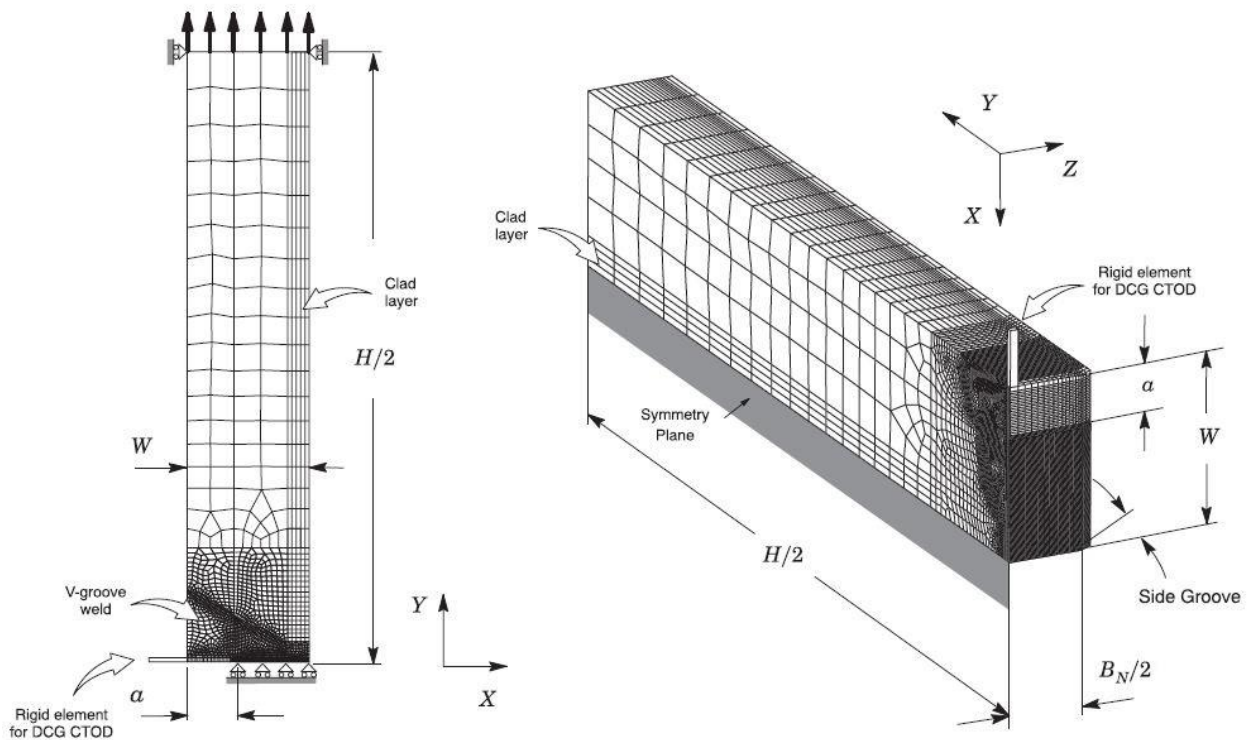
##### ***4-3-1-1 Boundary Conditions***

Symmetry conditions permit modeling of only one-half of the specimen with appropriate constraints imposed on the remaining ligament. This half-symmetric, plane-strain model is similar to the previous numerical model employed in the stationary crack analyses previously described and has one thickness layer of 1778 elements and 3790 nodes with plane-strain constraints ( $w = 0$ ) imposed on each node.

### 4-3-2 3-D Finite Element Models

Experimental observations of low-constraint fracture specimens employed in  $J$ -resistance testing of ductile material often reveal a rather severe crack front tunneling, even in side-grooved configurations, which contrasts sharply to the uniform growth implicitly assumed in the plane-strain analysis considered in the present study. To address this issue, 3-D finite element analyses incorporating ductile crack growth are also performed on the dissimilar UNS N06625 alloy 625 girth weld to examine 3-D effects on the resulting CTOD resistance curve for this test configuration. Figure 4.2 (b) displays the quarter-symmetric 3-D finite element model for the tested clamped SE(T) specimen with  $a/W = 0.3$  and the V-groove weld geometry - the numerical model also incorporates the 3 mm clad layer and a rigid, elastic element at the crack mouth to measure the DCG CTOD as indicated in the figure. The 3-D mesh is thus obtained by simply extruding the 2-D mesh along the  $Z$ -axis; the in-plane ( $X$ - $Y$ ) finite element mesh has therefore identical mesh refinement as the plane-strain model, including a row of 112 computational cells, each cell with size  $D/2 = 100 \mu\text{m}$ , along the remaining crack ligament ( $W - a$ ). This finite element mesh has 15 variable thickness layers defined over the half net thickness ( $B_N/2$ ) and same layer thickness at the specimen center plane and at the side groove region as the numerical model employed in the stationary crack analyses previously described. The mesh arrangement at  $Y = 0$  contains a slab of  $15 \times 112 = 1680$  cell elements to capture the onset of ductile tearing and crack growth along the crack front on the specimen centerplane.

Figure 4.2. Finite element models for the clamped SE(T) specimens with  $a/W=0.3$  employed in the fracture testing of the UNS N06625 girth weld: (a) Half-symmetric plane-strain model. (b) Quarter-symmetric 3-D numerical model.

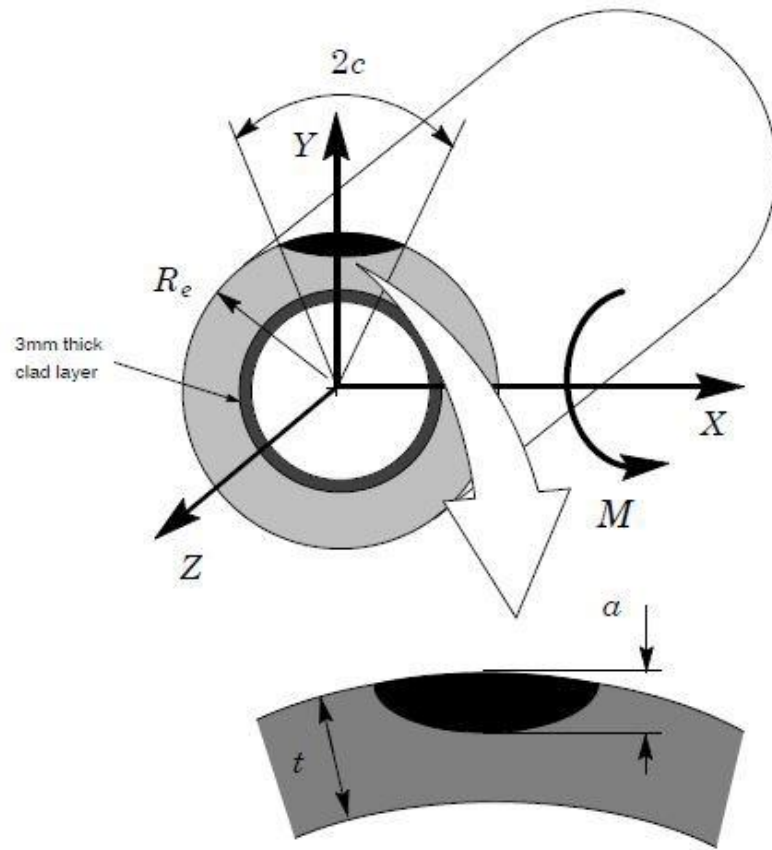


#### 4-3-2-1 Circumferentially Cracked Pipes

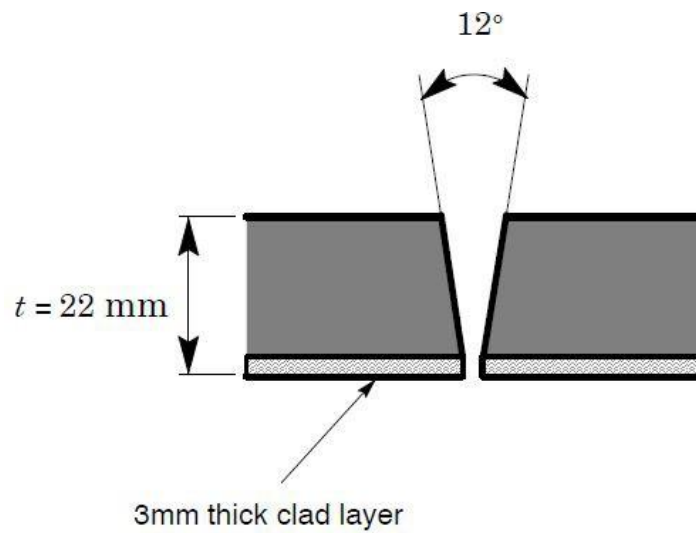
Once the GT parameters are calibrated using de  $R$ -curves for the tested SE(T) specimens (see Section 4.1 next), the analyses proceed by conducting a verification analysis which compares predictions of ductile crack extension in circumferentially cracked pipes under bending and clamped SE(T) fracture specimens. This study focuses on a typical pipe configuration employed in the submarine infrastructure having external diameter,  $De = 273\text{mm}$  (10" NPS) with an overall thickness of 22mm, including a 3mm clad layer, as indicated in Figure 4.3 (a). The pipe girth weld is characterized by a V-groove geometry with a narrow groove weld of about  $12^\circ$  illustrated in Figure 4.3(b), which represents current trends in field girth welds of submarine pipelines made by automatic processes [78]. Three relative crack depths are considered in the present work and are given by  $a/t = 0.1, 0.2$  and  $0.3$  with a fixed crack length,  $2c = 100\text{mm}$  - see Figure 4.3(a). Here, the circumferentially flaw size with  $a/t = 0.3$  matches the  $a/W$ -ratio of the weld centerline notched specimen utilized in the fracture resistance testing of the girth weld material, whereas the circumferentially cracked pipe having

an  $a/t$ -ratio of 0.1 encompasses short crack sizes typically considered during in-service flaw evaluations. Moreover, the analyses also consider a equivalent square groove weld as obtained by the homogenization procedure outlined previously in Section 2.3.

Figure 4.4 shows the 3-D quarter-symmetric finite element model for the circumferentially cracked pipe with  $a/t = 0.3$  and having a V-groove weld geometry incorporating the GT cells to describe ductile crack extension. This numerical model has 26,058 elements with pertinent constraint conditions enforced on the symmetry planes. Similarly to the finite element arrangement for the SE(T) specimens, a row of 61 computational cells, each cell also having a size  $D/2 = 100\mu\text{m}$ , on each layer along the remaining crack ligament ( $t-a$ ) is used to describe the onset of a ductile crack along the 19 layers defining the semi-elliptical crack front, in a mesh arrangement of  $19 \times 61 = 1159$  cell elements. To ensure that a constant bending moment with zero shear forces is imposed on the crack plane, the quarter-symmetric finite element model is loaded by a four-point bending scheme as indicated in Figure 4.4. The numerical models for the circumferentially cracked pipe with a square groove weld geometry of width  $he = 7.5\text{mm}$ , in which  $hw = 4.4\text{mm}$  and  $hc = 3.1\text{mm}$ , also have essentially similar features as those for the V-groove models, including the cell arrangement already described. Similarly to the numerical models for the SE(T) specimens, the finite element meshes for both the V-groove and square groove models are equipped with a rigid, elastic element at the crack mouth as indicated in Figure 4.4 to evaluate the CTOD during crack extension based on the DCG procedure.



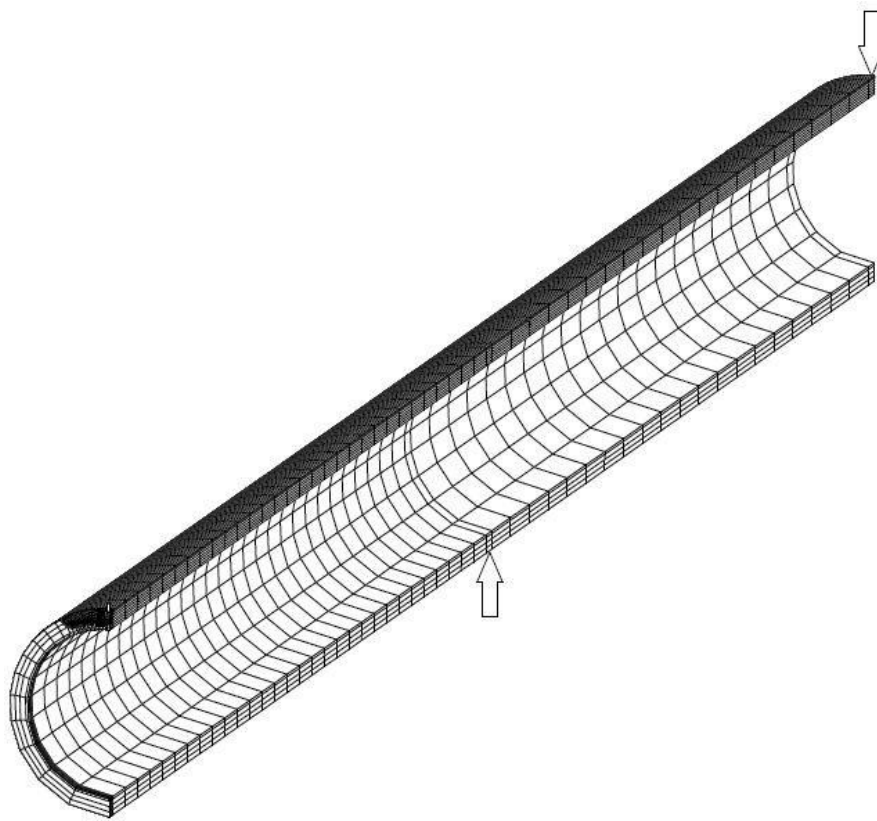
(a)



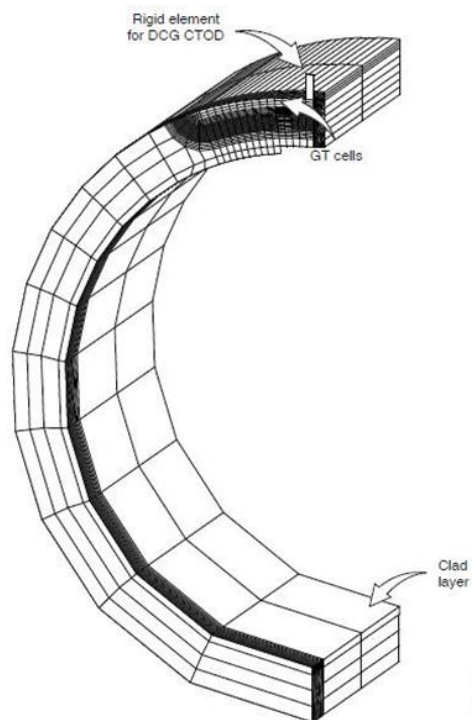
(b)

Figure 4.3: (a) Circumferentially cracked pipe configuration having a dissimilar Ni-Cr weld and an internal CRA clad layer under bending. (b) Narrow groove weld geometry adopted in the numerical analyses.

Figure 44.: 3D quarter-symmetric finite element model for the circumferentially cracked pipe with  $a/t = 0.3$  and having a V-groove weld geometry incorporating the GT cells to describe ductile crack extension



(a)



(b)

#### 4-4 Material Models

The finite element solutions reported here are generated by employing an elastic–plastic material model incorporating conventional Mises plasticity theory in small geometry change (SCG) setting for the stationary crack analyses and large geometry change (LGC) setting for the crack growth analyses. The material model for both the weld metal and baseplate material utilizes a piecewise-linear representation of the true stress-logarithm strain behavior derived from the measured tensile response for each material described in figure 3.2 and table 3.1 with a Poisson’s ratio,  $\nu = 0.3$ .

#### 4-5 Software

The finite element code WARP3D [105] provides the numerical solutions for the extensive simulations reported here including stationary and crack growth analyses implementing the cell model. The research code FRACTUS2D [68] is employed to compute the required  $\eta$ -factors and the  $J$ -CTOD relations derived from stationary and growing analyses for the analyzed fracture specimens incorporating a V-groove weld. Evaluation of the numerical value of CTOD follows the 90° procedure [11] to the deformed crack flanks as illustrated in figure 2.5 (b).

The finite element computations employ a domain integral procedure [135] for numerical evaluation of equation 2.18 to provide pointwise and front average values of  $J$  across the crack front at each loading level. In each case, the  $J$ -values are computed over domains defined outside material having the highly non-proportional histories of the near-tip fields and thus retain a strong domain (path) independence. Moreover, the thickness average values of  $J$  agree very well with estimation schemes based upon  $\eta$ -factors for deformation plasticity [11] so that they provide a convenient parameter to characterize the average intensity of far field loading on the crack front.

## CHAPTER 5

## RESULTS



## 5-1 Introduction

This chapter provides the results of this study, including  $\eta_{J-CMOD}$  and  $\eta_{J-LLD}$  derived from finite element analysis of plane-strain and 3D models incorporating the weld groove configuration and the material properties described in chapter 4. These derived  $\eta$ -factors (see figure 5.1) for the weld centerline notched SE(T) specimens with varying  $a/W$ -ratios for all girth welds under consideration were used to obtain crack growth resistance curve in chapter 3. In these plots, the lines represent fitting curves to the computed plane-strain  $\eta$ -values. For comparison, the figures also include the  $\eta$ -factor solutions for homogeneous clamped SE(T) geometries derived from previous work of Mathias et al. [10].

## 5-2 $\eta$ -factors and J-CTOD relationships for stationary crack analysis of V-groove welds

Consider first the  $\eta_{J-CMOD}$  results shown in figure 5.1 (a). Apart from small differences, the  $\eta$ -values for the girth welds are in close agreement with the results of Mathias et al. [10] in the range  $0.2 \leq a/W \leq 0.4-0.5$ . In contrast, the  $\eta$ -values depend somewhat more sensitively on the girth weld material, particularly for the UNS N06625 girth weld with  $a/W \geq 0.5$ . Here, these larger differences in the  $\eta$ -values most likely arise from the much stronger influence of the V-shaped weld groove in connection with the level of mismatch in material properties on the load-CMOD curve and, thus, on the plastic area upon which  $\eta_J$  is defined. As the crack size increases towards the weld root region, the local width of the weld metal effectively affecting the crack tip is narrower (refer to figure 3.1) so that the effects of strength mismatch on the evolution of load with CMOD are diminished. Overall, however, these differences are not large enough to significantly influence the determination of  $J$  based on the plastic area under the load-CMOD curve.

Consider next the  $\eta_{J-LLD}$  results shown in figure 5.1 (b). A different picture emerges here as the  $\eta$ -values for the girth welds display larger differences relative to the results of Mathias et al. [10]. Remarkably, the  $\eta$ -values for the A106 girth weld are substantially lower compared to the results for homogeneous material over the entire  $a/W$ -ratio considered. While we have not explored in details such behavior, it can be understood by the following argument. This girth weld has a very high degree of strength mismatch between the weld metal and the baseplate material of  $\approx 35\%$ , thus shielding the weld region from the (remote) applied displacements at the clamped ends. While the CMOD is less affected by the degree of mismatch

in material properties, it becomes clear that the LLD is much more sensitive to the strength of the weld metal relative to the baseplate. Similar results were also found in recent work of Paredes and Ruggieri [23] who investigated the effects of weld strength mismatch on  $\eta$ -factors for weld centerline notched SE(T) configurations having square groove welds. However, since  $\eta_{J-LLD}$  enters into the fracture resistance evaluation procedure only to correct  $J$  for crack growth (refer to Section 2-2-2-3-1), it is expected to give only a relatively moderate effect on the  $J$ -resistance curves.

The  $J$ -CTOD relationships for the stationary crack analysis of V-groove weld models are also of interest. Figure 5.2 shows the variation of  $m = J/(\delta\sigma_f)$  with varying  $a/W$ -ratios, as described by open symbols, for the V-groove weld models of the tested girth welds. For every material considered in figure 5.2, parameter  $m$  exhibits a weak dependence on the  $a/W$ -ratio. As expected, though, the  $m$ -value displays a more noticeable sensitivity on material properties, ranging from  $\sim 1.2$  for the UNS N06625 girth weld to 1.4–1.5 for the X80 girth weld. For reference, this plot also includes the dependence of  $m$  on crack size over the range  $0.2 \leq a/W \leq 0.7$  obtained from equation 14 appearing in previous work of Sarzosa et al. [71], hereafter referred to as SSR, with the strain hardening exponent for the weld metal material given in table 3.1. Relative to the results of SSR, which are applicable to stationary crack analyses of plane-sided specimens made of homogeneous material, the present set of  $m$ -values derived from the V-groove weld models is in generally good agreement.

Now, to provide a simpler manipulation of the previous results, a functional dependence of factors  $\eta_J$  and parameter  $m$  with  $a/W$ -ratio is obtained in the form:

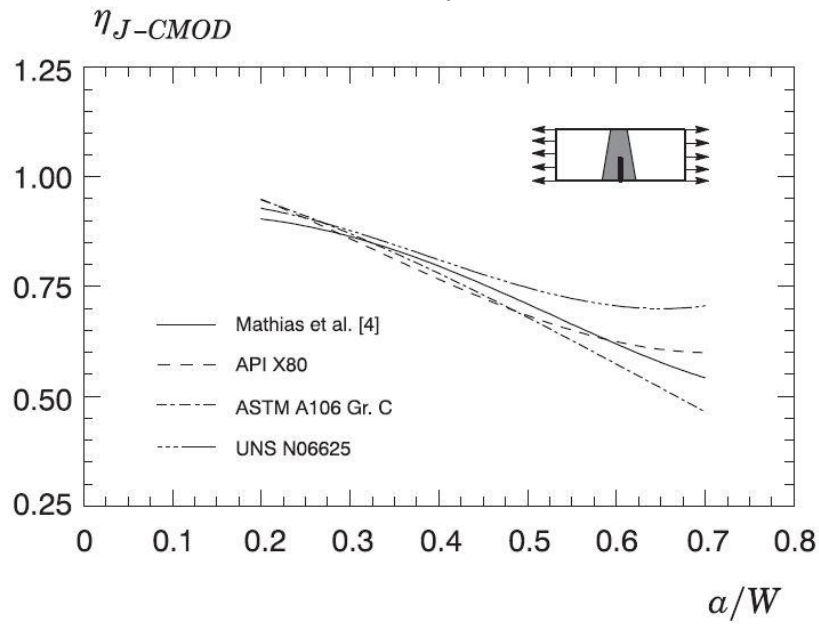
$$\eta_{J-CMOD} = b_0 + b_1 \left(\frac{a}{w}\right) + b_2 \left(\frac{a}{w}\right)^2 + b_3 \left(\frac{a}{w}\right)^3 \quad (5.1)$$

$$\eta_{J-LLD} = c_0 + c_1 \left(\frac{a}{w}\right) + c_2 \left(\frac{a}{w}\right)^2 + c_3 \left(\frac{a}{w}\right)^3 + c_4 \left(\frac{a}{w}\right)^4 + c_5 \left(\frac{a}{w}\right)^5 \quad (5.2)$$

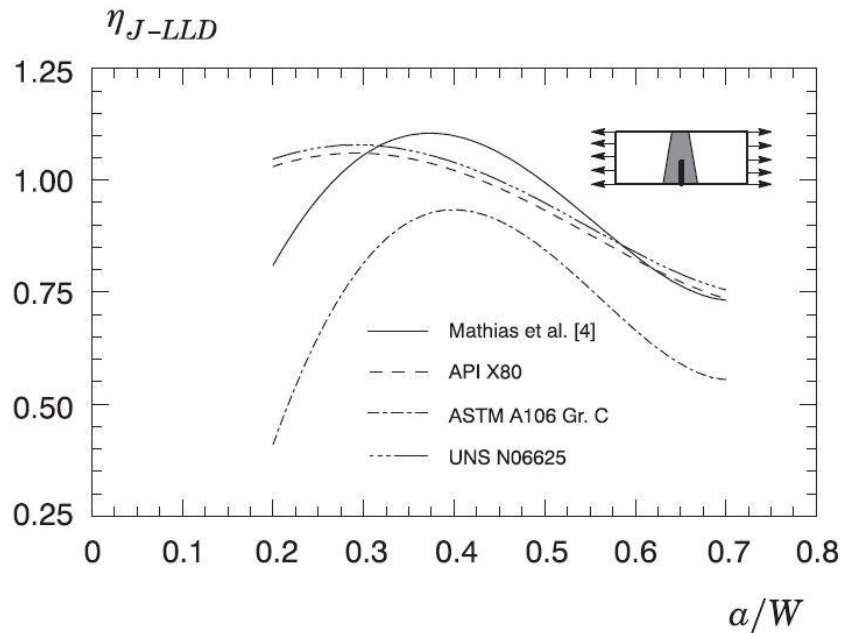
$$m = d_0 + d_1 \left(\frac{a}{w}\right) + d_2 \left(\frac{a}{w}\right)^2 \quad (5.3)$$

which are applicable in the range of  $0.2 \leq a/W \leq 0.7$  for stationary cracks. Tables 5.1 and 5.2 provide the coefficients of the above polynomial fitting for the tested girth welds considered in the present study.

Figure 51. : Dependence of  $\eta$ -factors on  $a/W$ -ratio derived from plane-strain analysis incorporating the weld groove configuration and material properties for the tested girth welds: (a) Factors  $\eta$  based on CMOD. (b) Factors  $\eta$  based on LLD.

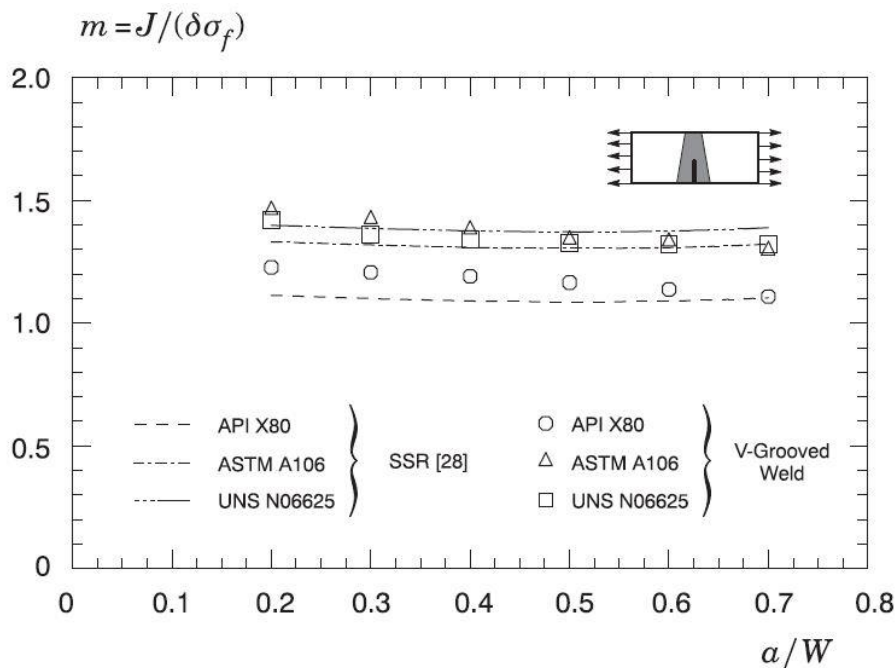


(a)



(b)

Figure 52.: Dependence of J-CTOD relationships, as characterized by parameter  $m$ , on  $a/W$ -ratio derived from plane-strain analysis incorporating the weld groove configuration and material properties for the tested girth welds.



### 5-3 CTOD resistance data for extending cracks

#### 5-3-1 Numerical simulation of crack growth

Numerical simulation of crack growth in plane-strain setting for the SE(T) specimens described here begins with calibration of the cell model parameters for the girth welds employed in this study. Guided by the previous studies of Ruggieri and Dodds [95], Gullerud et al. [102] and Ruggieri and Dotta [108], the analysis follows from matching the computed resistance curves with the measured fracture resistance data. Since the GTN constitutive model depends on a number of parameters, the model calibration can be accomplished in several ways. As already briefly discussed in preceding sections, the simplest approach is to fix the cell size,  $D/2$ , and, further, the strain nucleation parameters  $f_N$  and  $S_N$  at the onset of the analysis and then determine suitable values for the initial volume fraction,  $f_0$ , and the mean value of the plastic strain driving the nucleation of new voids,  $\varepsilon_N$ , that produce the best fit to the measured crack growth data for the tested specimens. However, while the calibrated values for  $f_0$  and  $\varepsilon_N$  are somewhat coupled (a change in  $\varepsilon_N$  also leads to a change in  $f_0$  that produces the best fit to the measured fracture resistance data), the  $f_0$ -value that yields the resistance curve in agreement with the experimental results is presumably weakly affected by small changes in  $\varepsilon_N$  (recall that  $\varepsilon_N$  can take a value several hundred times greater than the yield strain value for the material).

Figure 5.3 shows the predicted  $J$ - $\Delta a$  curves for every case under consideration using the cell size  $D/2 = 100 \mu\text{m}$ ,  $f_N = 0.5$  and  $S_N = 0.05$  and slightly varying  $\varepsilon_N$ -values. For each tested girth weld and the A106 baseplate material, predicted  $R$ -curves are shown for three values of the initial volume fraction as indicated in the plots. These analyses are rather conclusive as the initial volume fraction,  $f_0$ , plays a central role in capturing the predicted evolution of  $J$  with  $\Delta a$  for every case. Consider, for example, the results for the X80 girth weld displayed in figure 5.3 (a). For  $f_0 = 0.003$ , the predicted  $R$ -curve agrees well with the average measured values for almost the entire range of growth despite the inherent scatter in the experimental data. However, since the primary interest here lies in the description of fracture resistance as a means to determine the CTOD for a growing crack, some differences between the predicted and the measured crack growth resistance curve are not of particular concern. In contrast, the use of  $f_0 = 0.01$  produces a lower resistance curve relative to the measured data. Essentially similar behavior is observed for other tested materials, including the A106 baseplate steel pipe. Table 5 summarizes the calibrated GTN parameters and includes factors  $q_1, q_2$  derived from the work of Faleskog and Shih [89].

### 5-3-2 CTOD-R curves based on plane-strain analyses

The previous 2-D finite element analyses incorporating a phenomenological model for stable crack growth provide a basis for describing ductile fracture response of the tested girth welds in terms of CTOD- $\Delta a$  data. Here, the CTOD fracture resistance curves displayed in figure 5.4 are determined as follows: (1) CTOD-values based on the double clip gage (DCG) procedure, denoted  $\delta_{DCG}$ , displayed in figure 2.11. (2) CTOD-values determined using the  $90^\circ$  intercept procedure based on the CTOD-values evaluated using the  $90^\circ$  intercept procedure based on the extending crack tip and the deformed crack flanks illustrated in figure 2.5 (b),  $\delta_{ECT}$ . (3) CTOD-values converted from corresponding  $J$ -values of the resistance curves described by the solid line in figure 5.4 using the computed  $J$ -CTOD relationships expressed by equation 5.3 with the coefficients  $d_k$  given in table 5.3. Here, the computed curves based on the cell model analysis that give the best fit to the corresponding sets of experimentally measured  $J$ - $R$  curves are considered as average resistance curves for each case considered. Moreover, the CTOD-resistance curves in which the CTOD-value is converted from the  $J$ -CTOD relationship for stationary cracks given by equation 14 appearing in SSR [136] are also provided to aid in assessing the relative changes in CTOD- $\Delta a$  data based on the previous definitions for CTOD. Further observe that figure 5.4 (d) refers to the CTOD resistance curves

for the ASTM A106 baseplate material and, thus, only the CTOD- $R$  curve derived from SSR [136] is included in the plot.

The results displayed in figure 5.4 show a dependence of the crack growth resistance curves on the CTOD model adopted. Such dependence also appears to be related to material flow properties and degree of weld strength mismatch. Consider first the fracture resistance results for the X80 and UNS N06625 girth welds shown in figure 5.4 (a-b). Here, the variation of CTOD with  $\Delta a$  using the  $J$ -CTOD relationships derived from the V-groove weld model is essentially unchanged with regard to the corresponding fracture resistance data based on the SSR [136] expression. Remarkably, the CTOD- $R$  curves based on  $\delta_{ECT}$  and  $\delta_{DCG}$  are also fairly indistinguishable from each other. Observe, however, that the latter curves are consistently higher than the corresponding fracture resistance curves based on  $J$ -CTOD relationships. Now direct attention to the CTOD- $\Delta a$  data for the A106 girth weld and the baseplate material shown in figure 5.4 (c-d). The overall trends remain similar except that the variation of  $\delta_{ECT}$  and  $\delta_{DCG}$  with crack growth and the fracture resistance data derived from  $J$ -CTOD relationships differ by a larger amount. Moreover, and perhaps equally importantly, a noteworthy feature of these results is that, in every case considered, the CTOD resistance data based on the double clip gage method to determine  $\delta_{DCG}$ , is again always higher than the CTOD resistance curves based on  $J$ -CTOD relationships.

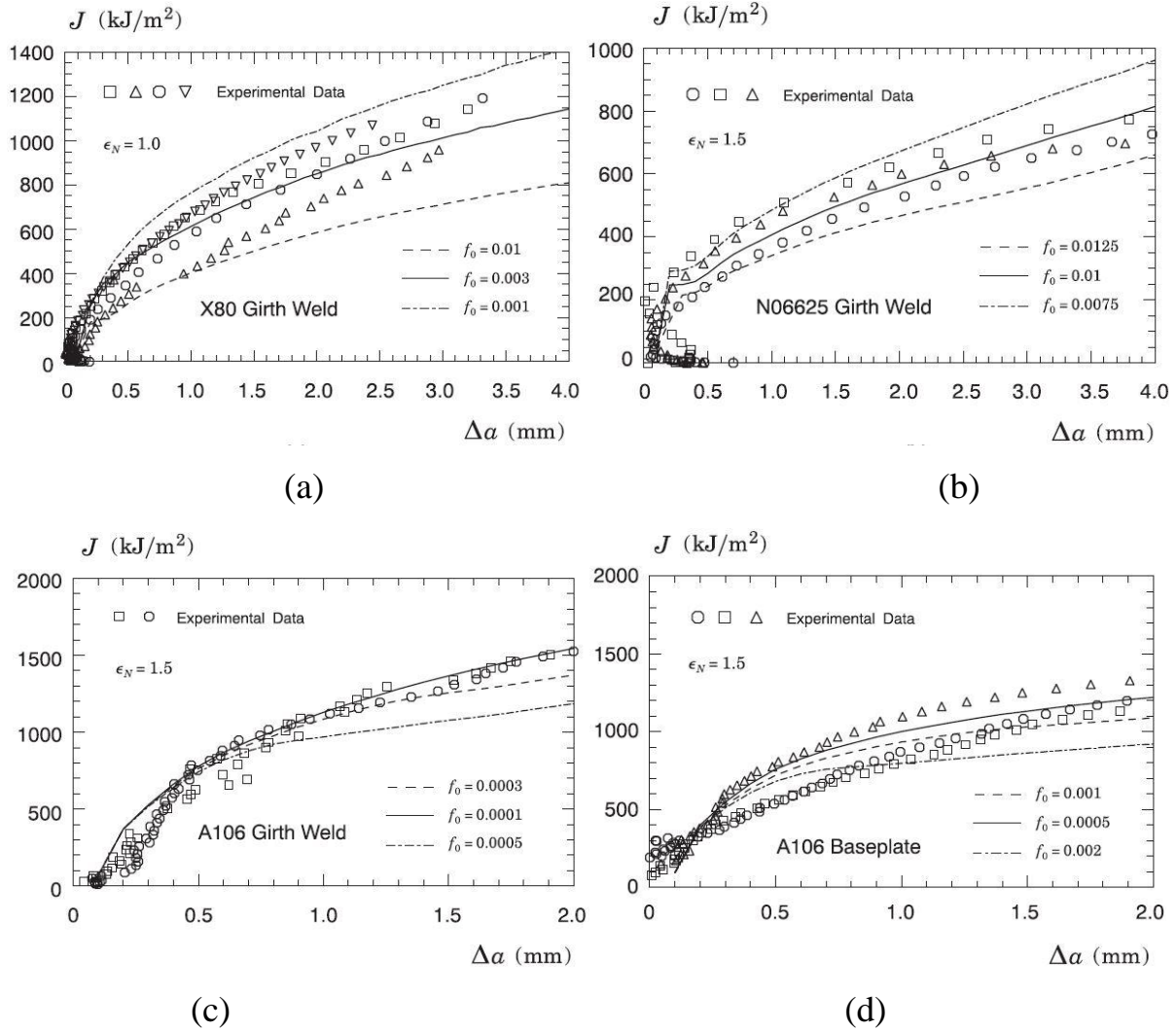
Table 5-1: Coefficients for the polynomial fitting of  $\eta_{J-CMOD}$ -values defined by equation 5.1

	<b>Girth Weld Material</b>	$b_0$	$b_1$	$b_2$	$b_3$
<b>2D</b>	API X80	0.950	0.622	-4.099	3.548
	UNs N06625	0.600	3.164	-9.506	7.461
	ASTM A106	1.015	-0.019	-1.839	1.064
<b>3D</b>	UNs N06625	0.717	2.003	-6.635	5.282

Table 5-2: Coefficients for the polynomial fitting of  $\eta_{J-LLD}$ -values defined by equation 5.2

	<b>Girth Weld Material</b>	$c_0$	$c_1$	$c_2$	$c_3$	$c_4$	$c_5$
<b>2D</b>	API X80	1.646	-10.023	57.288	-141.889	153.709	-60.667
	UNs N06625	1.380	-6.643	40.875	-103.908	111.500	-42.500
	ASTM A106	-9.281	112.627	-493.106	1067.842	-1141.875	479.000

Figure 53.: Predicted J- $\Delta a$  curves for the tested girth welds and the baseplate material using the cell size  $D/2=100\mu\text{m}$ ,  $fN=0.5$  and  $sN=0.05$  in all computations: (a) API X80. (b) UNS N06625 alloy. (c) ASTM A106 Gr C girth weld. (d) ASTM A106 Gr C baseplate steel.



The relatively close correspondence between the variation of  $\delta_{ECT}$  and  $\delta_{DCG}$  with  $\Delta a$  deserves further discussion. As already described, because  $\delta_{DCG}$  is defined as the crack opening at the position of the original crack tip, not the extending crack tip, it should rather be the case that  $\delta_{DCG}-\Delta a$  data should in general differ from the corresponding  $\delta_{ECT}$  resistance data. However, a different reason is offered here for the weak dependence of CTOD resistance data on the CTOD model, whether using the DCG procedure or the  $90^\circ$  intercept procedure based on the extending crack tip. Figure 5.5 shows the deformed profiles for the X80 girth weld test specimen at two different amounts of ductile tearing, as characterized by  $\Delta a = 2 \text{ mm}$  and  $\Delta a = 4 \text{ mm}$ - observe that the latter level of tearing is slightly larger than the maximum experimental

growth given in figure 3.3 (a). For both amounts of tearing, there is no sign of significant specimen rotation despite the large imposed remote loading which, in turn, causes the crack to open in a parallel fashion. Because the CTOD for the extending crack is defined here by the intercept between a straight line at  $45^\circ$  from the current crack tip and the deformed crack flanks, it is clear from the plots shown in figure 5.5 that  $\delta_{ECT}$  should compare well with  $\delta_{DCG}$  in the present framework.

Figure 54.: CTOD-resistance curves derived from plane-strain analysis using several procedures: (a) API X80. (b) UNS N06625 alloy. (c) ASTM A106 Gr C girth weld. (d) ASTM A106 Gr C baseplate.

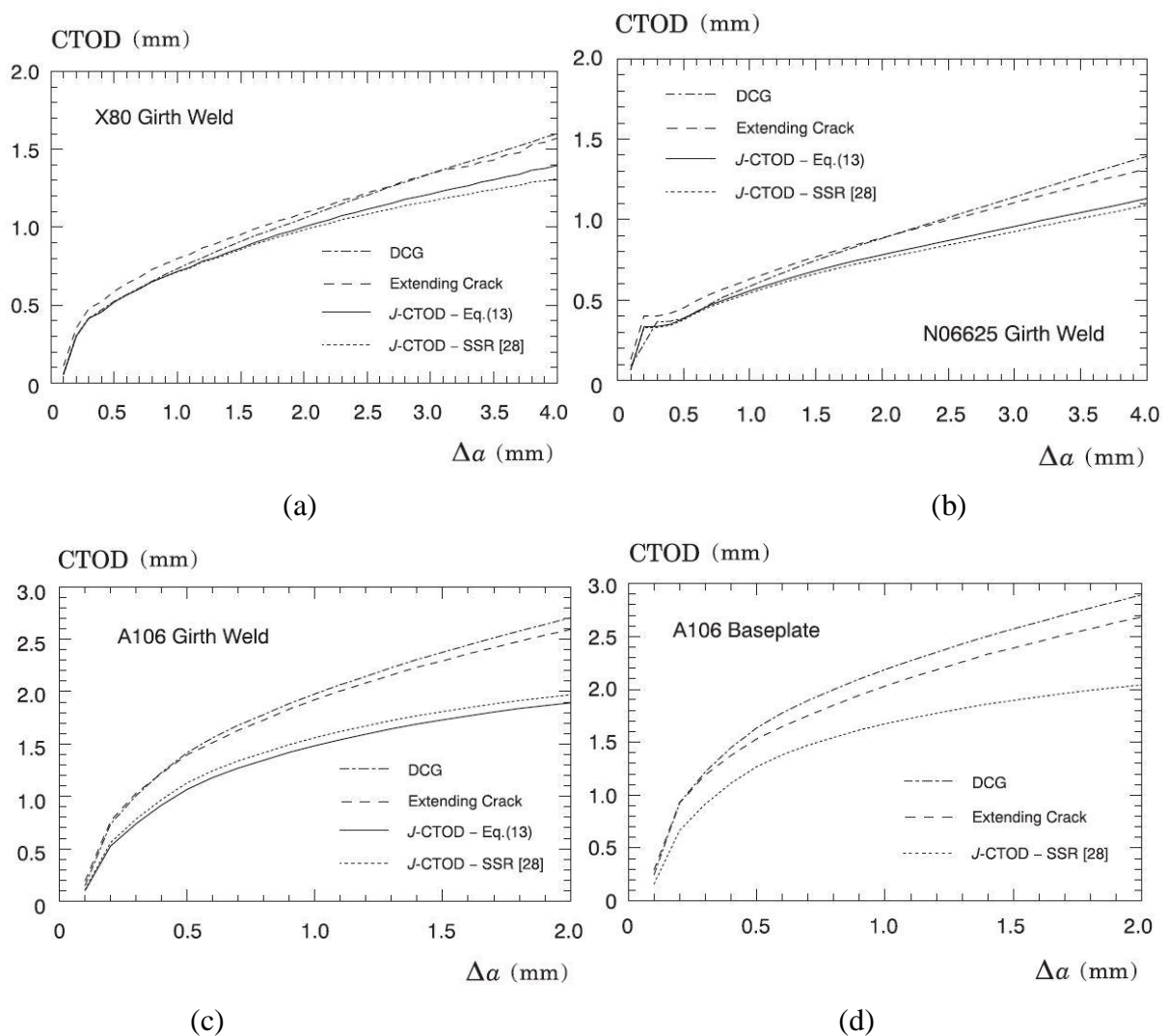


Table 5-3: Coefficients for the polynomial fitting of  $m$ -values defined by equation 5.3

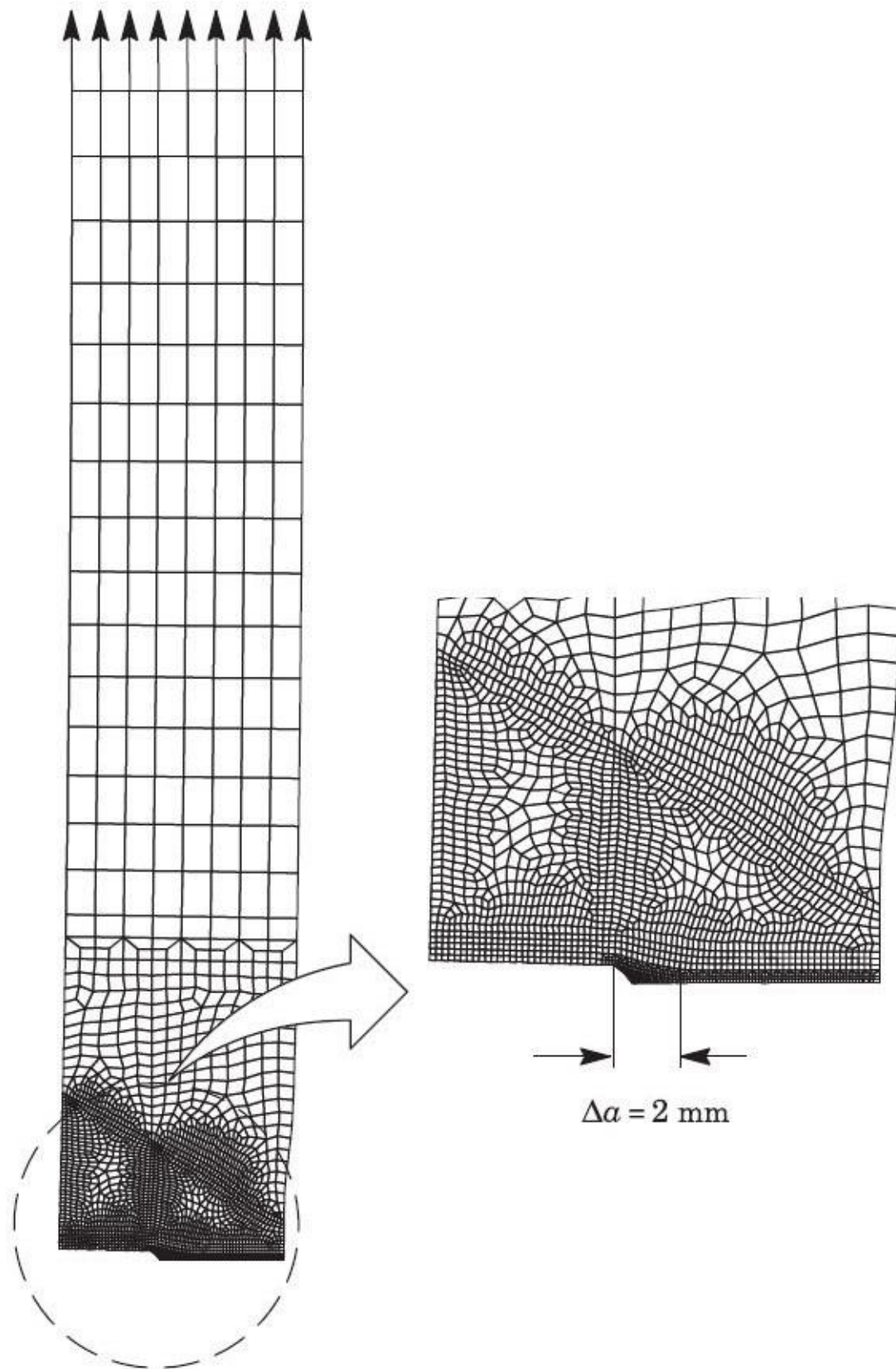


	<b>Girth Weld Material</b>	$d_0$	$d_1$	$d_2$	$d_3$
<b>2D</b>	API X80	1.256	-0.129	-0.068	-0.071
	UNs N06625	1.633	-1.531	2.544	-1.423
	ASTM A106	1.581	-0.626	0.424	-0.119
<b>3D</b>	UNs N06625	1.565	-0.731	1.541	-1.344

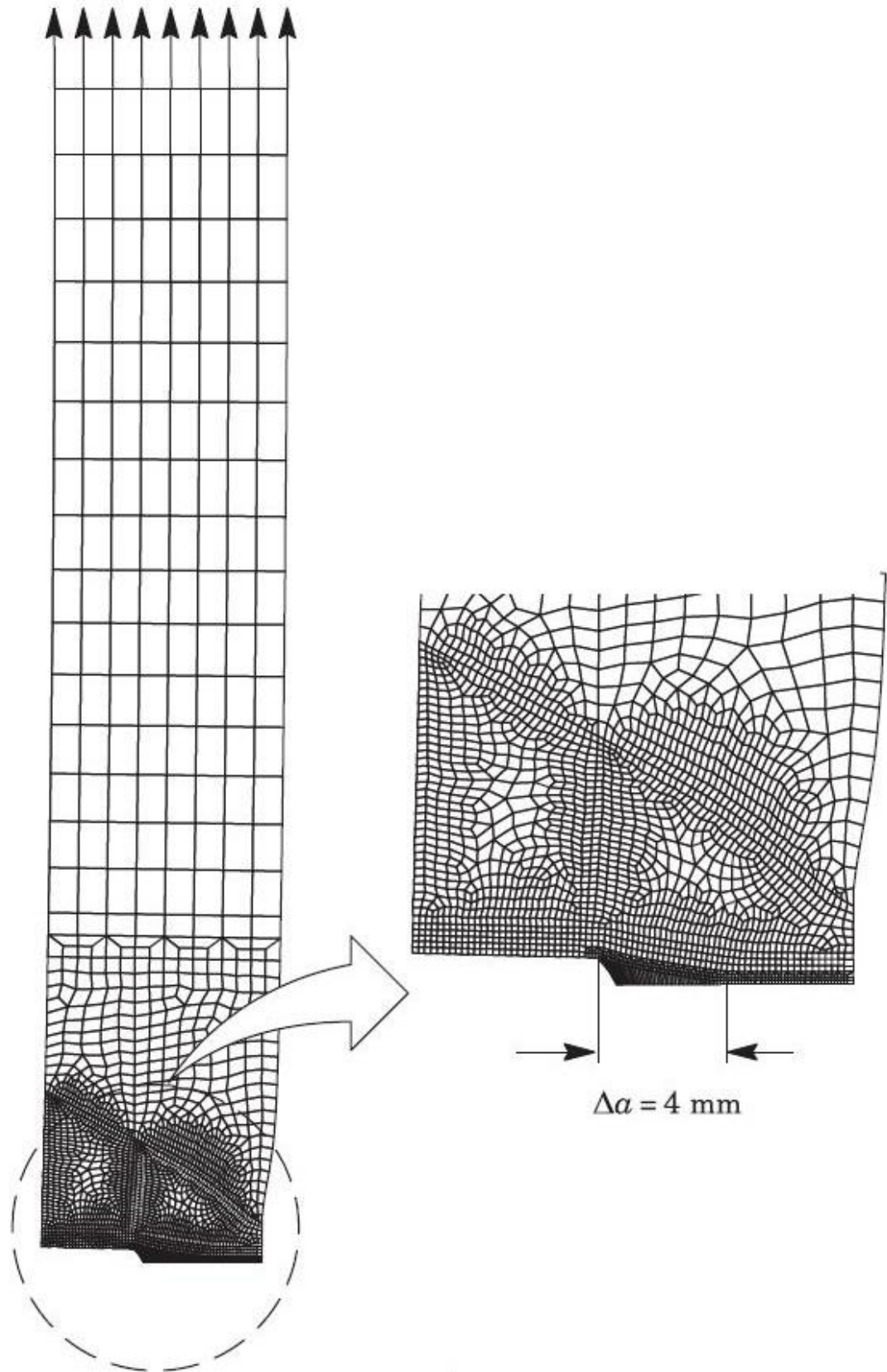
Table 5-4: Calibrated GTN parameters and factors  $q_1$ ,  $q_2$  derived from the work of Faleskog et al. [78] for all tested materials.

<b>Tested Material</b>	$e_N$	$f_0$	$q_1$	$q_2$
<b>API X80 Weld</b>	1.0	0.0030	1.58	1.04
<b>UNs N06625 Weld</b>	1.5	0.0100	1.52	0.92
<b>ASTM A106 Weld</b>	1.5	0.0001	1.75	0.80
<b>ASTM A106 Steel</b>	1.5	0.0005	1.45	0.95

Figure 55.: Deformed profiles for the X80 girth weld test specimen at two different amounts of ductile tearing: (a)  $\Delta a=2\text{mm}$ . (b)  $\Delta a=4\text{mm}$ .



(a)



(b)

### 5-3-3 CTOD-R Curves of the Dissimilar Ni-Cr Girth Weld Based on 3-D Analyses

The study thus far has focused on obtaining CTOD resistance data for the tested girth welds by determining CTOD values on the basis of 2-D, plane-strain analyses. Hence, it is natural to raise the question as to whether 3-D effects play a role in changing the ductile fracture response in terms of CTOD- $\Delta a$  data. For the purpose of addressing this issue, this section considers the evaluation of CTOD resistance curves for the dissimilar Ni-Cr girth weld based on  $\eta$ -factors and  $J$ -CTOD relationships derived from 3-D analyses of the V-groove weld model already previously described with the CTOD resistance data based on the DCG method measured by Sarzosa et al. [131].

Before undertaking these studies, additional insight can be gained by first examining 3-D effects on the  $J$  and CTOD distribution over the crack front for the tested girth welds under consideration. Figure 5.6 (a-b) display the distribution of  $J$  over the crack front, denoted  $J_{local}$ , with increased levels of loading for the 3-D V-groove weld model with  $a/W = 0.3$  and  $0.5$ ; this range of  $a/W$ -ratio represents the amount of ductile tearing ( $\sim 4$  mm) observed in the fracture tests. The  $J_{local}$ -values are normalized by the thickness average values, denoted  $J_{avg}$ , so that the ratio  $J_{local}/J_{avg}$  defines the relative change of the local  $J$ -value with the thickness average value of  $J$ . Note that the quantity  $J_{avg}$  describes the experimental measure of  $J$  that would be determined from a  $J$ -integral fracture test using the plastic work associated with load-displacement records [11, 19, 62, 64]. Figure 5.6 (c-d) show the corresponding distribution of CTOD, as defined by the  $90^\circ$  intercept procedure, over the crack front, denoted  $\delta_{local}$ , normalized by the CTOD-value evaluated at the specimen midplane, denoted  $\delta_{z=0}$ .

The results shown in figure 5.6 (a-b) reveal that, while the maximum  $J$ -values occur over a relatively small portion of the specimen midplane region ( $0 \leq Z/(B_N/2) \leq 0.3$ ) for both  $a/W$ -ratios, they gradually decrease to smaller  $J$ -values, which are nevertheless relatively close to the midplane values as the side-groove region is approached. By contrast, the distributions of  $\delta_{local}$  across the specimen net thickness shown in figure 5.6 (c-d) are uniform over the entire crack front. Further, observe that the  $\delta_{local}$ -values are virtually indistinguishable from the midplane CTOD value. Such results are consistent with the expected behavior of a tension-loaded specimen, such as the clamped SE(T) geometry analyzed here, indicated in the deformation plots shown in figure 5.5 since the crack faces clearly open rather uniformly over the entire crack front. Moreover, since the CTOD conventionally measured in fracture tests is actually defined by crack tip opening displacement evaluated at the specimen midplane, the

results provided in figure 5.6 also indicate a good correlation between the experimentally measured CTOD and thickness average value of  $J$ .

Now, a similar approach as before may be followed to evaluate the  $J$ -resistance curves for the UNS N06625 girth weld in which new  $\eta$ -factors derived from the 3-D analysis of the V-groove weld model are employed to evaluate the  $J$ -values at each partial unloading point. Tables 5.1 and 5.2 also provides the fitting coefficients derived from the 3-D models that were used in conjunction with equations 5.1 and 5.2 to obtain new fracture resistance data for this girth weld. Figure 5.7 (a) displays the  $J$ -resistance curves in which the effect of crack growth correction on  $J$ - $\Delta a$  data is also examined. These results show that crack growth correction (open symbols) lowers the measured fracture resistance curves by 10–15% for  $\Delta a \geq 3$  mm compared to the uncorrected data (solid symbols); this finding is fully in accord with previous experimental studies by Mathias et al. [10].

Numerical evaluation of the  $J$ - $\Delta a$  response for the 3-D finite element model incorporating crack growth now proceeds by calibrating the set of GTN parameters that establish the best agreement with the  $J$ -resistance data shown in figure 5.7 (a). Because our primary interest here lies in the correlation of CTOD- $\Delta a$  data derived from the 3-D numerical analysis with the CTOD resistance curve measured by Sarzosa et al. [136], the calibration procedure focuses on the uncorrected  $J$ -resistance data (*i.e.*, without crack growth correction). Figure 5.7 (b) recasts the uncorrected fracture resistance data and includes the predicted resistance curve obtained by using  $\varepsilon_N = 1.5$  and  $f_0 = 0.01$  while keeping other parameters the same as the plane-strain analyses already described. In the context of the present 3-D analysis, numerical evaluation of ductile crack extension,  $\Delta a$ , is performed in a similar fashion to the 9-point procedure adopted by current fracture resistance test procedures, including ASTM E1820 [70]. Hence, the amount of crack growth associated with the predicted fracture resistance response represents the average crack extension not the midplane growth. Apart from the early stage of ductile crack growth, generally good agreement exists between the measured data and the computed resistance curve.

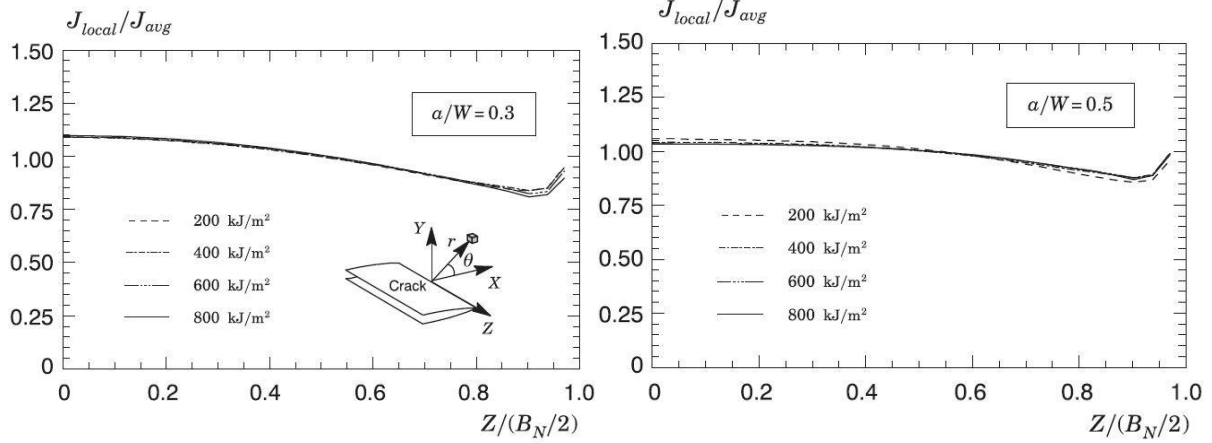
We will now use the numerical  $J$ -resistance curve in figure 5.7 (b) to determine the corresponding CTOD resistance data including 3- D effects on the fracture response for the tested specimens and how it compares with the experimental CTOD-resistance curves for this N06625 girth weld reported by Sarzosa et al. [136] using the DCG technique. For this purpose, we also consider a new  $J$ -CTOD relationship, as characterized by parameter  $m$ , derived from the 3-D analysis of the V-groove weld model given by equation 5.3 with the fitting coefficients

also given in Table 5.3. Figure 5.8 compares the CTOD-resistance curve derived from using equation 2.10 with the new  $J$ -CTOD relationship in 3-D setting and the corresponding CTOD- $\Delta a$  data in which the double clip gage (DCG) method is employed to generate CTOD values for the 3-D numerical model of the V-groove weld. To illustrate the 3-D effects on the computed fracture resistance data, the figure also includes the CTOD resistance curve derived from the DCG procedure based on plane-strain results displayed in previous figure 5.4 - note here that those results are generated from a  $J$ -resistance curve which incorporates crack growth correction.

The trend displayed by these results is clear as the CTOD- $\Delta a$  data derived from the DCG method lie above the corresponding fracture resistance curve based on the computed  $J$ -CTOD relationship. Further, the plane-strain DCG results are in relatively close agreement with the present 3-D analysis, a behavior which is consistent with the observed 3-D effects on the  $J$  and CTOD distribution over the crack front shown in figure 5.6. The tendency for the CTOD resistance curve based on the DCG procedure to lie always above the CTOD- $\Delta a$  data derived from the  $J$ -CTOD relationship has also been noted in previous efforts to investigate fracture resistance behavior in terms of CTOD by Sarzosa et al. [136] and Weeks and Lucon [31]. At the same time, it is clear from the figure that the computed CTOD resistance curve based on the DCG method agrees relatively well with the measured data, albeit lying somewhat below the experimental resistance curve. While we have not explored the source of the small deviation between both CTOD resistance curves based on the DCG method, these results suggest a potential effect of key test parameters on the measured data. For example, the 3-D numerical model has a straight, through crack whereas the crack front of the tested fracture specimen not only exhibits a certain degree of curvature but the crack front is also rather nonuniform [137]. Aside from these uncertainties, the double clip gage method no doubt produces higher CTOD resistance curves compared with the corresponding fracture resistance data based on  $J$ -CTOD relationships which, thus, gives nonconservative estimates of fracture toughness.

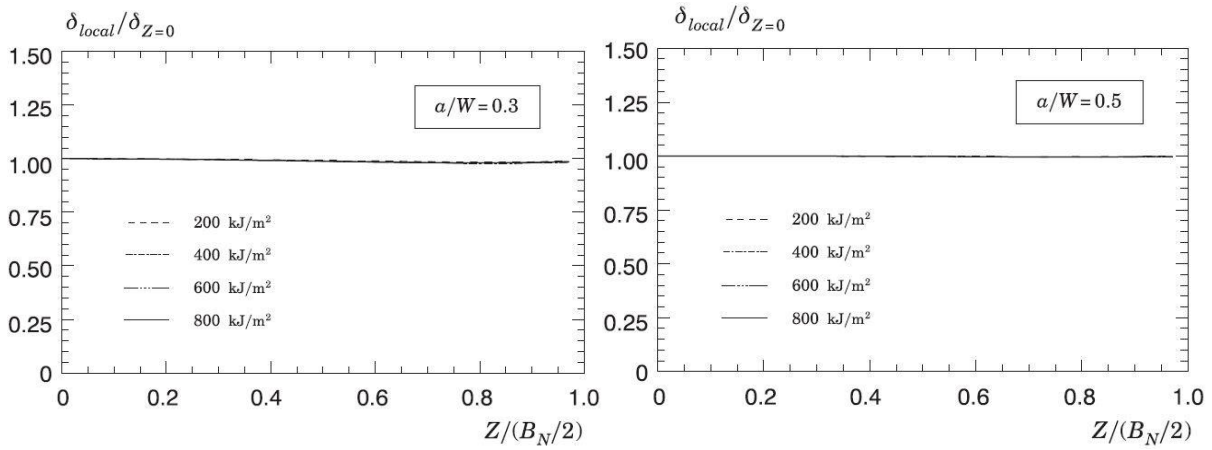
Figure 56.: (a) Distribution of  $J$  over the crack front, denoted  $J_{local}$ , with increased levels of loading for the 3-D V-groove weld model with  $a/W=0.3$  and  $0.5$ . (b) Distribution of CTOD, as defined by

the 90° intercept procedure, over the crack front, denoted  $\delta_{local}$ , with increased levels of loading for the 3-D V-groove weld model with  $a/W=0.3$  and 0.5.



(a)

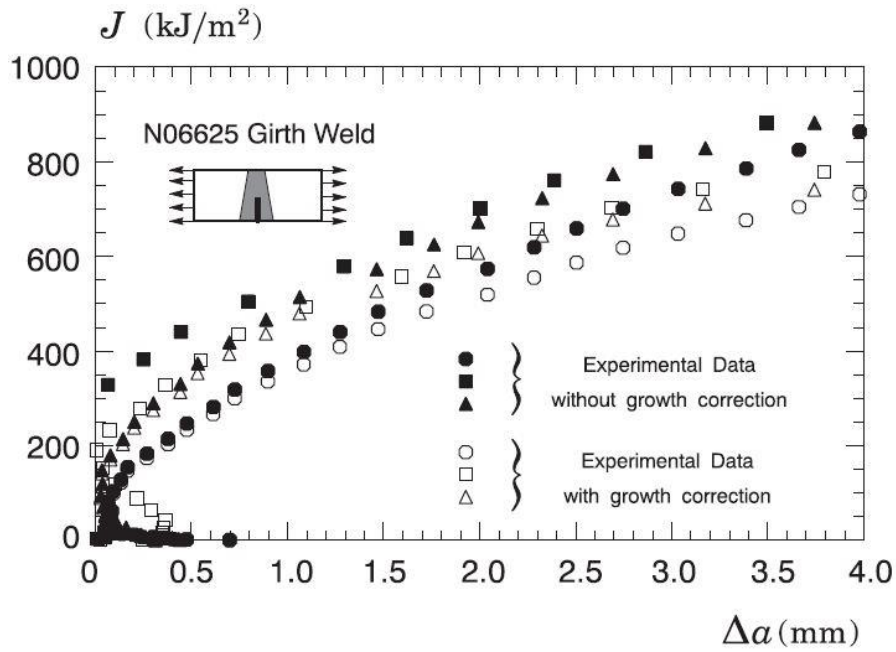
(b)



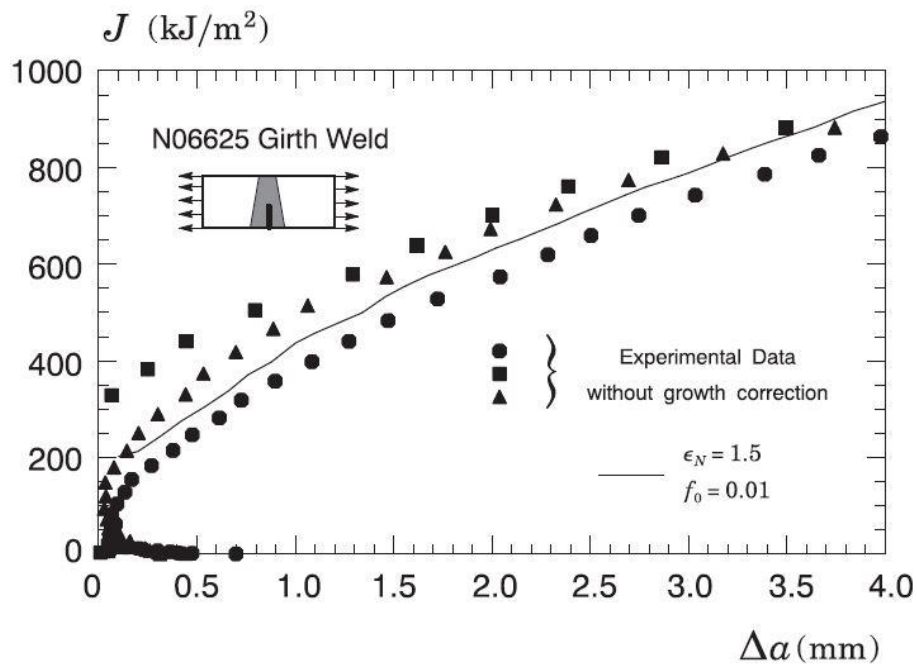
(c)

(d)

Figure 57.: (a)  $J$ -resistance curves for the UNS N06625 girth weld with new  $\eta$ -factors derived from the 3-D analysis of the V-groove weld model. (b) Predicted  $J$ - $\Delta a$  curve for the uncorrected data (without crack growth correction) using  $\epsilon_N=1.5$  and  $f_0=0.01$ .



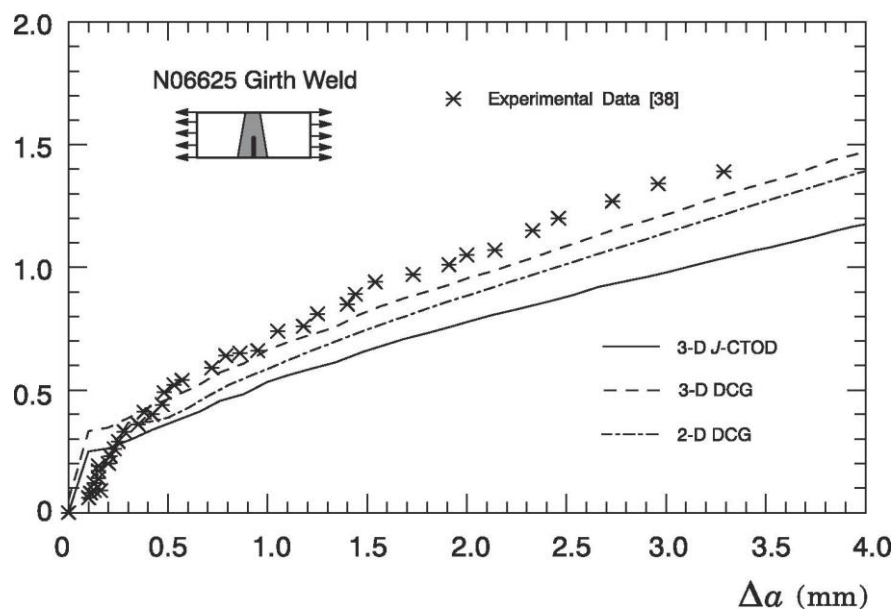
(a)



(b)



Figure 58.: Comparison of CTOD resistance curves derived from the double clip gage method and J-CTOD relationship for the 3-D V-groove weld model of the UNS N06625 girth weld.

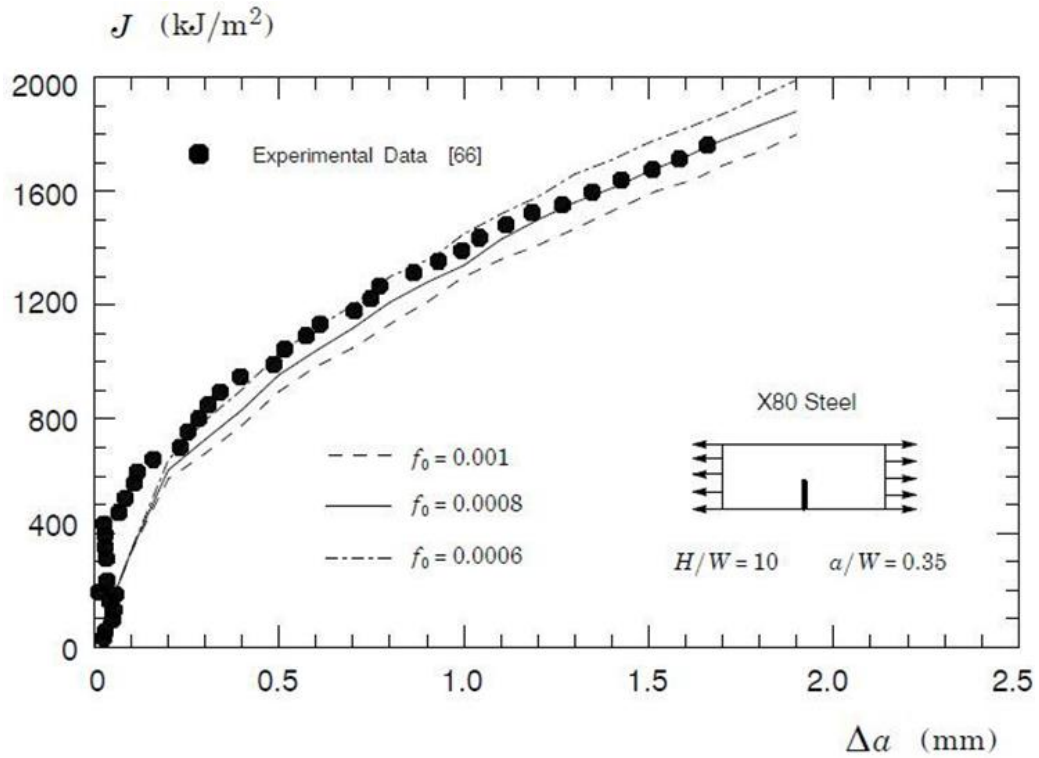


## 5-4 Comparison of R-curve in SE(T) specimen and actual pipe

### 5-4-1 X80 pipeline steel

Bayley [138] provides  $J$ -resistance test results and mechanical properties for an X80 pipeline steel derived from a round robin testing program conducted by BMT Fleet and PRCI to further validate a test protocol to measure the fracture toughness of steels and welds using clamped SE(T) specimens. The tested geometry has  $a/W = 0.35$  with thickness  $B = 14\text{mm}$ , width  $W = 14\text{mm}$ ,  $H = 140\text{mm}$  and 5% side-groove on each side. Figure 5.9 displays the average crack growth resistance curve at room temperature obtained by the unloading compliance (UC) procedure to generate  $J-\Delta a$  data for the tested material reported in Bayley [138].

Figure 59.: Predicted  $J$ - $\Delta a$  curves for the X80 pipeline steel tested by Bayley [138] obtained by crack growth analyses performed on the clamped SE(T) specimen using the cell size  $D/2 = 100\mu m$ ,  $f_N = 0.5$  and  $s_N = 0.05$  with  $\varepsilon_N = 2.0$ .



Figur 5.9 shows the predicted  $J$ - $\Delta a$  curves using the cell size  $D/2 = 100 \mu m$ ,  $f_N = 0.5$ ,  $s_N = 0.01$  with  $\varepsilon_N = 2$  and three values of the initial volume fraction as shown in the plot. Moreover, all the computations use  $q$ -values for the material analyzed derived from Faleskog and Shih [89], which are given as  $q_1 = 1.38$ ,  $q_2 = 0.99$  and  $q_3 = q_1^2$ . For  $f_0 = 0.0008$ , the predicted  $R$ -curve agrees relatively well with the measured fracture resistance values for almost the entire range of growth. Further, the use of  $f_0 = 0.001$  and  $f_0 = 0.0006$  provides a more visible departure of the predicted resistance curves relative to the measured fracture resistance data. Observe that the early part of the curve in which  $\Delta a \leq 0.5 \text{ mm}$  is relatively not well described by the numerical resistance curve, a behavior which is associated with the rather poor representation of the crack blunting and initiation process by the cell model [45]. However, since the primary interest here lies in the description of fracture resistance as a means to determine the CTOD for an extending crack under conditions of stable crack growth, such behavior is not of particular concern.

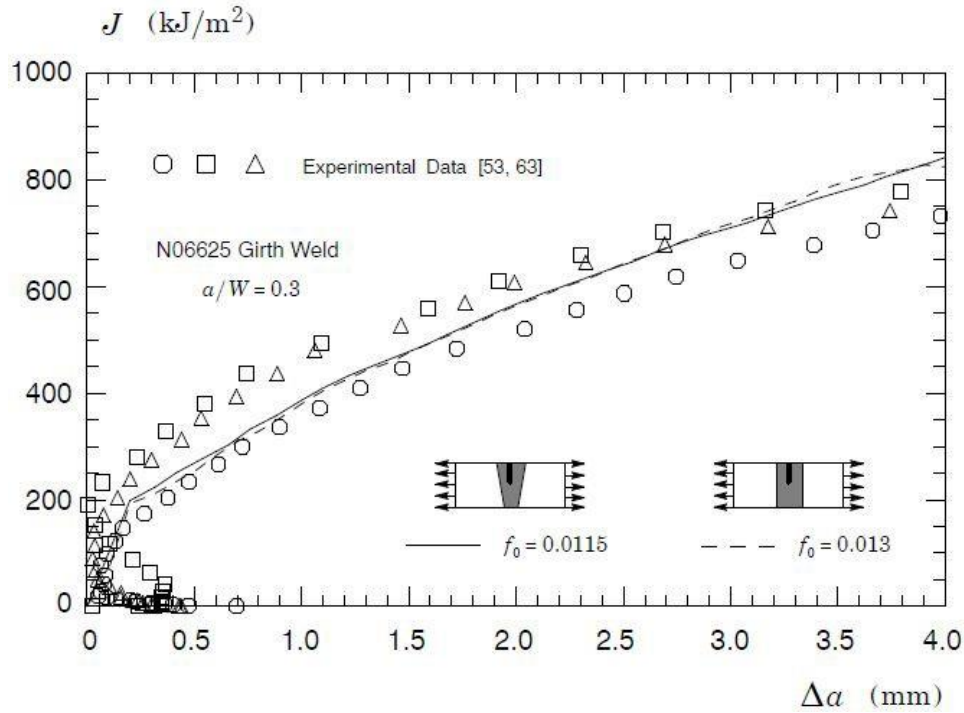
#### 5-4-2 Dissimilar Ni-Cr Girth Weld

Sarzosa et al. [132] performed fracture resistance tests at room temperature on weld centerline notched SE(T) specimens under fixed-grip conditions based on the UC method. The welded specimens were fabricated from a girth weld of a API X65 steel pipe internally clad with a thin layer of a nickel-based corrosion resistant alloy (CRA) made of Inconel 625 alloy (UNS designation N06625 [1, 2]). The girth weld was produced using a nickel-chromium filler metal matching the 3mm thick, nickel-based CRA material layer thereby ensuring very similar mechanical properties for either the clad internal layer and the weld metal. The clamped SE(T) specimen has  $a/W = 0.3$  with thickness  $B = 16mm$ , width  $W = 16mm$ ,  $H = 160mm$  and 7.5% side-groove on each side.

Using the same calibration protocol as before, Figure 5.10 displays the predicted  $J$ -resistance curves for the tested girth welds for the two weld groove models under consideration. Here, the cell size is also taken as  $D/2 = 100\mu m$  with  $f_N = 0.5$  and  $s_N = 0.05$  and a slightly smaller  $\varepsilon_N$ -value of 1.5 in comparison to the previous analysis. Further, similarly to the previous analyses, these computations use the  $q$ -values taken from Faleskog and Shih [89] and are given as  $q_1 = 1.52$ ,  $q_2 = 0.92$  and  $q_3 = q_1^2$ . Despite the inherent scatter in the experimental  $J - \Delta a$  results, the predicted R-curves agree well with the average fracture resistance data for both cases, particular for amounts of stable crack growth in the range  $\Delta a \leq 2.5mm$ . Further observe that the numerical resistance curves display little sensitivity to the weld groove model as the calibrated initial porosity values are  $f_0 = 0.0115$  for the V-groove geometry and  $f_0 = 0.013$  for the square groove configuration derived from the homogenization approach.

Figure 510.: Predicted  $J - \Delta a$  curves for the N06625 girth weld tested by Sarzosa et al. [132] obtained by crack growth analyses performed on weld centerline notched SE(T) specimens having a

V-groove model and a square groove model with the cell size  $D/2 = 100\mu m$ ,  $f_N = 0.5$  and  $s_N = 0.05$  with  $\varepsilon_N = 1.5$ .

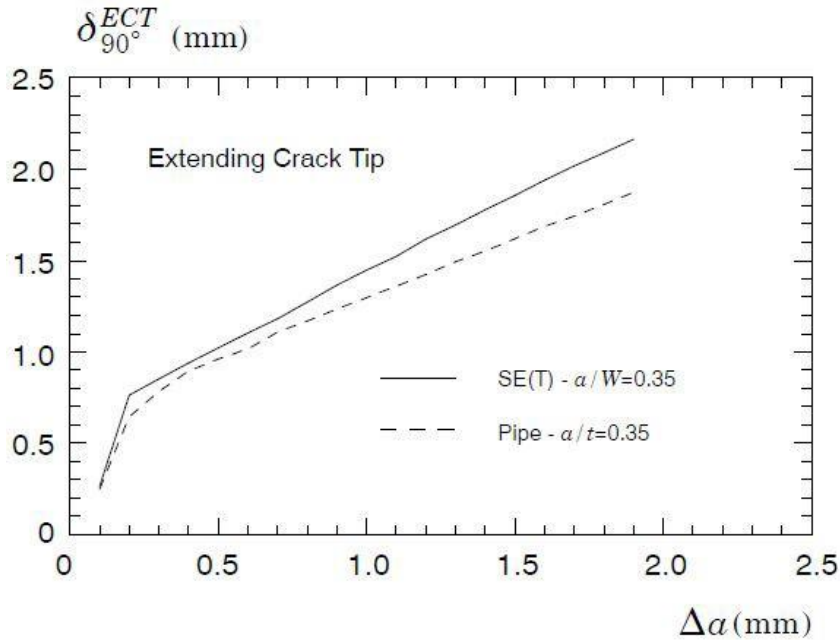


Before launching into the analyses to compare predictions of ductile crack extension in Ni-based clad pipe girth welds, we first generate predictions of  $CTOD - R$  curves for the pipe geometry under bending made of an API X80 steel and having a circumferential surface crack with  $2c = 100mm$  and  $a/t = 0.35$ . The analysis thus serves as a validation study of the approach pursued in the present work since there are no potential effects of weld strength mismatch coupled with weld groove geometry and clad layer on the predicted ductile fracture behavior.

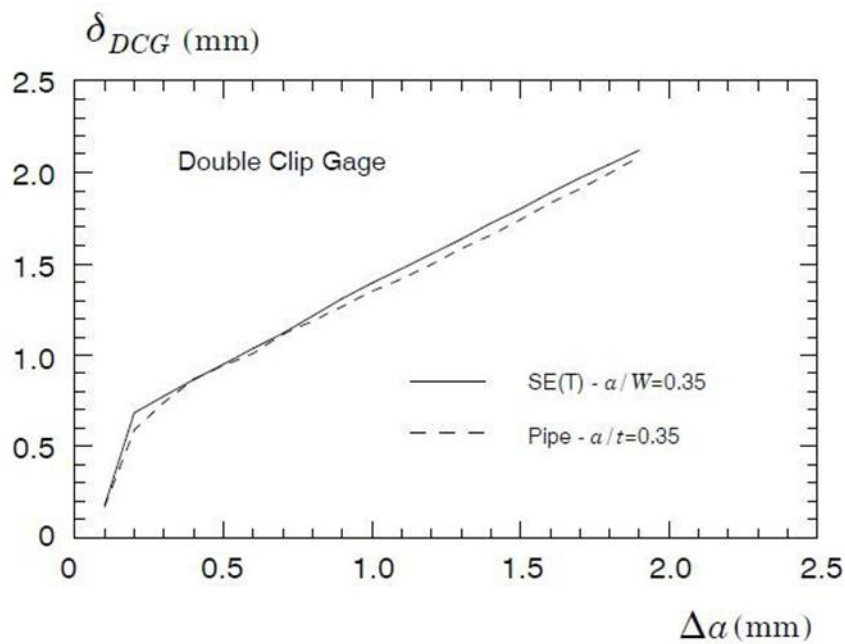
Figure 5.11 compares the  $CTOD$ -resistance curves derived from 3D analyses of crack extension for the clamped SE(T) specimen with  $a/W = 0.35$  and a circumferentially cracked pipe under bending with  $a/t = 0.35$  using two different procedures to evaluate the  $CTOD$ , namely the extending crack tip (ECT) approach and the double clip-gage (DCG) method. While the differences between the R-curves obtained by both procedures, particularly in the range of  $\Delta a \leq 1.0mm$ , are not very significant, there are nonetheless important features that deserve additional discussion. Observe that the  $CTOD$ -resistance curves for the clamped SE(T) specimen are highly comparable, such that the  $CTOD$ -value for a given amount of crack growth is relatively insensitive to the  $CTOD$  evaluation procedure in this case. More importantly, though, further observe that the DCG procedure gives  $CTOD - R$  curves for the

SE(T) specimen and the cracked pipe in much closer agreement than the corresponding crack growth resistance results derived from the extending crack tip approach.

Figure 511.: *CTOD* resistance curves for the X80 pipeline steel derived from 3D analyses of crack extension for the clamped SE(T) specimen with  $a/W = 0.35$  and a circumferentially cracked pipe with  $a/t = 0.35$ : (a) *CTOD* determined by the extending crack tip procedure. (b) *CTOD* evaluated by the double clip-gage (DCG) method



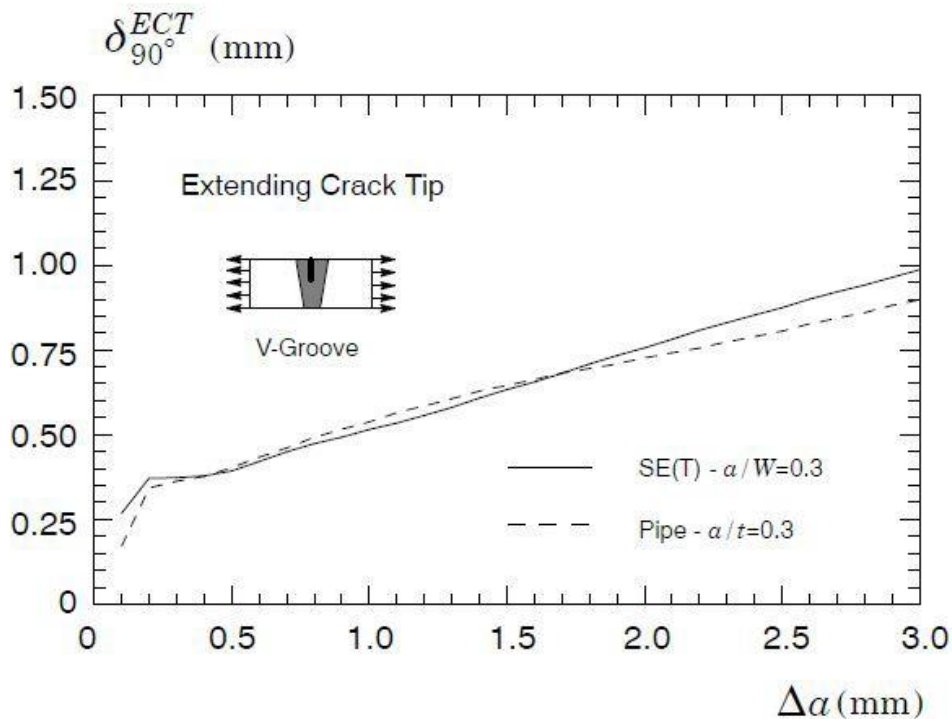
(a)



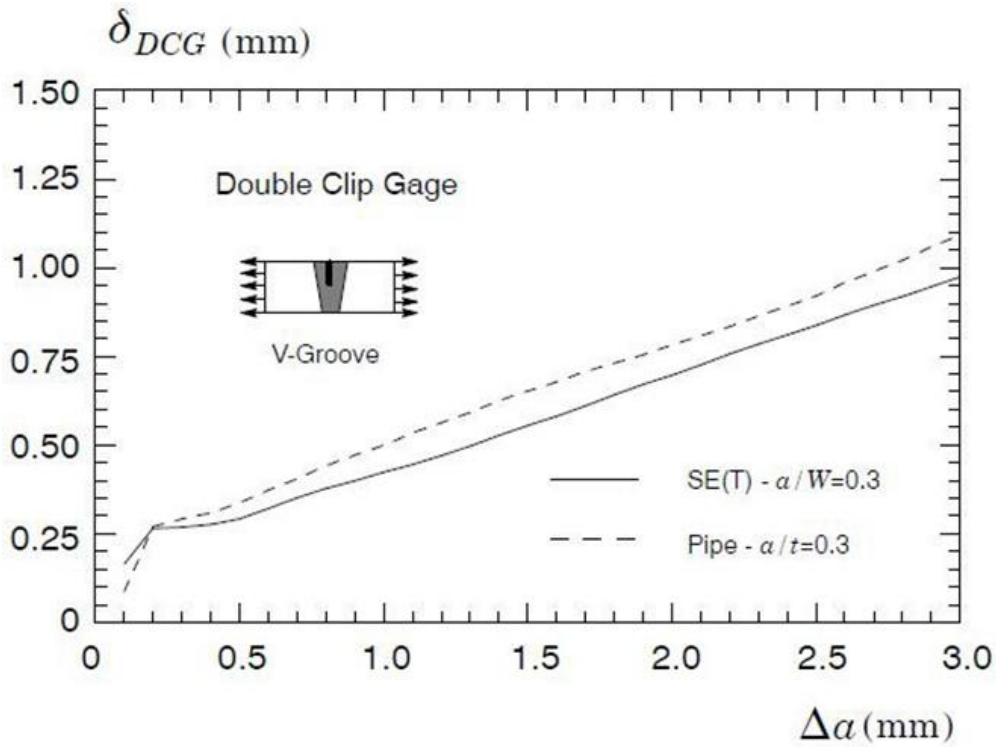
(b)

The same analysis as above is followed for the primary case of interest which addresses the correlation of *CTOD*–resistance curves between clamped SE(T) specimens and circumferentially cracked pipes having a dissimilar Ni-Cr weld. Figure 5.12 and 5.13 compares the variation of *CTOD* with increased amounts of ductile tearing,  $\Delta a$ , derived from 3D analyses of crack extension for the clamped SE(T) specimen with  $a/W = 0.3$  and the circumferentially cracked pipe under bending with  $a/t = 0.3$ . These figures illustrate the effects of different procedures to evaluate the *CTOD* and also compare the influence of the weld groove model on the predicted R-curves.

Figure 512.: *CTOD* resistance curves for the UNS N06625 girth derived from 3D analyses of crack extension incorporating the V-groove model for the clamped SE(T) specimen with  $a/W = 0.3$  and a circumferentially cracked pipe with  $a/t = 0.3$ : (a) *CTOD* determined by the extending crack tip procedure. (b) *CTOD* evaluated by the double clip-gage (DCG) method.

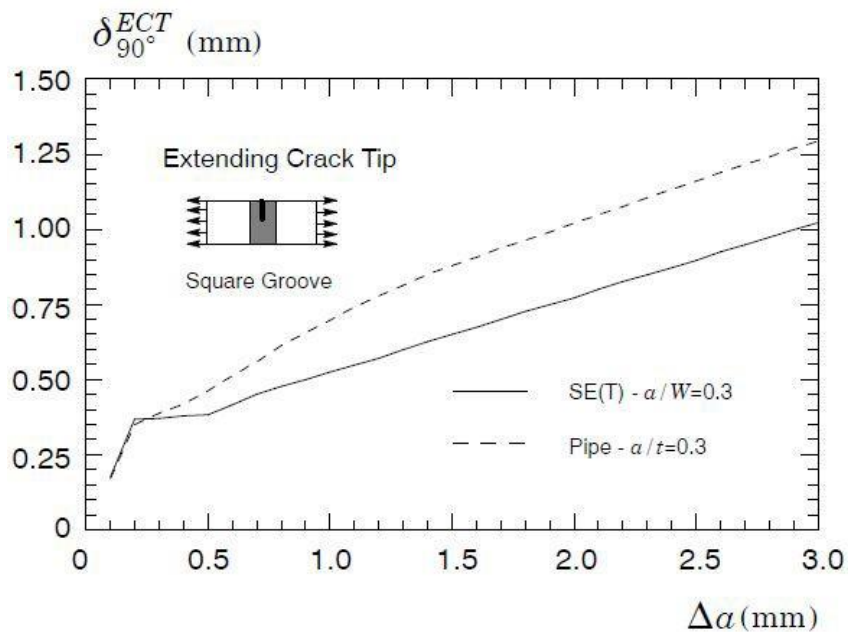


(a)

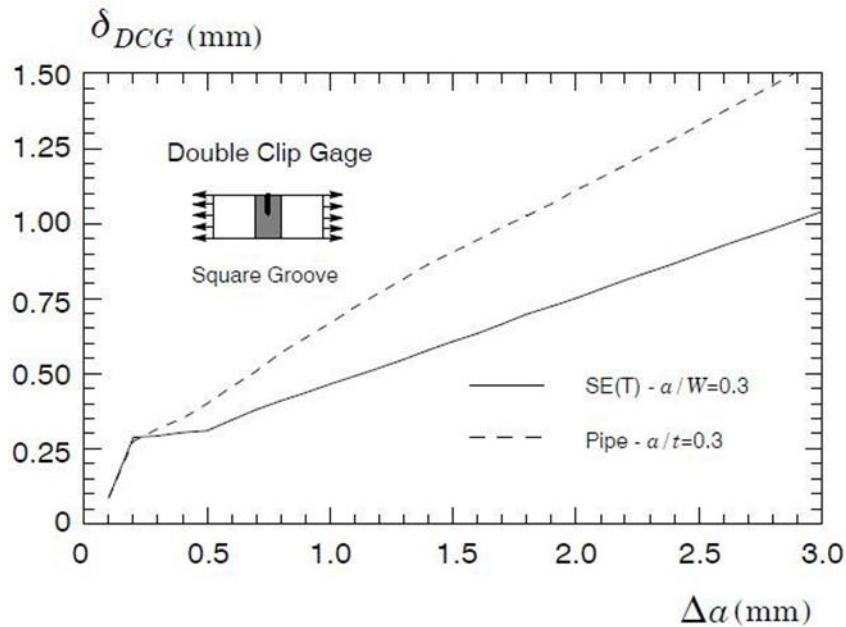


(b)

Figure 513.:  $CTOD$  resistance curves for the UNS N06625 girth derived from 3D analyses of crack extension incorporating the square groove model for the clamped SE(T) specimen with  $a/W = 0.3$  and a circumferentially cracked pipe with  $a/t = 0.3$ : (a)  $CTOD$  determined by the extending crack tip procedure. (b)  $CTOD$  evaluated by the double clip-gage (DCG) method.



(a)



(b)

Consider first the results for the V-groove model shown in Figure 5.12. The significant features include: 1) the  $CTOD-R$  curves for the SE(T) specimen and the cracked pipe based on the ECT method are highly comparable; 2) the R-curve for the SE(T) specimen is slightly more conservative than the corresponding resistance curve for the cracked pipe when the DCG procedure is used to evaluate the  $CTOD$ , and 3) the DCG procedure provides lower crack growth resistance curves in comparison with the ECT method for both analyzed crack configurations.

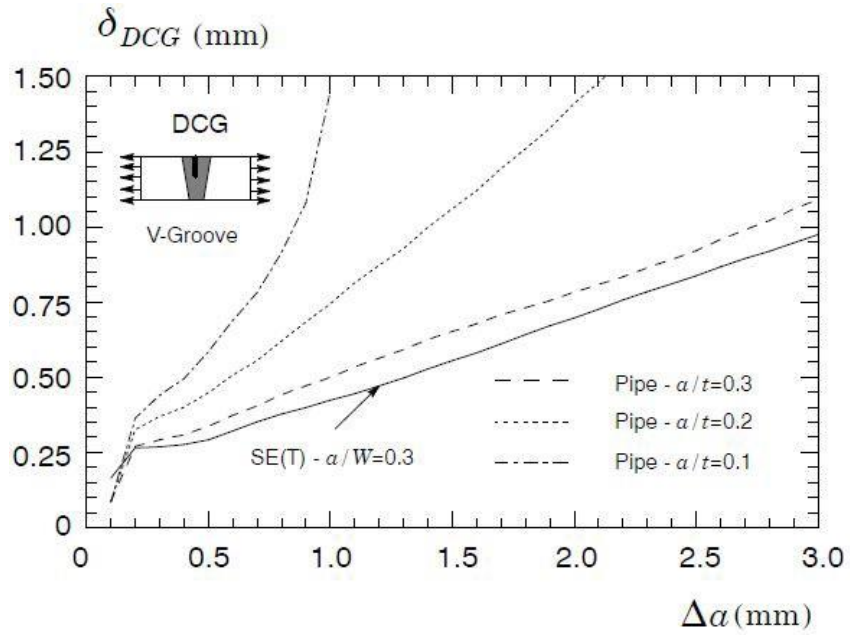
Consider next the square groove results displayed in Figure 5.13. A different picture now emerges as the  $CTOD$ -resistance curves depend more markedly on the  $CTOD$  evaluation method and crack configuration. Indeed, observe the much larger differences in the R-curve between the SE(T) specimen and the cracked pipe for both  $CTOD$  evaluation procedures, particularly in the case of the DCG approach. Further observe that the R-curves for the SE(T) specimen derived from either the ECT procedure and the DCG method are essentially similar. Therefore, the differences between the  $CTOD$ -resistance curves for the SE(T) specimen and the cracked pipe actually arise from a more prominent effect of the  $CTOD$  evaluation procedure in the case of the circumferentially cracked pipe.

The previous results and associated conclusions just discussed have the common feature of involving crack configurations with the same relative crack depth given by  $a/W = a/t = 0.3$ . These analyses can be extended to other cases of interest by considering the correlation of the  $CTOD$ -resistance curve for the SE(T) specimen with  $a/W = 0.3$  with the

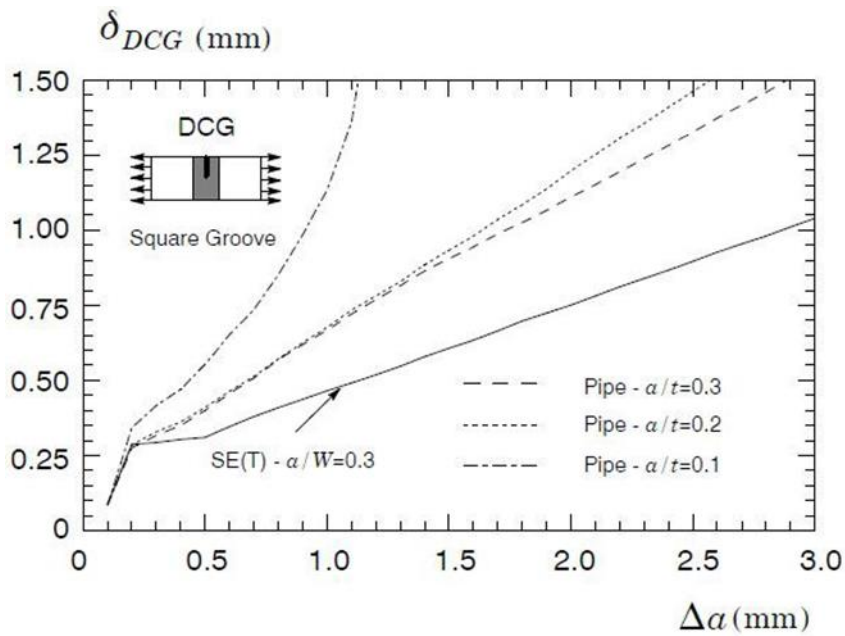


fracture resistance behavior of circumferentially cracked pipes having shallow cracks in the range of  $a/t = 0.1$  and  $0.2$ . This additional range of crack depth over pipe thickness ratio falls within typical flaw depths adopted in fitness-for-service analyses performed during the installation of submarine pipelines, including production and gas-lift pipelines. Figure 5.14 shows the  $CTOD$ –resistance curves based on the double clip-gage (DCG) method for the UNS N06625 girth derived from 3D analyses of crack extension for the circumferentially cracked pipes with  $a/t = 0.1, 0.2$  and  $0.3$  incorporating the V-groove and square groove model. The results shown in this plot reveal similar trends as before in which the SE(T) specimen always provides conservative crack growth resistance curves based on the DCG  $CTOD$  compared to those corresponding to the circumferentially cracked pipes. Observe that, for the case of the V-groove model, the  $CTOD$ –resistance curve for the pipe with  $a/t = 0.2$  differs rather markedly from the resistance curve of the pipe with  $a/t = 0.3$ , whereas for the case of the square groove model both  $CTOD - R$  curves are similar, particularly up to  $\Delta a \approx 1.5\text{mm}$ . Now direct attention to the crack growth resistance curves for the pipe with  $a/t = 0.1$ . Here, the  $CTOD$  increases rather sharply with increased amounts of ductile tearing for both weld groove models. This behavior can be understood by considering that this pipe configuration with a very shallow crack has exceptionally low levels of crack tip constraint, which, in turn, suppress crack extension by a void growth mechanism. Under this condition, the  $CTOD$  increases with increased loading so that, with crack growth suppressed, the final failure is likely to occur by plastic collapse of the remaining crack ligament with little amounts of ductile tearing. Despite these features, the trends displayed by these results are unmistakable, in that a clamped SE(T) specimen having a dissimilar Ni-Cr weld provides  $CTOD$ –resistance curves based on the DCG  $CTOD$  that describe well, albeit conservatively, the ductile fracture behavior of corresponding dissimilar Ni-based clad pipe girth welds with circumferential surface cracks.

Figure 514. : *CTOD* resistance curves based on the double clip-gage (DCG) method for the UNS N06625 girth derived from 3D analyses of crack extension for the circumferentially cracked pipes with  $a/t = 0.1, 0.2$  and  $0.3$ : (a) V-groove model. (b) Square groove model.



(a)



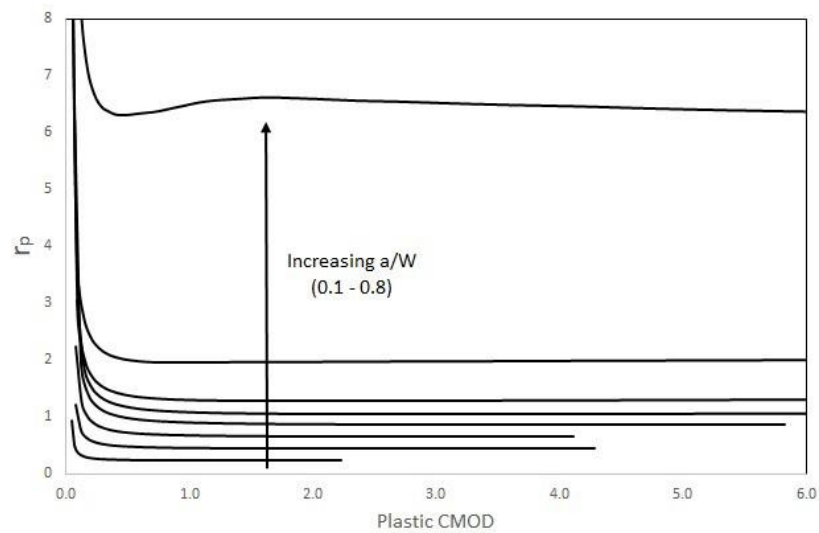
(b)

### 5-5 R-curves using plastic rotational factor

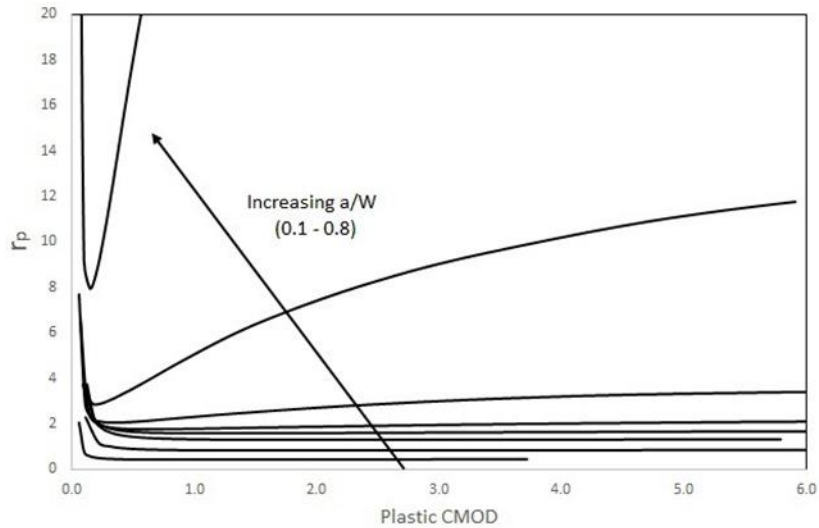
We investigated the R-curves using DCG method. Although DCG method has gained a great attention during recent decades, it has some difficulties to take advantage of it. Usually,

experimental setup to measure CMOD at two different points is a little bit complicated and hard to carry out. Therefore, we were requested to investigate deriving R-curve using CMOD only at one point. Here we take advantage of  $r_p$  method which is explained earlier in the literature review chapter, but first we have to check  $r_p$  variation with material properties and loading. Here we cannot use the standard recommendation as  $r_p = 0.4$  since this value is limited to deeply cracked SE(B) specimen which is not our interest specimen. Therefore, initially we conducted some general investigation on homogeneous materials with various hardening levels as: 1)  $n = 20$  and  $E/\sigma_0 = 300$  2)  $n = 10$  and  $E/\sigma_0 = 500$  3)  $n = 5$  with  $E/\sigma_0 = 800$ , assuming  $E = 206 \text{ GPa}$ . A wide range of plane strain models with  $a/w$  ratios ranging from 0.1 to 0.8 with increments of 0.1 were investigated to observe  $r_p$  variation. Figure 5.15 indicates the  $r_p$  as a function of plastic portion of CMOD.

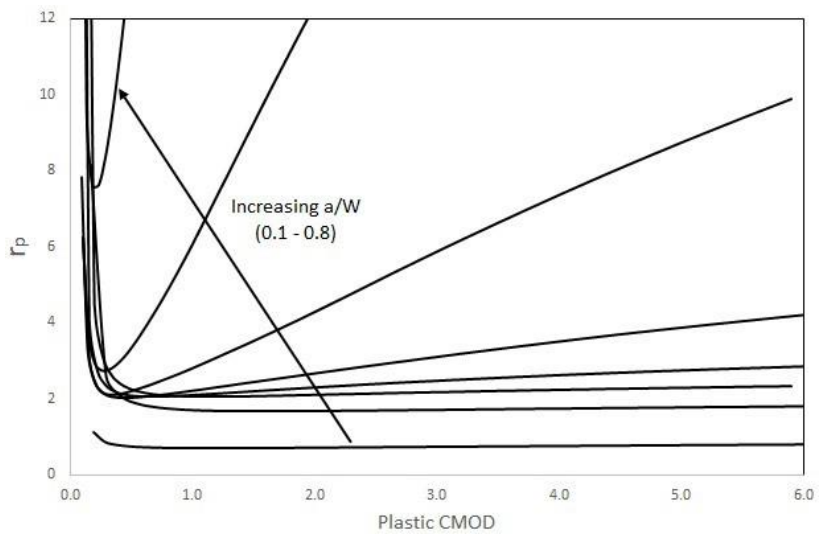
Figure 5.15.:  $r_p$  as a function of  $a/W$  ratios, Plastic CMOD, and material hardening levels (a) high hardening ( $n = 5$ ) (b) moderate hardening ( $n = 10$ ) (c) low hardening ( $n = 20$ )



(a)



(b)



(c)

Figure 5.15 shows that initially at very small plastic CMODs the  $r_p$  values go to infinity which makes sense since in SE(T) specimens during initial loading steps crack ligament undergoes only tension, which resembles a circle with infinite radius (therefore infinite  $r_p$ ), and then at larger load steps some rotation occurs, which resembles a circle with finite radius.

Figure 5.15 (c), results for low hardening material ( $n=20$ ), indicates an almost linear variation of  $r_p$  as a function of CMOD (which is an indicator of load). For shallow cracks ( $a/w \leq 0.3$ )  $r_p$  is rather independent of CMOD than being a linear function of it. This means that we can define constant  $r_p$  values for shallow cracks based on  $a/w$  ratios. Although for very

deep cracks (cases with  $a/w=0.6, 0.7$  and  $0.8$ )  $r_p$  strongly depends on CMOD, they are not the case of interest for pipeline crack growth evaluation.

For figure 5.15 (b), results for moderate hardening material ( $n=10$ ), we may have the same explanation as Figure 5.15 (c), while the limit of  $r_p$  independency from CMOD extends to  $a/w = 0.5$  rather than  $0.3$ . And then for Figure 5.15 (a), the limit of  $r_p$  independency from CMOD even extends more to  $a/w = 0.7$ .

We see that in some deeply cracked SE(T) specimen unlike SE(B) specimen it is not possible to define a constant  $r_p$  value. However, depending on material hardening levels and crack depth ( $a/w$  ratio), mostly shallow cracks, we are able to define constant  $r_p$  values. Note that when we say constant  $r_p$  it does not mean that  $r_p$  is independent of material properties and/or crack depth ( $a/w$ ), we rather mean that we can define a constant  $r_p$  for a specific material with a specific  $a/w$  ratio. In other words, for regions with plastic CMOD larger than  $\sim 0.5$  mm if  $r_p$  curve is a horizontal line,  $r_p$  is dependent only on material hardening and crack depth, while in other cases it also depends on plastic CMOD. Since we are mostly interested in shallow cracks which are the proper case for crack growth evaluation during reeling process, regardless of the value of CMOD we may derive the R-curve.

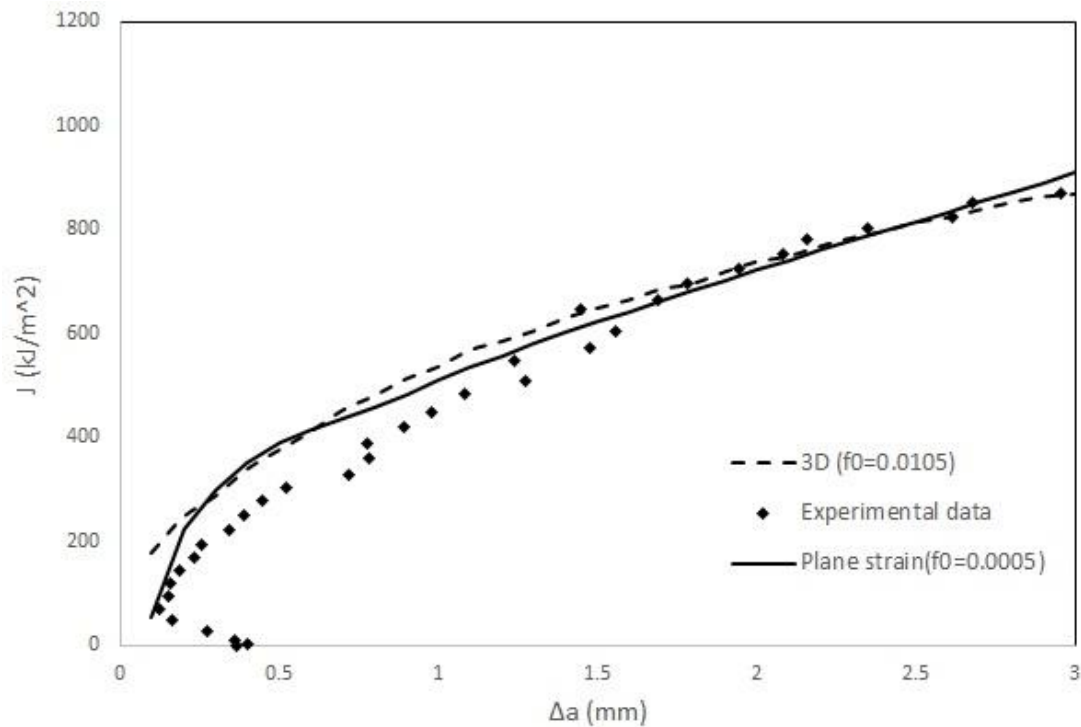
In addition to above arguments, we see that  $r_p$  values for SE(T) specimen are much higher than SE(B) specimen. This completely makes sense since in SE(T) specimen the loading is dominantly tension and therefore there is less bending and larger  $r_p$  values. To investigate the effect crack depth ( $a/W$  ratio) we can figure out that shallow cracks have smaller  $r_p$  values compared to deep cracks. In deep cracks only a small crack ligament remains which undergoes uniform stress distribution and therefore less rotation (large  $r_p$  values).

#### **5-5-1 A285 steel R-curve using $r_p$ method**

The general evaluation of  $r_p$  values showed its potential of being used as a method to estimate R-curves in SE(T) specimen. In this regard, A285 steel as a pressure vessel steel is used to evaluate and demonstrate the  $r_p$  method functionality in CTOD based R-curve estimation. Note that since we want to demonstrate the applicability of the method, a homogeneous material is considered. In this regard, plane strain and 3D models very similar to models in figure ... are generated. The fracture specimen has  $a/W = 0.4$  and  $H/W = 10$  with thickness  $B = 15$  mm, width  $W = 15$  mm. Here,  $H$  represents the distance between fixed clamps (also often designated as “day-light” between grips),  $W$  is the specimen width,  $B$  denotes de

specimen thickness and  $a$  defines the crack size. Moreover, the specimen is equipped with a 15% side-groove (7.5% on each side) to promote a more uniform crack front extension. The mechanical properties are  $E = 204 \text{ GPa}$ ,  $\nu = 0.3$ ,  $\sigma_y = 230.0 \text{ MPa}$  and  $n = 5.3$ . Figure 5.16 shows R-curve derived from plane strain and 3D calibrated models. According to material properties,  $q_1 = 1.9$ ,  $q_2 = 0.79$  and  $q_3 = q_1^2$ .

Figure 5.16.: Predicted  $J-\Delta a$  curves for the A285 steel



Now, Figure 5.17 provides the  $r_p$  values for A285 steel. The results are consistent with previously derived  $r_p$  for material with hardening  $n=5$ . Note that  $r_p$  values for CMOD less than  $\sim 0.5\text{mm}$  are ignored. The calibrated model was used to derive CTOD based R-curves, including  $r_p$  method, for A285 steel. The result for plane strain and 3D model are shown in figure 5.18 (a) and (b) respectively. The other CTOD based R-curve are also provided in order to be able to evaluate the R-curve derived by  $r_p$  method. The stress intensity factor solution for clamped SE(T) specimen are derived using equations provided in Cravero and Ruggieri's work [139].

The CTOD based R-curves for plane strain models using different methods are very close. We also see that  $r_p$  method provides more conservative results compared to Extending crack method and DCG method. In 3D model the results are more scattered. But again, the  $r_p$  method

provides more conservative results. Earlier we saw that DCG method provides very nice results for the V-groove weld and almost a conservative result for the square-groove weld. We can conclude that although it is easier to carry out  $r_p$  method to measure the R-curve, it provides very conservative result which is not favorable. DCG method holds a good level of conservatism which enables us to ensure reliable estimation but not too much which may cause considerable costs due to over estimation of crack growth.

Figure 517. :  $r_p$  variation for A285 steel

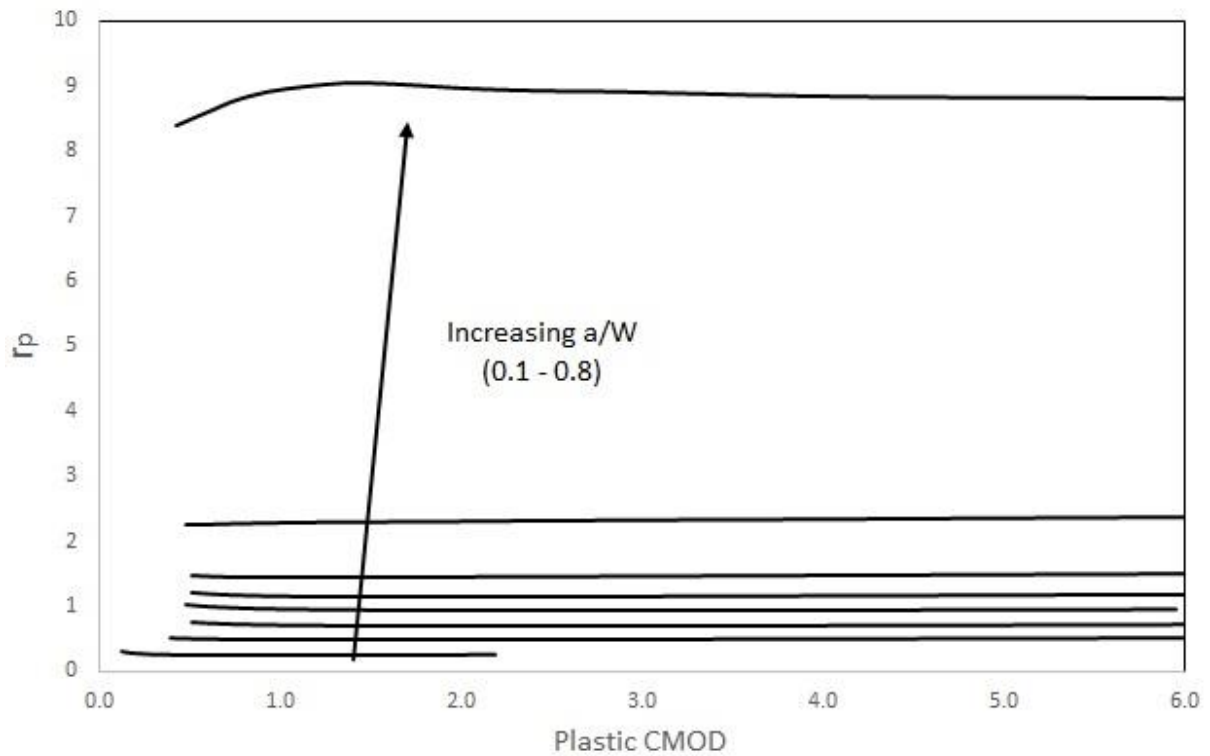
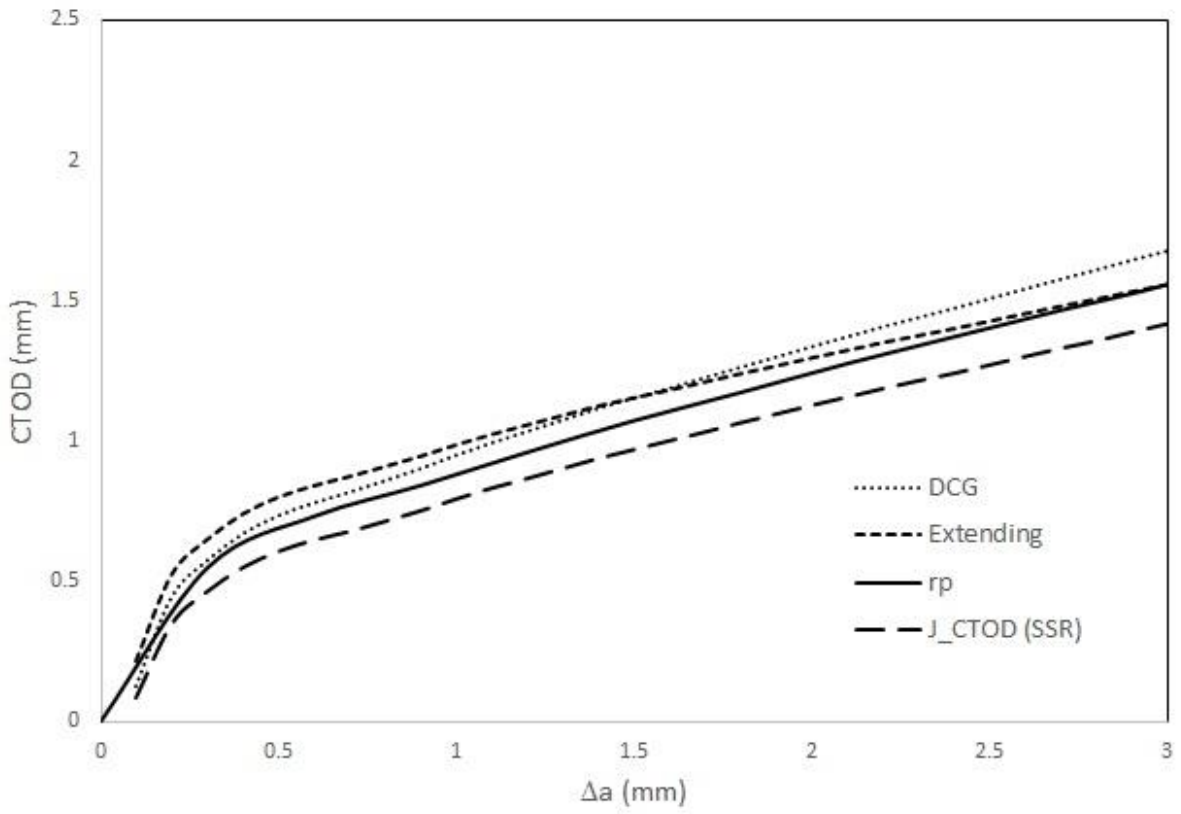
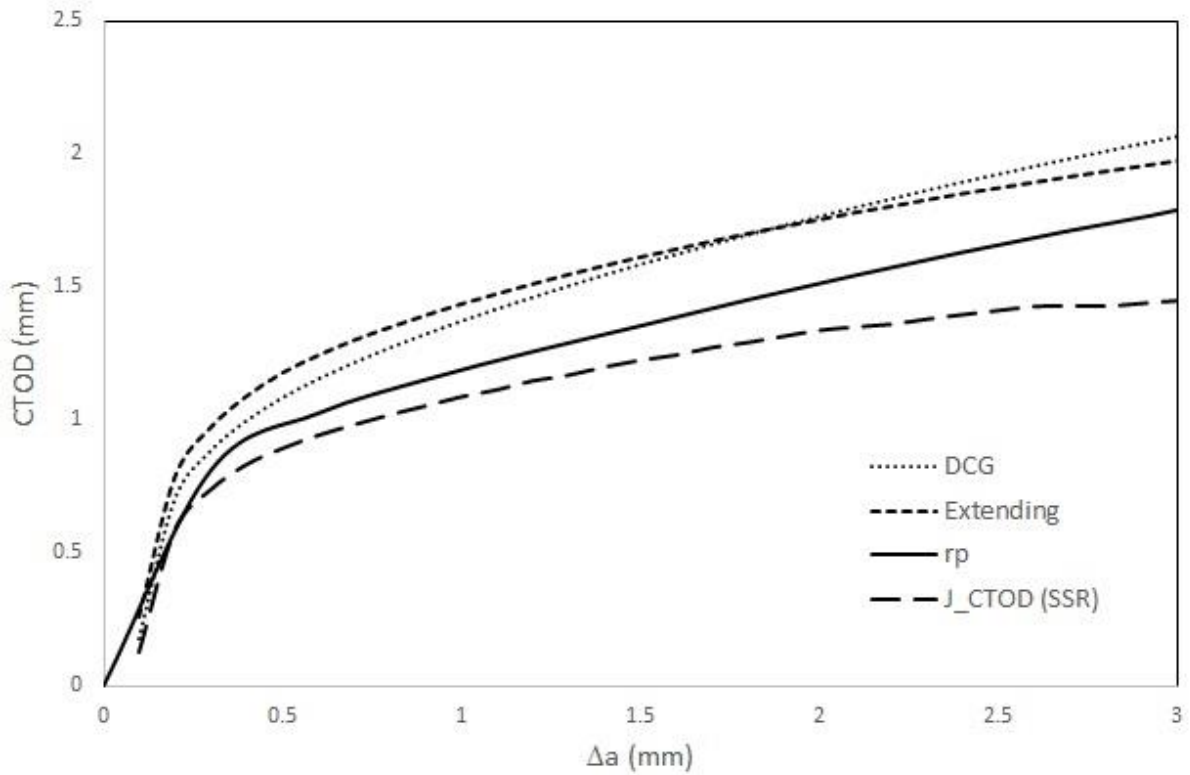


Figure 518.: CTOD based R-curves for A285 steel (a) plane strain and (b) 3D model



(a)



(b)





## CHAPTER 6

### SUMMARY AND CONCLUSION

## 6-1 Summary and Conclusion

This study describes a numerical investigation of stable ductile crack extension in pipe girth welds with different material properties to characterize the crack growth resistance behavior in terms of the  $J$ -integral and crack tip opening displacement (CTOD). The procedure laid out for describing the evolution of  $J$  and CTOD with increased loading for an extending crack involves applying a computational cell methodology to model Mode I crack extension in plane strain and 3-D models for clamped SE(T) specimens with a weld centerline crack. The investigation also covers fracture resistance tests of pipe girth welds with different levels of weld strength mismatch, including a dissimilar welded specimen extracted from a clad line pipe, from which key microstructural parameters utilized in the growth analysis are calibrated. The extensive numerical analyses are employed to determine CTOD fracture resistance curves on the basis of the following approaches: (1) CTOD-values converted from corresponding  $J$ -values of the fracture resistance data; (2) CTOD-values evaluated using the  $90^\circ$  intercept procedure based on the extending crack tip and the deformed crack flanks; (3) CTOD-values based on the double clip gage (DCG) procedure and 4) Plastic rotational factor. Predictions from the numerical analyses are also compared with experimentally measured CTOD resistance data based on the DCG method.

The present investigation shows that the evaluation procedure of  $J$ -resistance curves based on plastic work is not significantly affected by the degrees of weld strength mismatch considered in the study. Our analyses reveal that factors  $\eta_{J-CMOD}$  derived from plane-strain models of clamped SE(T) geometries with V-groove welds compare well with corresponding  $\eta$ -values applicable to homogeneous materials, particularly in the range  $a/W \leq 0.2-0.45$ . By contrast, factors  $\eta_{J-LLD}$  show a more noticeable dependence on weld strength mismatch. Overall, however, since  $\eta_{J-LLD}$  only enters into the evaluation procedure to correct  $J$  for crack growth, this effect may be expected to be relatively small. Similarly, the  $J$ -CTOD relationships are only weakly sensitive to the degree of weld strength mismatch.

The extensive set of growth analyses performed on clamped SE(T) specimens with weld centerline cracks and varying levels of weld strength mismatch reveals important differences between CTOD values based on the double clip gage (DCG) method and the  $\delta$ -values derived from  $J$ -CTOD relationships. Indeed, in every case considered in this study, including detailed 3-D analysis of a fracture specimen extracted from a dissimilar Ni-Cr girth weld, the CTOD resistance curve based on the DCG approach was always consistently higher than the

corresponding CTOD resistance data directly obtained from a  $J$ -resistance curve. Such differences are of particular concern in defect assessment procedures and ECA methodologies since the DCG method clearly provides nonconservative estimates of fracture toughness. A possible alternative to circumvent this issue would be to determine the crack driving force in the cracked component also using the DCG method so that the measured fracture toughness value and the crack tip loading parameter would be both consistent. However, this approach would also involve more computational effort and, thus, would not always be easily obtained for engineering applications and routine FFS analyses.

Our study was not limited to crack growth in SE(T) specimens and their potential level of conservativeness. Although it is well believed that SE(T) specimens hold the same level of crack tip constraint as circumferentially cracked pipes, our study indicates that yet there might be some difference between R-curves in SE(T) fracture specimen and that of actual pipes. Using V-groove girth welds provided almost the same R-curves for both SE(T) specimen and actual pipe, however, the square groove girth weld models show a much higher R-curves in actual pipe compared to SE(T) specimen, specifically for DCG method. This is caused by thicker weld material in the crack ligament due to converting V-groove weld to square one. Considering both V-groove and square weld geometry, ensures conservative estimation of crack growth resistance. However, considerable level of conservative estimation, as DCG procedure, may not be favorable.

The main interest of this study is to evaluate structural integrity of circumferentially cracked pipes under large bending during pipeline installation using reeling procedure. In this regard, Shallow cracks ( $a/w \leq 0.3$ ) are of main concern. The results show that pipes with  $a/w = 0.1$  undergo plastic deformation and failure rather than crack growth and fracture. Pipes with V-groove weld, show quite large R-curve difference for  $a/w = 0.2$  and  $a/w = 0.3$ . The reason is that in these cases, R-curves not only depend on crack depth, but also on weld metal thickness in the crack ligament, where deeper crack has less weld metal thickness in the crack ligament. However, pipes with square-groove weld show pretty close R-curves for cases with  $a/w = 0.2$  and  $a/w = 0.3$  which is completely consistent with literature and makes sense. In these cases, R-curves no longer depend on girth weld thickness since for both  $a/w = 0.2$  and  $a/w = 0.3$  we have the same girth weld thickness in the crack ligament. Considering the discussion in this paragraph, we can infer that using either V-groove or square-groove weld clamped SE(T) specimen with  $a/w = 0.3$  provides reliable

estimation of crack growth. Note that, although there is a huge difference for square-groove weld, the estimation is on safe and conservative side.

We found that using DCG method, clamped SE(T) specimens can predict crack growth in actual circumferentially cracked pipes (even though their prediction might be conservative in some cases). However, measuring R-curves using DCG method has some complexities associated with mounting two clip gauge to measure COD at two different points. Therefore, using one COD to measure R-curve might be favorable, specially for industry since it is simpler. In this regard, plastic rotational factor were investigated to measure R-curve using one COD. The results show that plastic rotational factor provides R-curves less conservative than DCG method, which is favorable. Moreover, our simulation shows that for shallow cracks, there is no need to measure the plastic portion of CMOD to derive R-curve. In fact, the absolute value of CMOD would be enough since according to Figure 5.15,  $r_P$  does depend on crack depth rather than plastic CMOD.

## 6-2 Future works

This study provided a deep insight in correlation between crack growth resistance curves in SE(T) fracture specimen and circumferentially cracked pipe. Investigation of multiple R-curves derived by various methods showed that some may provide conservative results. However, some assumption as following may alter the conservativeness level, which can be a good subject for future works.

- 1- In some pipes, the clad layer is not (very well) bounded to pipe base metal. Investigating the effect of this issue may provide new insight in R-curves and their level of conservativeness.
- 2- Investigating specimens in which clad layer has different material than weld metal (in our case clad layer and weld metal were the same). Note that when weld metal and clad layer have different material properties, the equivalent metal in homogenization procedure would change.
- 3- Using homogeneous material we demonstrated that  $r_P$  method has a great potential to measure R-curves. Investigating  $r_P$  abilities for non-homogeneous SE(T) and pipelines can be an unique idea to work on it.

## REFERENCES

- [1] AMERICAN SOCIETY FOR TESTING AND MATERIALS. **ASTM B443-00**: Standard specification for nickel-chromiummolybdenum-Columbium alloy (UNS N06625) and Nickel-Chromium- Molybdenum-Silicon alloy (UNS N06219) plate, sheet, and strip 2009.
- [2] AMERICAN SOCIETY FOR TESTING AND MATERIAL. **ASTM B444-06** : Standard specification for nickel-chromiummolybdenum-Columbium alloys (UNS N06625 and UNS N06852) and nickel-chromiummolybdenum-silicon alloy (UNS N06219) pipe and tube 2011.
- [3] WASTBERG, S. ; PISARSKI, H. ; NYHUS, B. Guidelines for engineering critical assessments for pipeline installation methods introducing cyclic plastic strain. In: INTERNATIONAL CONFERENCE ON OFFSHORE MECHANICS AND ARTIC ENGINEERING, 23., Vancouver, Canada, 2004. **OMAE 2004**: proceedings. New York : American Society of mechanical engineers, 2004.
- [4] CHIS, T. The mechanics of pipeline reeling. In: **Annals of the Oradea University: fascicle Management and Technological Engineering**, v. 6, e 16, p. 617–625, 2007.
- [5] MANOUCHEHRI, S. ; HOWARD , B. ; DENNIEL, S. A discussion of the effect of the reeled installation process on pipeline limit states. In: INTERNATIONAL OFFSHORE AND POLAR ENGINEERING CONFERENCE, 18., Vancouver, Canada, 2008. **ISOPE 2008**: proceedings. Cupertino, Calif. : International Society of Offshore and Polar Engineers, 2008.
- [6] MANOUCHEHRI, S. A discussion of practical aspects of reeled flowline installation. In: INTERNATIONAL CONFERENCE ON OCEAN, OFFSHORE AND ARTIC ENGINEERING, 31., Rio de Janeiro, Brasil, 2012. **OMAE 2012**: proceedings. New York : ASME, 2012.
- [7] RICE, J. R. A path independent integral and the approximate analysis of strain concentration by notches and cracks. **Journal Applied Mechanics**, v. 35, n. 2, p. 379–86, 1968.
- [8] HUTCHINSON, J. W. Fundamentals of the phenomenological theory of nonlinear fracture mechanics. **Journal Applied Mechanics**, v. 50, p. 1042–51, 1983.
- [9] JOYCE J. A.; HACKETT, E.M.; ROE, C. Effects of crack depth and mode loading on the J-R curve behavior of a high strength steel. In: Underwood, J. H.; Schwalbe , K.H. Dodds, R.H., eds. **Constraint effects in fracture**.

Philadelphia: American Society for Testing and Materials, 1993. p. 239–63.  
(ASTM STP, 1171)

[10] MATHIAS, LLS; SARZOSA BURGOS, D. F. ; RUGGIERI, Claudio. Effects of specimen geometry and loading mode on crack growth resistance curves of a high-strength pipeline girth weld. **International Journal Press Vessels Pip**, v.111–112, p. 106–19, 2013.

[11]ANDERSON, T. L. **Fracture mechanics**: Fundaments and Applications . 3.ed. Boca Raton, FL: CRC Press, 2005.

[12] DET NORSKE VERITAS. OFFSHORE STANDARD. **DNV-OS-F101**: submarine pipeline systems. [s.L.] 2013.

[13] DET NORSKE VERITAS. **DNV-RP-F108** :fracture control for pipeline installation methods introducing cyclic plastic strain 2006.

[14] HUTCHINSON, J. W. Fundamentals of the phenomenological theory of nonlinear fracture mechanics. **Journal of Applied Mechanics**, v. 50, p. 1042–1051, 1983.

[15] NYHUS, B.; POLANCO, M. ; ORJASAETER, O. SENT specimens as an alternative to SENB specimens for fracture mechanics testing of pipelines. In: INTERNATIONAL CONFERENCE ON OCEAN, OFFSHORE AND ARTIC ENGINEERING, 22., Cancun, Mexico, 2003. **OMAE 2003**. New York : Asme, 2003.

[16] CRAVERO, S. ; RUGGIERI, C. Correlation of fracture behavior in high pressure pipelines with axial flaws using constraint designed test specimens: Part I: Plane-strain analyses. **Engineering Fracture Mechanics**, v. 72, p. 1344–1360, 2005.

[17] SILVA, L. A. L. ; CRAVERO, S.; RUGGIERI, C. Correlation of fracture behavior in high pressure pipelines with axial flaws using constraint designed test specimens - Part II: 3-D effects on constraint. **Engineering Fracture Mechanics**, v. 76, p. 2123–2138, 2006.

[18]SHEN, G. et. al. Fracture toughness evaluation of high strength steel pipe. In: ASMEPRESSURE VESSEL AND PIPING DICISION CONFERENCE, Chicago, Illinois, 2008. **PVP 2008** : proceedings. New York : American Society of Mechanical Engineers, 2008. v. 6, p. 1275-1282.

[19] CRAVERO, S.; RUGGIERI, C. Estimation procedure of J-resistance curves for SE(T) fracture specimens using unloading compliance. **Engineering Fracture Mechanics**, v. 74, p. 2735–57, 2007.

[20] CLARKE, G. A. et. al . Single specimen tests for JIc determination. In: Rice JR, Paris PC, eds. **Mechanics of crack growth**. Philadelphia: American Society for Testing and Materials, 1976. p. 27–42. (ASTM STP, 590)

[21] LANDES, J. D. ; BEGLEY, J. A. Recent developments in JIc testing. In: Brown, W. F, Kaufman J. G, eds. Developments in fracture mechanics test methods standardization. Philadelphia: American Society for Testing and Materials, 1977. p. 57–82. ( ASTM STP, 632)

[22] RUGGIERI, C. Further results in J and CTOD estimation procedures for SE(T) fracture specimens – Part I: homogeneous materials. **Engineering Fracture Mechanics**, v. 79, p. 245–65, 2012.

[23] PAREDES, M. ; RUGGIERI, C. Further results in J and CTOD estimation procedures for SE(T) fracture specimens – Part II: weld centerline cracks. **Engineering Fracture Mechanics**, v. 89, p. 24–39, 2012.

[24] ZHU, X. K.; MCGAUGHY, T. A review of fracture toughness testing and evaluation using sent specimens. In: INTERNATIONAL PIPELINE CONFERENCE (IPC), 10., Calgary, Alberta, Canada, 2014. **New York, NY : ASME, 2014.**

[25] RUGGIERI, C. Low constraint fracture toughness testing using se(t) and se(b) specimens. **International Journal Press Vessels Pip**, v. 156, p. 23–39, 2017.

[26] ZHU, X. K. Review of fracture toughness test methods for ductile materials in low-constraint conditions. **International Journal Pressure Vessel Pip**, v. 139–140, p. 173–83, 2016.

[27] BURDEKIN, F. M. Stone DEW. The crack opening displacement approach to fracture mechanics in yielding materials. **Journal of Strain Analysis**, v.1, n.2, p. 145–53, 1966.

[28] HARRISON, J.D. et. al. The COD approach and its application to welded structures. In: Landes, J.D, Begley J.A., Clarke G.A, eds. **Elastic-plastic fracture**. Philadelphia: American Society for Testing and Materials, 1979. p. 606–31. (ASTM STP, 668)

[29] MOORE, P. L; PISARSKI, HG. Validation of methods to determine CTOD from SENT specimens. In: INTERNATIONAL OFFSHORE AND POLAR ENGINEERING CONFERENCE, 22., Vancouver, 2012. **ISOPE**. Cupertino, CA : ISOPE, 2012.

[30] EXXONMOBIL upstream, measurements of crack-tip opening displacement (CTOD) fracture resistance curves using single-edge notched tension (SENT) specimens. ( Technical Report, 2010)



- [31] WEEKS, TS; LUCON, E. Direct comparison of single-specimen clamped SE(T) test methods on X100 line pipe steel. In: INTERNATIONAL PIPELINE CONFERENCE, 10., Calgary, Canada, 2014. **IPC 2014** : proceedings, New York : Asme, **2014**
- [32] BRITISH STANDER INSTITUTION. **BS 8571**: method of test for determination of fracture toughness in metallic materials using single edge notched tension (SENT) specimens, 2018.
- [33] IRWIN, G.R. Analysis of stresses and strains near the end of a crack traversing a plate. **Journal of Applied Mechanics**, v.24, p.361-364, 1957.
- [34] WESTERGAARD, H.M. Bearing pressure and cracks. **Journal of Applied Mechanics**, v. 6, p.49-53, 1939.
- [35] WILLIAM, M.L. On the stress distribution at the base of a stationary crack. **Journal of Applied Mechanics**, v. 24, p.109-114, 1957.
- [36] RICE, J.R. Limitations to the small scale yielding approximation for crack tip plasticity. **Journal of the Mechanics and Physics of Solids**, v. 22, n. 1, p.17-26, 1974.
- [37] ABU-MUHARIB, Andrew et. al. Cleavage fracture modelling for RPV steels: discrete model for collective behaviour of microcracks. In: PRESSURE VESSEL PIPING CONFERENCE , Paris, 2013. **ASME 2013** : proceedings: New York: American Society of Mechanical Engineers, 2013.
- [38] SHERRY, A.H. ; France, C.C ; .Goldthorpe, M.R Compendium of T-stress solutions for two and three dimensional cracked geometries. **Fatigue & Fracture of Engineering Materials & Structures**, v.18, n. 1, p.141-155, 1995.
- [39] TVERGAARD, V.; HUTCHINSON, J.W. Effect of T-stress on mode I crack growth resistance in a ductile solid. **International Journal of Solids and Structures**. v.31, n. 6, p. 823-84, 1994.
- [40] SURESH, S. **Fatigue of materials**. Cambridge: Cambridge University Press, 1991.
- [41] MURAKAMI, Y. **Stress intensity factors handbook**. Oxford: Pergamon, 1987. v.1-2
- [42] TADA, H.; PARIS, P. C.; IRWING, G. R. **The stress analysis of cracks handbook**. 3.ed. New York : American Society of Mechanical Engineers, 2000.
- [43] British Stander Institution. **BS 7910**: guide to methods for assessing the acceptability of flaws in metallic structures, 2005.

[44] British Standard Institution . **BS 7448-2**: fracture mechanics toughness tests. Method for determination of  $K_{Ic}$ , critical CTOD and critical J values of welds in metallic materials, 1997.

[45] ANDRIANOPOULOS, N. P. ; BOULOUGOURIS, V. C. On an intrinsic relationship between plane stress and plane strain critical stress intensity factors. **International Journal of Fracture**, v. 67, n.1, p.R9-R12, 1994.

[46] WELLS, A.A. Unstable crack propagation in metals: cleavage and fast fracture. In: PROCEEDINGS OF THE CRACK PROPAGATION SYMPOSIUM, Cranfield, UK, 1961. **Proceedings. Cranfield : College of Aeronautics, 1961.** v. 1, Paper 84

[47] HUTCHINSON, J.W. Singular behaviour at the end of a tensile crack in a hardening material. **Journal of the Mechanics and Physics of Solids**, v.16, n. 1 p.13-31, 1968.

[48] RICE, J.R.; ROSENGREN, G.F. Plane strain deformation near a crack tip in a power-law hardening material. **Journal of the Mechanics and Physics of Solids**, v.16, n. 1, p.1-12, 1968.

[49] JANSSEN, M.; ZUIDEMA, J. ; WANHILL, R.J.H. **Fracture mechanics**, 2. ed. New York: Spon Press, 2004.

[50] WEBSTER, G.A. ; AINSWORTH, R.A. **Ainsworth, high temperature component life assessment.** London: Chapman & Hall, 1994.

[51] AMERICAN SOCIETY TECHNICAL MECHANICS. **ASTM E813-81**: standard test method for JIC, a measure of fracture toughness, annual book of ASTM standards. Philadelphia: ASTM, 1981. part.10, p.822-840.

[52] SHIH, C.F. Relationship between the J-integral and the crack opening displacement for stationary and extending cracks. **Journal of the Mechanics and Physics of Solids**, v. 29, p.305-26, 1981.

[53] HANCOCK, J.W. ; REUTER, W.G.; PARKS, D. Constraint and toughness parameterized by T, constraint effects in fracture. Philadelphia : American Society for Testing and Materials, 1993. p. 21–40 (ASTM STP, 1171)

[54] JOYCE J.A.; LINK, R.E. Effects of constraint on upper shelf fracture toughness. **Fracture mechanics.** Philadelphia : American Society for Testing and Materials, 1995. v.26, p.142-77 (ASTM STP, 1256)

[55] ZHU, X.K. ; JANG, S. K. J–R curves corrected by load-independent constraint parameter in ductile crack growth. **Engineering Fracture Mechanics**, v. 68, n.3, p. 285-301, 2001.

[56] BETEGON, C. ; HANCOCK, J.W. Two-parameter characterization of elasticplastic crack-tip fields. **Journal of Applied Mechanics**, v.58, n.1, p.104-110, 1991.

[57] O'DOWD, N.P. ; SHIH, C.F. Family of crack-tip fields characterized by a triaxiality parameter-I: structure of fields. **Journal of the Mechanics and Physics of Solids**, v. 39, n.8, p. 989-1015, 1991.

[58] O'DOWD, N.P. SHIH, C.F. Family of crack-tip fields characterized by a triaxiality parameter-II. Fracture applications. **Journal of the Mechanics and Physics of Solids**, v.40, n.5, p. 939-963, 1992.

[59] CHAO, Y.J.; YANG, S. ; SUTTON, M.A. On the fracture of solids characterized by one or two parameters: theory and practice. **Journal of the Mechanics and Physics of Solids**, v.42, n. 4, p. 629-647, 1994.

[60] PARDOEN, T. ; MARCHAL, Y.; DELANNAY, F. Thickness dependence of cracking resistance in thin aluminium plates. **Journal of the Mechanics and Physics of Solids**, v.47,n.10, p.2093- 2123, 1999.

[61]ERNST, H. A. ; PARIS, P. C. ; LANDES, J. D. Estimations on J-integral and tearing modulus T from a single specimen record. In: Roberts, R, ed. Proceedings of the Internatinal Symposium on Fracture Mechanics, 13., **Fracture mechanics. Philadelphia, Pa : American Society for Testing and Materials, 1981.** p. 476-502. (ASTM STP, 743)

[62] CRAVERO, S.; RUGGIERI, C. Further developments in J evaluation procedure for growing cracks based on LLD and CMOD data. **International Journal Fracture**, v.148, p. 387-400, 2007.

[63] ZHU, X.K.; LEIS, B. N. ; JOYCE, J. A. Experimental estimation of J-R curves from load- CMOD record for SE(B) specimens. **Journal of ASTM International**, v.5, n. 5, p. 1-15, 2008.

[64]KANNINEN, M. ; POPELAR, C. H. **Advanced fracture mechanics.** New York: Oxford University Press; 1985.

[65] KIRK, M. T.; DODDS, R. H. J and CTOD estimation equations for shallow cracks in single edge notch bend specimens. **Journal of Testing and Evaluation**, v.21, p. 228e38, 1993.

[66] KIM, Y. J.; SCHWALBE, K. H. On experimental J estimation equations based on CMOD for SE(B) specimens. **Journal of Testing and Evaluation** v.29, p. 67e71, 2001.

[67] DONATO, G. H. B. ; RUGGIERI, C. Estimation procedure for J and CTOD fracture parameters using three-point bend specimens. In: INTERNATIONAL

PIPELINE CONFERENCE 6., Calgary, Canada, 2006. **IPC 2006. New York, NY ASME, 2006** . p. 149-157.

[68] RUGGIERI, C. **FRACTUS2D**: numerical computation of fracture mechanics parameters for 2-D cracked solids. [São Paulo]: Universidade de Sao Paulo, 2011. (Tech rep. )

[69] SHIH, C.F.; MORAN, B.; NAKAMURA, T. Energy release rate along a threedimensional crack front in a thermally stressed body. **International Journal of Fracture**, v.30, n.2, p.79-102, 1986.

[70] AMERICAN SOCIETY FOR TESTING AND MATERIALS. **ASTM E1820-15**: Standard test method for measurement of fracture toughness. 2015.

[71] SARZOSA BURGOS, Diego Felipe ; SOUZA, R.F. ; RUGGIERI, C. J-CTOD and growth analysis. **Engineering Fracture Mechanics**, v. 147, p. 331-54, 2015.

[72] DOWLING, A.R.; ROWNLEY, C.H.A. The effect of defects on structural failure. A two criteria approach. **International Journal of Pressure Vessels and Piping**, v.3, n.2, p.77-107,1975.

[73] BUDDEN, P.J.; SHARPLES, J.K. ; DOWLING, A.R. Dowling. The R6 procedure: recent developments and comparison with alternative approaches. **International Journal of Pressure Vessels and Piping**, v.77, n.14-15, p.895-903, 2000.

[74] R6: assessment of the integrity of structures containing defects, revision 4, [s.L.] : British Energy Generation, 2005.

[75] CRAVERO, S.; RUGGIERI, C. Structural integrity analysis of axially cracked pipelines using conventional and constraint-modified failure assessment diagrams. **International Journal of Pressure Vessels and Piping**, v.83, n.8, p.607-617, 2006.

[76] LIDBURY, D.P.G. et al. Prediction of the first spinning cylinder test using continuum damage mechanics. **Nuclear Engineering and Design**, v.152, n.1-3, p.1-10, 1994.

[77] BILBY, B.A. et. al. Some experience in the use of damage mechanics to simulate crack behaviour in specimens and structures. **International Journal of Pressure Vessels and Piping**, v.64, n.3, p.213-223, 1995.

[78] BETHMONT, M et. al. The method of local approach of fracture and its application to a thermal shock experiment. **Nuclear Engineering and Design**, v.119, n. 2-3, p.249-261, 1990.

- [79] HOWARD, I.C.; SHEIKH, M.A. **Simulation of nuclear safety tests**. Sheffield : Department of Mechanical and Process Engineering, The University of Sheffield, UK, 1994. (Final Report)
- [80] ERIPRET, C. et. al. Prediction of fracture in the transition regime: Application to an A533B pressure vessel steel. **Advances in Fracture Research**. Oxford : Pergamon, 1997. p.197-205
- [81] PINEAU, A. Development of the local approach to fracture over the past 25 years: Theory and applications. **International Journal of Fracture**, v.138, n.1/4, p.139-166.
- [82] MCCLINTOCK, F. A. A criterion for ductile fracture by the growth of holes. **Journal Applied Mechanics**, v. 35, n. 3, p.363-371, 1968.
- [83] RICE, J. R. ; TRACEY, D. M. On the ductile enlargement of voids in triaxial stress fields. **Journal of Mechanics Physics of Solids**, v. 17, n. 3, p. 201-20, 1969.
- [84] GURSON, A. L. Continuum theory of ductile rupture by void nucleation and growth: Part I—Yield criteria and flow rules for porous ductile media. **Journal of Engineering Materials & Technology**, v. 99, n. 2-15, 1977.
- [85] GURSON, A. L. **Plastic flow and fracture behavior of ductile materials incorporating void nucleation, growth, and interaction**. (Thesis) - Brown University, 1977.
- [86] ROUSSELIER, G. Ductile fracture models and their potential in local approach of fracture. **Nuclear Engineering and Design**, v. 105, n. 1, p. 97-111, 1987.
- [87] ROUSSELIER, G. et al. A methodology for ductile fracture analysis based on damage mechanics: an Illustration of a local approach of fracture. **Nonlinear Fracture Mechanics** : elastic-plastic Fracture. West Conshohocken, Pa. : ASTM International, 1988. v.2, p. 332-354 (ASTM STP, 995)
- [88] TVERGAARD, V. Material failure by void growth to coalescence. **Advances in Applied Mechanics**, v.27, p. 83-151, 1989.
- [89] FALESKOG, J.; GAO, X.; SHIHH, C.F. Cell model for nonlinear fracture analysis – I. Micromechanics calibration. **International Journal of Fracture**, v. 89, p. 355-373, 1988.
- [90] GAO, X., FALESKOG , J.; SHIHH, C.F. Cell model for nonlinear fracture analysis – II: fracture-process calibration and verification. **International Journal of Fracture**, v.89, p. 375-398, 1988.

- [91] ZHANG, Z. **A Practical micro-mechanical model-based local approach methodology for the analysis of ductile fracture of welded t-joints**. Tese (Doutorado) - Lappeenranta University of Technology, 1994..
- [92] TVERGAARDT, V. ; NEEDLEMAN, A. Analysis of the cup-cone fracture in a round tensile bar. **Acta Metallurgica**, 32, n.1, p. 157-169, 1984.
- [93] ZHANG , Z. ; HAUGE, M. On the Gurson micro-mechanical parameters. **Fatigue & Fracture Mechanics**. West Conshohocken, PA : American Society for Testing and Materials, 1999. V. 29
- [94] THOMASON, P. F. **Ductile fracture of metals**. Pergamon Press: 1990.
- [95] RUGGIERI, C.; PANONTIN, T. L. ; DODDS, R. Numerical modeling of ductile crack growth in 3-D using computational cell elements. **International Journal of Fracture**, v. 82, n.1, p. 67- 95, 1966.
- [96] PENUELAS, I.; BETEGON, C. ; RODRIGUEZ, C. A ductile failure model applied to the determination of the fracture toughness of welded joints. Numerical simulation and experimental validation. **Engineering Fracture Mechanics**, v.73, n.18, p. 2756-2773, 2006.
- [97] NEEDLEMANN, A. ; RICE, J. Limits to ductility set by plastic flow localization. **Mechanics of Sheet Metal Forming**. Boston: Springer, 1979. p. 237-267
- [98] CHU, C. ; NEEDLEMAN , A. (1980). Void nucleation effects in biaxially stretched sheets. **Journal of Engineering Materials & Technology** v. 102, n. 3, p. 249-256, 1980.
- [99] SOVIK, O. Experimental and numerical investigation of void nucleation in an AlMgSi alloy. **Journal de Physique IV**::colloque, v.6, c. 6, p.155-164, out. 1996.
- [100] LE ROY , G., et al. A model of ductile fracture based on the nucleation and growth of voids. **Acta Metallurgica**, v. 29, p. 1509-1522, 1981.
- [101] GURLAND, J. Observations on the fracture of cementite particles in a spheroidized 1.05C steel deformed at room temperature. **Acta Metallurgica**. v.20, p. 735-741, 1972.
- [102] Gullerud, A. S., Gao, X., Dodds, R. H. and Haj-Ali, R. Simulation of ductile crack growth using computational cells: numerical aspects. **Engineering Fracture Mechanics**, v. 66, no. 1, p. 65-92, 2000.
- [103] ZHANG, Z.; THAULOW, C. ; ØDEGARD, degård, J. (2000). A complete Gurson model approach for ductile fracture. **Engineering Fracture Mechanics**, v. 67, n. 2, p. 155-168.

- [104] PARDOEN, T. ; HUTCHINSON, J. W. An extended model for void growth and coalescence. **Journal of the Mechanics & Physics of Solids**, v. 48, n.12, p. 2467-2512, 2000.
- [105] HEALY, B. et. al.. WARP3D: 3-D Dynamic Nonlinear Fracture analyses of solids using parallel computers, user manual. Illinois: University of Illinois at Urbana-Champaign, 2020. Disponível em: <http://www.warp3d.net/>. Acesso em: 18 jul. 2022
- [106] RUGGIERI, C. ; HIPPERT, E. Cell model predictions of ductile fracture in damaged pipelines. In: Reuter, W.G ;. Piascik, R. S., org. **Fatigue & Fracture Mechanics**, West Conshohocken, PA: ASTM International, 2002. v. 33, p. 176-191. (ASTM STP, 1417)
- [107] CHEN, Y. ; LAMBERT, S. Numerical modeling of ductile tearing for semielliptical surface cracks in wide plates. **International Journal of Pressure Vessels & Piping**, v. 82, n. 5, p. 417-426, 2005.
- [108] RUGGIERI, C. ; DOTTA, F. Numerical modeling of ductile crack extension in high pressure pipelines with longitudinal flaws. **Engineering Structures**, v. 33, n.5, p. 1423-1438, 2011.
- [109] BOLINDER, T. (2014). Numerical simulation of ductile crack growth in residual stress fields. **Stockholm : Strålsäkerhetsmyndigheten, 2014.**
- [110] TAKTAK, R.; BENSEDDIQ, N. ; IMAD, A. Analysis of ductile tearing using a local approach to fracture. **Fatigue & Fracture of Engineering Materials & Structures**, v. 32, n. 6, p. 525-530, 2009.
- [111] XIA, L. ; SHIH, C. F. Ductile crack growth—I: a numerical study using computational cells with microstructurally-based length scales. **Journal of the Mechanics & Physics of Solids**, v.43, n. 2, p. 233-259, 1995.
- [112] ] XIA, L. ; SHIH, C. F. Ductile crack growth—II. Void nucleation and geometry effects on macroscopic fracture behavior. **Journal of the Mechanics & Physics of Solids**, v.43, n.12, p. 1953-1981, 1995.
- [113] NOURPANA, N. ; TAHERI, F. Ductile crack growth and constraint in pipeline subject to combined loadings. **Engineering Fracture Mechanics**, v. 78, p. 2010–2028, 2011.
- [114] SARZOSA BURGOS, D. F. ; RUGGIERI, C. A numerical investigation of constraint effects in circumferentially cracked pipes and fracture specimens including ductile tearing. **International Journal of Pressure Vessels and Piping**, v. 120-121, p. 1-18, Aug–Sept. 2014.

- [115] CHEN, Y. LAMBEET, S. Analysis of ductile tearing of pipeline-steel in single edge notch tension specimens. **International Journal of Fracture**, v. 124, p. 179–199, 2003.
- [116] CRAVERO, S. ; BRAVO, R. E. ; ERNST, H. A. Constraint evaluation and effects of J –R resistance curves for pipes under combined load conditions, In: INTERNATIONAL OFFSHORE AND POLAR ENGINEERING CONFERENCE , 18., Vancouver, CA, 2008. **ISOPE 2008 : proceedings, Cupertino, CA : ISOPE, 2008.**
- [117] CRAVERO, S. ; BRAVO, R. E. ; ERNST, H. A. Fracture mechanics evaluation of pipes subjected to combined load conditions. In: INTERNATIONAL CONFERENCE ON OCEAN, OFFSHORE AND ARTIC ENGINEERING, 28., Honolulu, Hawaii, 2009. **Proceedings. New York, N.Y. : American Society of Mechanical Engineers, 2009.**
- [118] XU, J.et. al. Constraint effect on the ductile crack growth resistance of circumferentially cracked pipes. **Engineering Fracture Mechanics**, v. 77, n.4, p. 671–684, 2010.
- [119] GINTALAS, M. AINSWORTH, R. A. Ainsworth, Engineering fracture mechanics, a constraint correction method based on use of a single test specimen. **Engineering Fracture Mechanics**, v. 247, p. 1-22, Apr. 2021
- [120] ZHU, X. ; ZELENAK, K.P., and MCGAUGHY, T., Comparative study of CTODresistance curve test methods for SENT specimens. **Engineering Fracture Mechanics**, v. 172, p. 17-38, 2017.
- [121] SOUZA, R. F. ; RUGGIERI, C. ; ZHANG, Z. A framework for fracture assessment of dissimilar girth welds in offshore pipelines under bending, **Engineering Fracture Mechanics**, v. 163, p. 66–88, 2016.
- [122] HERTELÉ, S. et al. J-integral analysis of heterogeneous mismatched girth welds in clamped single-edge notched tension specimens. **International Journal of Pressure Vessel and Piping**, v. 119, p. 95–107, 2014.
- [123] HAO, S. ; CORNEC, A. ; SCHWALBE, K. H. Schwalbe, plastic stress-strain fields and limit loads of a plane strain cracked tensile panel with a mismatched welded joint. **International Journal of Solids and Structures**, v. 34, p. 297–326, 1997.
- [124] LEI, R. A. AINSWORTH, A J integral estimation method for cracks in welds with mismatched mechanical properties. **International Journal of Pressure Vessel and Piping**, v.70, p. 237–245, 1997.
- [125] LEI, Y. ; TAO, J. ; LI, P. N. Limit load and J estimates of a centre cracked plate with an asymmetric crack in a mismatched weld. **International Journal of Pressure Vessels and Piping**, v.76, p. 747–757, 1999.



- [126] AMERICAN PETROLEUM INSTITUTE. **Specification for line pipe**. Washington, D.C. : American Petroleum Institute, 2007.
- [127] AMERICAN SOCIETY FOR TESTING AND MATERIALS. **ASTM A106**: Standard specification for seamless carbon steel pipe for high-temperature service, 2015. [s.L.] : ASTM International, 2015.
- [128] AMERICAN PETROLEUM INSTITUTE . **API RP-579-1/ ASME FFS-1** Fitness-for-service. [s.L.] : API, 2016.
- [129] RAMBERG, W. ; OSGOOD, W. R. **Description of stress-strain curves by three-parameters**. Washington : NACA, 1943. (Technical Report , NACA-TN-902)
- [130] RUGGIERI, C. **Test procedure for fracture resistance characterization of pipeline steels and pipeline girth welds using single-edgednotched tension (SENT) specimens**. [ São Paulo] : Universidade de São Paulo, 2020. (Technical Report, 2020).
- [131] SOUZA, R.F. ; RUGGIERI, C. Revised wide range compliance solutions for selected standard and non-standard fracture test specimens based on crack mouth opening displacement. **Engineering Fracture Mechanics**, v. 178, p. 77–92, Jun. 2017.
- [132] SARZOSA BURGOS, D. F. et al. Fracture resistance testing of dissimilar nickel-chromium girth welds for clad line pipes. **International Journal Fracture** v. 205, n. 2, p. 168–88, 2017.
- [133] JOYCE, J. A. **Manual on elastic-plastic fracture**: laboratory test procedure. West Conshohocken, Pa : ASTM International, 1996. (ASTM Manual Series, MNL 27)
- [134] FERREIRA, C. ; SARZOSA BURGOS, D. F; RUGGIERI, C. Fracture toughness testing of an overmatched pipe girth weld using clamped SE(T) specimens. In: ASME PRESSURE AND PIPING CONFERENCE  
San Antonio, Texas; 2019. **ASME 2019** : proceedings. New York, N.Y. : American Society of Mechanical Engineers, [2019]
- [135] Moran B, Shih CF. A general treatment of crack tip contour integrals. **International Journal Fracture**, v.35, p. 295–310, 1987.
- [136] SARZOSA BURGOS, D. F. ; SOUZA, R. F. ; RUGGIERI, C. J-CTOD relations in clamped SE(T) fracture specimens including 3-D stationary and growth analysis. **Engineering Fracture Mechanics**, v. 147, p. 331-54, 2015.
- [137] SARZOSA BURGOS, D. F. **Personal communication**. [s.L.] : s.ed. 2020.

[138] BAYLEY, C. **Evaluation of the single edge notch tension specimen for quantifying fracture toughness.** Dartmouth, Canada : Defence Research and Development Canada ,2015. (Scientific Report, DRDC-RDDC-2015-R156)

[139] CRAVERO, S.; RUGGIERI, C. Estimation procedure of J-resistance curves for SE(T) fracture specimens using unloading compliance. **Engineering Fracture Mechanics**, v.74, p. 2735-2757, 2007.